FINAL REPORT

Development of a Portable Surface Enhanced Raman Sensor For Real-Time Detection and Monitoring of Perchlorate And Energetics

SERDP Project ER-1602

January 2012

Baohua Gu
Nahla Hatab
Gyula Eres
Oak Ridge National Laboratory

Paul Hatzinger
Shaw Environmental, Inc.

Pamela Boss
Space and Naval Warfare Systems Center

SERDP
DOD ▪ EPA ▪ DOE

REPORT DOCUMENTATION PAGE

Form Approved
OMB No. 0704-0188

PLEASE DO NOT RETURN YOUR FORM TO THE ABOVE ORGANIZATION.

1. REPORT DATE *(DD-MM-YYYY)*	2. REPORT TYPE	3. DATES COVERED *(From - To)*
31-01-2012	final	March 2008 - December, 2011

4. TITLE AND SUBTITLE

Development of a Portable Fiberoptic Surface Enhanced Raman Sensor for In-Situ Detection and Monitoring of Perchlorate and Energetics

5a. CONTRACT NUMBER

DE-AC05-00OR22725

5b. GRANT NUMBER

NA

5c. PROGRAM ELEMENT NUMBER

6. AUTHOR(S)

Gu, Baohua, Ph.D.
Hatzinger, Paul B., Ph.D.
Boss, Pamela A., Ph.D.

5d. PROJECT NUMBER

ER-1602

5e. TASK NUMBER

NA

5f. WORK UNIT NUMBER

NA

7. PERFORMING ORGANIZATION NAME(S) AND ADDRESS(ES)

Environmental Sciences Division
Oak Ridge National Laboratory
Oak Ridge, TN 37831-6036

8. PERFORMING ORGANIZATION REPORT NUMBER

NA

9. SPONSORING/MONITORING AGENCY NAME(S) AND ADDRESS(ES)

Strategic Environmental Research and Development Program
901 N Stuart St., Suite 303
Arlington VA 22203

10. SPONSOR/MONITOR'S ACRONYM(S)

SERDP

11. SPONSOR/MONITOR'S REPORT NUMBER(S)

ER-1602

12. DISTRIBUTION/AVAILABILITY STATEMENT

Distribution Statement A: Approved for Public Release, Distribution is Unlimited

13. SUPPLEMENTARY NOTES

None

14. ABSTRACT

Costs for environmental analysis and monitoring are increasing at a rapid rate and represent a significant percentage of the total and future remedial expenses at many U.S. Department of Defense (DoD) contaminated sites. This project developed a cost-effective, miniaturized sensor for rapid field detection and monitoring of perchlorate (ClO4-), trinitrotoluene (TNT), and cyclotrimethylene-trinitramine (RDX) in contaminated groundwater or surface water via fiber-optic surface enhanced Raman spectroscopy (SERS) techniques. The performance of the potable Raman sensor was evaluated for detection and analysis of energetics both in laboratory and field. We showed the detection of ClO4-, TNT, and RDX at ppb to sub-ppm concentration levels in groundwater from a number of contaminated monitoring wells at several selected DoD military sites. This new technology shows the potential to provide a tool for rapid, in-situ screening and analysis of energetics that are both important for environmental monitoring and of interest for national security.

15. SUBJECT TERMS

Raman sensor, energetics, perchlorate, TNT, RDX, detection, SERS, gold nanoparticles, bowties, electron beam lithography

16. SECURITY CLASSIFICATION OF:			17. LIMITATION OF ABSTRACT	18. NUMBER OF PAGES	19a. NAME OF RESPONSIBLE PERSON
a. REPORT	b. ABSTRACT	c. THIS PAGE			19b. TELEPHONE NUMBER *(Include area code)*
U	U	U	UU		

This report was prepared under contract to the Department of Defense Strategic Environmental Research and Development Program (SERDP). The publication of this report does not indicate endorsement by the U.S. Department of Defense, nor should the contents be construed as reflecting the official policy or position of the Department of Defense. Reference herein to any specific commercial product, process, or service by trade name, trademark, manufacturer, or otherwise, does not necessarily constitute or imply its endorsement, recommendation, or favoring by the Department of Defense.

TABLE OF CONTENTS

LIST OF FIGURES

LIST OF TABLES

ACRONYMS AND ABBREVIATIONS

Au	Gold
Ag	Silver
ccd	Center-to-center distance
CD	Cyclodextrin
CCD	Charge-coupled device
Cl^-	Chloride
ClO_4^-	Perchlorate
CNMS	Center for Nanophase Materials Science
CTAB	Cetyl-trimethylammonium bromide
DI	Deionized
DMAE	2-(dimethylamino)-ethanethiol hydrochloride
DO	Dissolved oxygen
DOE	Department of Energy
DoD	Department of Defense
E	Electromagnetic field
EBL	Electron beam lithography
EF	Enhancement factor
EPA	Environmental Protection Agency
ER	Environmental restoration
ESI	Electron spray ionization
ESTCP	Environmental Security Technology Certification Program
FDTD	Finite difference time domain
GC	Gas chromatography
GC/MS	GC/mass spectrometry
GW	Groundwater
$HAuCl_4$	Gold chloride
HCl	Hydrochloric acid
HNO_3	Nitric acid
HPLC	High performance liquid chromatography
HPLC/MS	HPLC/mass spectrometry
IC	Ion chromatography
ITRC	Interstate Technology and Regulatory Council
LDRD	Laboratory Directed Research and Development
LTM	Long term monitoring
M	moles
MD	Maryland
MΩ	Megaohms
MW	Monitoring well
$NaBH_4$	Sodium borohydride
$Na_3C_6H_5O_7$	sodium citrate
ND	non-detect
NO_3^-	Nitrate
NMR	Nuclear magnetic resonance
NPGS	Nanometer Pattern Generation System

ORNL	Oak Ridge National Laboratory
p-ATP	*p*-aminothiophenol = *p*-mercaptoaniline (*p*MA)
PO_4^{3-}	Phosphate
*p*MA	*p*-mercaptoaniline = *p*-aminothiophenol (*p*-ATP)
QCM	Quartz-crystal microbalance
RIE	Reactive ion etching
RDX	Cyclotrimethylene-trinitramine
rrd	Row-to-row distance
SEM	Scanning electron microscopy
SERDP	Strategic Environmental Research and Development Program
SERS	Surface enhanced Raman spectroscopy
SGW	Synthetic groundwater
Si	Silicon
SO_4^{2-}	Sulfate
TcO_4^-	Pertechnetate
TEM	Transmission electron microscopy
TN	Tennessee
TNT	Trinitrotoluene
TOC	Total organic carbon
UK	United Kingdom
USEPA	United States Environmental Protection Agency
UV	Ultraviolet
VA	Virginia
VOCs	Volatile organic compounds

ACKNOWLEDGEMENTS

We wish to thank Chun-Hway Hsueh and Zhenyu Zhang at ORNL for performing theoretical calculations, Randy Cramer, Vanessa Lovejoy, and Macon Patterson from the US Navy for their assistance in field sampling and analysis, and Dr. Andrea Leeson of the Strategic Environmental Research and Development Program (SERDP) for her support and oversight during this project. The project was funded by the SERDP Program (Project ER-1602) to Oak Ridge National Laboratory (ORNL), which is managed by UT-Battelle LLC for U.S. Department of Energy (DOE) under contract DE-AC05-00OR22725.

EXECUTIVE SUMMARY

Costs for environmental analysis and monitoring are increasing at a rapid rate and represent a significant percentage of the total and future remedial expenses at many U.S. Department of Defense (DoD) contaminated sites. It has been reported that about 30 to 40% of the remediation budget is usually spent on long-term monitoring (LTM), of which a large percentage represents laboratory analytical costs. Energetics such as perchlorate (ClO_4^-), trinitrotoluene (TNT), and cyclotrimethylene-trinitramine (RDX) are among the most frequently detected in soils and groundwater at or near military installations due to their persistence and mobility. The US Army alone has reported to have >583 sites at 82 installations with energetics in groundwater, and 87 additional locations with suspected contamination. Currently, the standard protocol entails collecting samples in the field, packaging them, and shipping them overnight to a designated laboratory for analysis. This process requires significant sample preparation and handling, and analytical results may not be available for several days to weeks.

Objectives: The goal of this project was to develop a cost-effective, miniaturized sensor for rapid field detection and monitoring of ClO_4^-, TNT, and RDX in contaminated groundwater or surface water via fiber-optic surface enhanced Raman spectroscopy (SERS) techniques. Miniaturized sensors have the potential to significantly reduce analytical costs for LTM and to provide real-time results during field assessment and remediation activities. Our specific objectives were to (1) Construct an integrated field-portable SERS-based Raman sensor; (2) Design and develop sensitive and reproducible SERS substrates for energetics detection and analysis; (3) Develop and optimize methodologies for detecting energetics in contaminated groundwater or surface water; and (4) Evaluate the performance and cost effectiveness of the SERS technique for rapid field screening and monitoring of energetics at selected DoD sites.

Approach and Results: Using wet-chemical synthesis method, we successfully developed sensitive gold nanoparticle-based SERS substrates and demonstrated their applicability to detect ClO_4^-, TNT and RDX at concentrations as low as 10^{-9} M (~ 0.1 μg/L), 10^{-8} M (~ 2.3 μg/L), and 5×10^{-7} M (~ 0.12 mg/L), respectively. Using a process combining nanofabrication steps of pattern definition by electron beam lithography

(EBL), metal deposition, and reactive ion etching, we further developed and demonstrated large SERS enhancement factors exceeding 10^{11} resulting from a new configuration of elevated gold bowtie arrays with controllable gap sizes to < 8 nm. These new EBL-fabricated SERS substrates showed superior reproducibility and potential to be utilized for sensitive detection of energetics and other co-contaminants in groundwater and surface water. We subsequently developed and constructed a miniaturized, field-deployable sensor by integrating the SERS with a portable Raman analyzer equipped with a 300-mW near infrared laser and a fiber-optic probe. The performance of the potable Raman sensor was evaluated for detection and analysis of energetics both in laboratory and field. We showed the detection of ClO_4^-, TNT, and RDX at ppb to sub-ppm concentration levels in groundwater from a number of contaminated monitoring wells at several selected DoD military sites.

Benefits: Our results represent the first step in developing a SERS/Raman based field sensor that combines a portable Raman spectrometer with novel elevated gold bowtie arrays. The technology shows the potential to provide a tool for rapid, in-situ screening and analysis of energetics that are both important for environmental monitoring and of interest for national security. Future work can be directed to optimize the sensitivity and mass-production of SERS substrates and, through further technology validation and commercialization, a cost reduction of up to 50% may be realized using the portable Raman sensor because sample shipping and typical costs associated with laboratory analysis can be eliminated. The new technology also allows rapid turn-around of information to decision makers for site characterization and remediation.

1.0 PROJECT OBJECTIVES

The overall goal of this project was to develop a cost-effective, miniaturized sensor for rapid quantification and monitoring of energetics such as perchlorate (ClO_4^-), RDX and TNT in contaminated groundwater or surface water via fiber-optic surface enhanced Raman scattering (SERS) techniques. Our specific objectives were to:

1) Fabricate sensitive and reproducible SERS substrates using the state-of-the-art nano-fabrication techniques;
2) Construct a prototype fiber-optic SERS probe that is interfaced with a portable Raman spectrometer for field analysis;
3) Develop and optimize methodologies by incorporating molecular recognition techniques with improved selectivity and sensitivity for detecting energetics and other contaminants of concern; and
4) Evaluate the performance and cost effectiveness of the SERS technique for rapid field screening and monitoring of perchlorate and energetics at selected DoD sites.

2.0 BACKGROUND

2.1 Problem Statement and Contaminants of Concern

Rapid and real-time detection for environmental monitoring and security screening is a rapidly evolving field that is important for both environmental safety and national security. In particular, there is a significant need for compact and portable instruments that can perform on-site, sensitive, and accurate detection and identification of toxic and energetic chemicals, such as perchlorate (ClO_4^-), trinitrotoluene (TNT), cyclotrimethylene-trinitramine (RDX), and other chemical warfare agents and pollutants (CLAUSEN et al., 2006; KNEIPP et al., 1995; SYLVIA et al., 2000; WANI et al., 2003). Currently, the established detection and analysis methods for perchlorate in water are ion chromatography (IC) (EPA Method 314) and IC with electrospray ionization and mass spectrometry (IC/ESI/MS; EPA Method 6860) or high performance liquid chromatography with ESI and MS (HPLC/ESI/MS; EPA Method 6850), whereas TNT and RDX are analyzed primarily via HPLC with UV detection (EPA Method 8330b). All these conventional methodologies require sample collection and shipping as well as laboratory handling and, in the case of EPA Method 8330, a time-consuming pre-concentration step via solid-phase extraction is also needed. Each of these analytical techniques requires expensive analytical equipment and significant time for sample preparation and analysis. Moreover, typical turnaround times for explosives analysis by commercial laboratories are two weeks or longer. Therefore, costs for environmental analysis and monitoring represent a significant percentage of the total and future remedial expenses at many of the U.S. Department of Defense (DoD) contaminated sites. It has been reported that about 30 to 40% of the remediation budget is usually spent on long-term monitoring (LTM), of which a large percentage represents laboratory analytical costs. Rapid field detection and monitoring using miniaturized sensors thus has the potential to significantly reduce analytical costs for LTM, and to provide real-time results during site assessment work and other field remediation activities.

Among various contaminants found at DoD installations, perchlorate, TNT, and RDX are widely found in groundwater and surface water and are the focus of this study. Perchlorate is one of the most widespread contaminants in groundwater and surface water

at DoD military testing and training ranges (CLAUSEN et al., 2009; GU and COATES, 2006; SASS, 2004; SUIDAN et al., 2008). It is a key component of explosives and solid rocket fuels, although it is also present in a number of commercial products such as fireworks, road flares and Chilean nitrate fertilizers (BÖHLKE et al., 2005; GU and COATES, 2006). Perchlorate affects human thyroid function by inhibiting iodide uptake and may subsequently impact fetal development, which depends on hormones produced by the thyroid gland. Similarly TNT and RDX are among the most commonly used explosives, and each is frequently detected in soils and groundwater at or near military installations due to their persistence and high mobility (CLAUSEN et al., 2009; SUIDAN et al., 2008; WANI et al., 2003). For example, the US Army is reported to have 583 sites at 82 installations with explosives in groundwater, and 87 additional locations with suspected groundwater contamination (WANI et al., 2003). In addition, studies have shown that munitions compounds on many testing and training ranges are often heterogeneously distributed in surface soils, with localized concentrations ranging from 0.5 up to 10,000 mg/kg for samples collected only a few feet from each other (CROCKETT et al., 1998; MINA et al., 2003).

2.2 Surface Enhanced Raman Spectroscopy (SERS) Technology

Surface enhanced Raman scattering or spectroscopy (SERS) is a technique that provides orders of magnitude higher (10^4–10^{14}) enhanced Raman signal from analyte molecules that are either adsorbed onto or at the close proximity of specially prepared noble metal surfaces (GU et al., 2009; HATAB et al., 2010b; KNEIPP et al., 1997; NIE and EMORY, 1997; RUAN et al., 2007a; RUAN et al., 2006). Such surfaces are usually made with nanostructured gold (Au) or silver (Ag) arrays with nanometer gap sizes. Two mechanisms are known to account for the SERS effect (HATAB et al., 2010b; NIE and EMORY, 1997; ZHAO et al., 2006). The electromagnetic mechanism is believed to be responsible for the main enhancement that occurs as a result of the excitation of surface plasmons localized on roughened noble metal surfaces when illuminated by a laser light (Figure 1). The second mechanism is related to an increased polarizability of adsorbed analyte molecules due to specific interactions or coupling effects between the metal surface and the adsorbed molecule, although this mechanism has a smaller contribution to the

overall SERS enhancement. First demonstrated in 1974 (FLEISCHMANN et al., 1974), SERS has developed into a highly sensitive technique for detecting and analyzing a variety of chemical and biological agents. As a result, the SERS technique allows the detection of analyte molecules at ultra-trace to single molecular concentration levels (GU et al., 2009; HATAB et al., 2010b; KNEIPP et al., 1997; NIE and EMORY, 1997; RUAN et al., 2007a; RUAN et al., 2006). Thus, in comparison with fluorescence and optical absorption spectroscopic techniques, SERS is much more sensitive with greater molecular selectivity due to the molecular vibrational information provided by the Raman methodology. This is a significant advantage by using SERS since the surface selectivity and sensitivity extends Raman spectroscopy utility to a wide variety of applications previously impossible to achieve with normal Raman techniques.

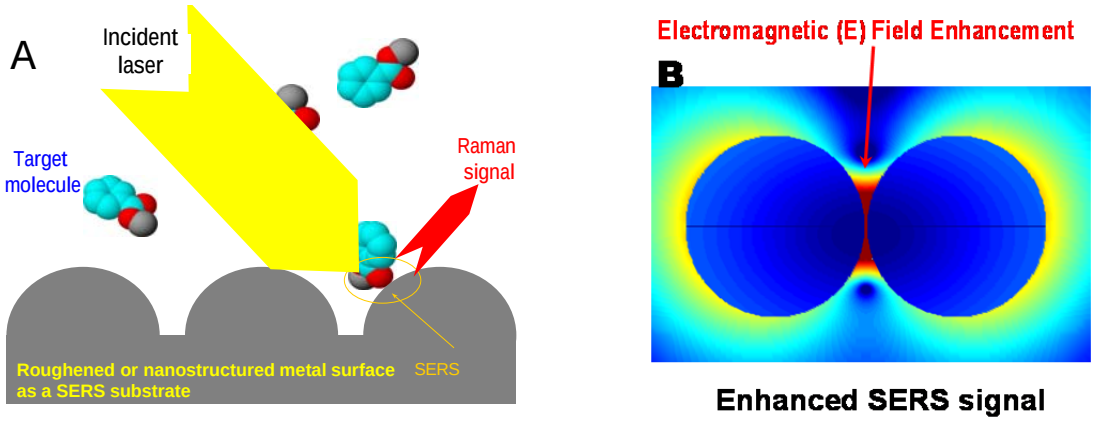

Figure 1. Schematic illustration of surface enhanced Raman scattering that occurs as a result of the excitation of surface plasmons localized on roughened noble metal surfaces when illuminated by a laser light.

The potential of SERS for trace analysis of explosives has been explored in recent years (KNEIPP et al., 1995; PRIMERA-PEDROZO et al., 2008; SYLVIA et al., 2000). In an early study, Kneipp and colleagues reported a minimum detection limit of 10^{-7} M for TNT adsorbed on gold and silver nanoparticles in laboratory prepared solutions (KNEIPP et al., 1995). More recently, a detection limit of 10^{-12} M for TNT was achieved by using synthesized Ag nanoparticles as a SERS substrate and by adjusting the pH of TNT aqueous solution (PRIMERA-PEDROZO et al., 2008). SERS was also found to be applicable for detecting the chemical vapor signature emanating from buried TNT-based landmines at

concentration level of 5 μg/L using a flow-through probe head design and electrochemically etched gold substrates (SYLVIA et al., 2000). Gold substrates produced by a nanosphere imprinting technique were also observed to be applicable for SERS detection of TNT as well as RDX and HMX but at relatively high concentrations (4.5×10^{-4} M) for both nitramines (PRIMERA-PEDROZO et al., 2008). Similarly, using Ag or Au-nanoparticles or ordered, Au-nanopillar substrates, we found that the methodology is sensitive for detecting perchlorate at trace concentrations in both laboratory synthesized and simulated groundwater (GU et al., 2004; RUAN et al., 2007b; RUAN et al., 2006; WANG and GU, 2005). In addition to the measurement of ClO_4^-, these Ag or Au substrate materials were found to be sensitive for the detection of nitrate, sulfate and radioactive uranium and technetium (GU and RUAN, 2007; RUAN et al., 2007c), potentially allowing multiple detection and analysis in a single measurement.

The vibrational spectrum generated using the Raman/SERS technique provides a "fingerprint" of the chemical composition of each agent. For example, perchlorate, RDX, and TNT all exhibit characteristic Raman scattering bands (or frequency shifts) due to their inherent chemical and structural features. The scattering bands of these energetics can thus be used for their identification and quantification (DOCHERTY et al., 2005). The strongest Raman frequency for perchlorate occurs at about 935 cm^{-1}. For RDX, the important –N-NO_2 vibrational frequencies are observed at about 1312 cm^{-1} (for symmetric stretch of NO_2) and 885 cm^{-1} (for symmetric ring stretch of RDX). For TNT, they are located at about 1367 cm^{-1} (for symmetric NO_2 stretch) and 829 cm^{-1} (for NO_2 bending vibration) (DOCHERTY et al., 2005; KNEIPP et al., 1995). Therefore, unlike conventional techniques such as ion or gas chromatography, SERS Raman analysis is specific because each compound of interest has unique molecular vibrational frequencies or fingerprints, as stated earlier. Simultaneous multi-component analysis is possible provided that the spectral overlap among different compounds is negligible or can be resolved. Furthermore, SERS is nondestructive and can be performed in aqueous solution under ambient conditions, thereby allowing direct analysis of environmental samples such as groundwater and surface water. The SERS technique also requires little or no sample preparation or pre-treatment and a small sample volume (usually microliters). It is rapid and virtually nondestructive. The availability of portable Raman spectrometers makes it possible to interface it with a

SERS probe, permitting rapid, in-situ field detection and analysis (MOORE and SCHARFF, 2009). Therefore, SERS based methods have the potential to reduce time, operational costs, and waste generated during the analysis while providing discriminative quantification of analytes in a single measurement.

3.0 TECHNICAL APPROACH

3.1 Wet-Chemical Synthesis and Fabrication of SERS Substrates

Wet-chemical synthesis and fabrication of noble metal nanoparticles and particle aggregates are among the most commonly used techniques for producing active SERS substrate surfaces. Using this method, either silver (Ag) or gold (Au) nanoparticles are synthesized using a series of chemical reactions such as reduction in an appropriate solvent solution, as illustrated in Figure 2A. Details about the synthesis methodology are given in Sections 4.1 and 4.2. Figure 2B shows some examples of as-synthesized Au nanoparticles [images taken by either transmission (TEM) or scanning electron microscopy (SEM)]. These nanoparticles are then used to form thin films (Figure 2C) through sedimentation or appropriate surface modification followed by self-assembly (detailed in Section 4.1), and the thin films are subsequently used as SERS substrates for measurements. Our initial studies were focused on the use of gold nanoparticles because gold shows superior chemical stability as compared with silver.

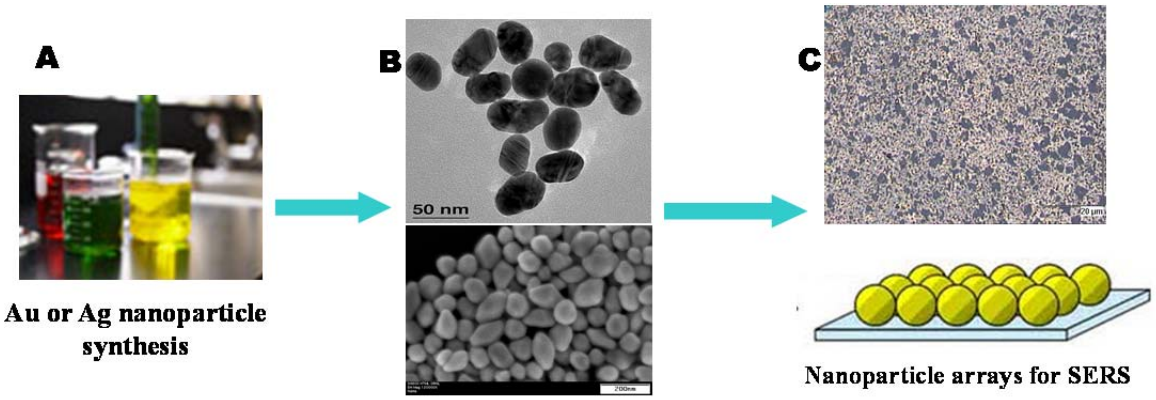

Figure 2. Illustration of wet-chemical synthesis of gold or silver nanoparticles, which are subsequently used to form nanoparticle thin films as SERS substrates for chemical analysis.

3.2 Electron Beam Lithography (EBL) and SERS Substrate Fabrication

One of the key challenges for SERS is the fabrication of noble metallic nanostructures that are highly reproducible and sensitive to target molecules. Unfortunately, the high enhancement (up to single molecule detection sensitivity) is usually

observed with randomly oriented metallic nanoparticles, from which only a minute fraction exhibits high SERS activity (often referred to as "hot spots") at the nanogap regions of nanoparticles (HATAB et al., 2010b; ZHAO et al., 2006). Additionally, these nanoparticle substrates are usually prepared by wet-chemical techniques and often have high sample to sample variability. It is difficult to achieve acceptable reproducibility for materials prepared from different batches or by different laboratories. For practical applications, it is imperative to develop SERS active substrates with reproducible and controllable SERS enhancement. To this end, substrates that show better reproducibility are prepared by physical means such as nanosphere lithography, laser ablation, dip pen nanolithography, and atomic force microscopy (CALZZANI et al., 2007; MOORE and SCHARFF, 2009). Advanced lithographic techniques such as focused ion beam and electron beam lithography (EBL) thus have been applied for precision nanofabrication (FROMM et al., 2004; KINKHABWALA et al., 2009; QIN et al., 2006) although these techniques also suffer from an inability to controllably fabricate the small gap sizes (e.g., <20 nm) that are necessary to achieve maximal SERS enhancement or sensitivity. It is thus one of our major objectives to develop, fabricate and optimize the sensitive and reproducible SERS substrates using the state-of-the-art nano-fabrication techniques.

As stated, the extreme sensitivity of SERS is dominated by the electromagnetic (E) enhancement, referring to the intense, spatially varying E fields produced by plasmonic coupling between closely spaced metal nanoparticles. A particularly intriguing feature of the electromagnetic enhancement is associated with the presence of the so-called "nanogap" effect where local SERS enhancement factors (EF) sufficient for detection of single molecules have been observed. Theoretical analysis using model systems consisting of closely spaced metal nanostructures have identified the size, shape, gap distance, the wavelength and polarization of the incident laser light as key factors that govern the overall EF within the nanogap. These advances in understanding the nanogap effect motivated new experimental approaches that, instead of searching for isolated hot spots or nanogaps in random nanoparticle aggregates, use EBL or physically fabricated periodic nanostructures.

EBL is among the most promising for fabricating SERS substrates with precisely defined shape and systematically variable nanogap size necessary for gaining insight into

the underlying enhancement mechanisms and for achieving maximal enhancement. Recent compelling examples include the demonstration of a strong polarization and gap size dependent response from single gold nanobowties fabricated by EBL, and the high harmonic generation by resonant plasmon field enhancement from a closely packed gold bowtie arrays. However, the large enhancement factors expected to occur for gap sizes on the order of a few nanometers remain difficult to achieve primarily because the resolution necessary for generating such features is beyond the capabilities of conventional EBL. Overcoming these technical hurdles promises advances in fundamental understanding of gap dependent *E* field coupling that enable design, fabrication, and practical application of a new generation of nanostructures that are capable of reliably and reproducibly performing sensitive molecule detection and spectroscopy.

The EBL equipment at the Center for Nanophase Materials Science (CNMS) at Oak Ridge National Laboratory (ORNL) was used as the primary tool for patterning and subsequent etching and deposition of SERS functional thin films. Figure 3 illustrates an EBL system with a field emission scanning electron microscope (SEM), Hitachi model S4700, interfaced with a pattern generator, Nanometer Pattern Generation System (NPGS) by JC Nabity Lithography Systems. EBL using an electron beam writer was also used for writing patterns on up to 10-cm silicon wafers.

Figure 3. A SEM based electron beam lithography (EBL) system at ORNL. It is interfaced with a pattern generator and nanometer pattern generation systems.

During this project, a variety of highly ordered SERS substrates were developed using EBL and Lift-off techniques (detailed in Section 4.3). These substrates include a series of two-dimensional models of squares, hexagonal, bowties (consisting of a pair of triangular prisms), and elliptical nano-arrays with varying sizes, heights, and nano-gap distances. In particular, novel elevated gold bowtie nanostructural array substrates were

found to be among the most effective in enhancing the SERS detection of energetics of interest to this work.

3.3 Sample characterization and Raman spectroscopic analysis

The fabrication of SERS substrate materials is complemented with imaging and surface characterization including scanning and transmission electron microscopy (TEM) and a wide array of scanning probe techniques. Scanning electron microscope (SEM) imaging of gold bowtie arrays was performed either with a JEOL JSM-7400F field emission SEM operated at 10 kV, or a FEI Nova 600 SEM focused ion beam system equipped with both a secondary electron detector and a backscattered electron detector. Lower resolution backscattered electron imaging was used in order to distinguish between Au and Si to show that the Au layer is present on gold nanoparticle arrays, and that the silicon posts are not coated with Au. This is because the contrast in the backscattered electron images is a function of the atomic number (Z) of the elements.

For the initial laboratory evaluation, the SERS spectra were measured using a desktop micro-Raman system equipped with a 300-mW near-infrared diode laser at an excitation wavelength of 785 nm (Renishaw Inc, New Mills, UK). Typical SERS spectra were collected at optical polarization of either parallel or perpendicular to the nanoparticle array. The laser beam was set in position with a 50×, 0.5-NA (numerical aperture) Leica microscope objective at a spatial resolution of about 2 μm. For all bowtie substrates, the polarization was set parallel to the bowtie axis with an output power of about 1 mW at the exit of the objective. Following the initial laboratory studies, SERS substrate samples were evaluated using a custom-made portable Raman spectrometer equipped with a fiber optic SERS probe (detailed in Section 4.4).

3.4 Theoretical Calculations and Model Simulation

Lumerical finite difference time domain (FDTD) Solutions software was used to calculate the electromagnetic field (E) intensity. A graphical representation of the E field intensity versus location in the plane of a periodic array of elevated gold bowtie structures (Figure 4), as an example, was used to calculate the location of the maximum enhancement.

Because a perfectly sharp tip at the apex of the triangular prism cannot be achieved experimentally, simulations of finite sharpness bowtie structures have been performed following previously established methods by either truncating the tips of the triangle or assuming a curvature at the apex. A simple geometry of the bowtie structure with truncated apexes is considered in the present study to elucidate the essential trends of how the near-field plasmon resonance varies with the gap size, d, and the truncation width, w. The Si post has a smaller x-y cross-section than the bowtie structure with edges also truncated. For simplicity, the Si post is assumed to be a cylinder in the simulations, and the central line of the cylindrical post is assumed to align with the centroid of the triangle with a size of 100 nm and a gold thickness of 40 nm. The diameter of the Si post is 40 nm, and a sorbed layer of the *p*-mercaptoaniline (*p*MA) analyte of 0.5 nm on the exposed gold surfaces is also assumed. The x-y dimensions of the unit cell adopted in simulations correspond to experimentally used center-to-center distance (*ccd*) and row-to-row distance (*rrd*) values of bowtie arrays. The dielectric properties of Au, Cr, and Si were taken from Palik's handbook, and the dielectric constant of *p*MA is 7. A plane wave (at 500 to 1000 nm wavelength) polarized across the junctions between triangles (i.e., along the x-direction) is illuminated in the negative z-direction of the bowtie. Because the laser illumination is polarized along the x-direction and the bowtie structure is periodic, anti-symmetric boundary condition is used at $x = 0$ and the upper boundary of x in the unit cell, whereas symmetric boundary condition is used at $y = 0$ and the upper boundary of y. Using these symmetric and anti-symmetric boundary conditions, only a quarter of the unit cell is required in simulations. Various simulation domains in the z-direction have been adopted to ensure the convergence of the simulation results, and the top and the bottom of the simulation domain are defined, respectively, at 360 nm above the Au bowtie and 100 nm below the Si post so that the total z-dimension of the simulation domain is 700 nm. The perfectly matched layers are used at the top and the bottom of the simulation domain to completely absorb waves leaving the simulation domain in the wave propagation direction. The mesh sizes in the bowtie region (including analyte, gap, and Cr layer) vary from 0.25 to 1 nm, and automatic graded mesh with a mesh accuracy of 4 is used in the region outside the bowtie.

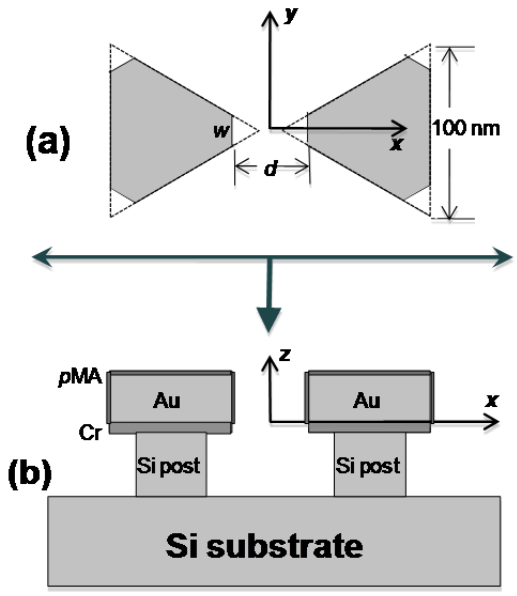

Figure 4. Schematic illustration (not to scale) of the top view of a bowtie structure in the *x*-*y* plane (a) and the cross-section in the *x*-*z* plane (b). The height of the gold bowtie is 40 nm with a sorbed analyte layer of 0.5 nm of *p*-mercaptoaniline (*p*MA). The Cr adhesion layer is 8 nm, the Si post diameter is 40 nm, and the post height is 200 nm.

3.5 Determination of SERS enhancement factors

For the evaluation of the sensitivity and performance of as-prepared SERS substrates, thionine or *p*-mercaptoaniline (*p*MA) were initially utilized as probing molecules for the determination of Raman enhancement factors because these molecules can form a monolayer on Au or Ag surfaces (HAYNES and VAN DUYNE, 2003; JACKSON and HALAS, 2004). For example, the self-assembled monolayer of *p*MA was prepared by exposing the Au bowtie arrays to an aliquot of freshly prepared aqueous solution of *p*MA at 10^{-5} M (1.5 mL) in a plastic petri-dish for 12 hours at room temperature. Samples were then rinsed in a solution containing 10% ethanol and 90% deionized water (18.2 MΩ) to remove unbound *p*MA and dried with a flow of N_2. The maximum SERS signal was obtained by focusing the laser beam on the substrate, and the spectral data (N = 8–13) were collected by moving the stage at ~10 μm intervals (one spectral acquisition per step) over ~ 1600 μm^2 area. Spectral data were analyzed using the Galactic GRAMS software for each substrate pattern with different gap sizes and inter-bowtie distances. Using Au bowtie arrays as an example, a typical set of spectra was collected from 13 different spots on a 1600 μm^2

bowtie array in order to evaluate the reproducibility of the substrate arrays. The SERS enhancement factor (*EF*) was then calculated based on Eq. 1 below:

$$EF = \frac{I_{SERS}}{I_{bulk}} \frac{N_{bulk}}{N_{SERS}} \quad (1)$$

where the SERS integrated band area at 1588 cm^{-1} (I_{SERS}) (one of the strongest Raman band for *p*MA) is divided with that of the nonenhanced Raman signal of the same band (I_{bulk}). N_{bulk} and N_{SERS} are the number of molecules for the neat bulk sample (without SERS enhancement) and that excited by the localized field between the two triangles making up the bowties in the SERS measurement. An N_{bulk} of 3.1×10^{13} in the laser spot was estimated based on the focusing volume and a density of *p*MA of 1.06 g/cm^3. N_{SERS} was calculated according to a previously established method where it was assumed that the *E* field enhancement that contributes to the SERS signal is at the tips of the triangles that form the bowtie gap. Since the two triangles have the same area of field enhancement and the *p*MA molecules uniformly cover the Au surfaces of the bowtie, the area is calculated as a cylinder with the Au film thickness of 40 nm being the height of the cylinder. The area of the cylinder consists of two cylindrical halves with a radius of curvature of 15 nm representing the sides of the gold bowties as a conservative estimate, and two circles with the same radius representing the top (at the tip area) of the bowties. Accordingly, the estimated N_{SERS} is 1.1×10^6 for ccd = rrd = 300 nm, $2.2\text{x}10^4$ for ccd = rrd = 2 μm, and 6.7×10^4, for ccd = 785 nm and rrd = 2 μm bowtie arrays based on a packing density of 0.20 nm^2/molecule of *p*MA.

3.6 Portable Raman Sensor and Field Sample Analysis

During the course of this SERDP project, we developed a portable Raman sensor by integrating the SERS substrate developed in our laboratory and a commercial Raman analyser (Figure 5). The initial configuration of the portable Raman sensor included a EZRaman-M system equipped with a fiber optic probe (Figure 5a). However, this portable Raman system was found lacking the required sensitivity and rigidity (due to its optical fiber broken down during transportation). An improved portable Raman sensor was later developed by integrating an EZRaman-I system equipped with a cooled charge-coupled

device (CCD) detector (up to -50°C for improved sensitivity) and stainless steel-encased optic fiber. The entire sensor system was also fitted in a 6×12×18-inch casing for improved rigidity and portability (Figure 5b). However, both of these portable Raman systems are equipped with a diode laser operating at 785 nm as the excitation source. The fiber optic probe serves three purposes: (1) transmission of the incident laser to excite the sample, (2) collection of the scattered Raman signal to the spectrometer detector, and (3) removal of unwanted background signals through an optical filtering device. Each spectrum was accumulated over a period of 60 s and analyzed by ThermoGalactic GRAMS software. Additional details in the design and evaluation of the portable Raman sensor are provided in Section 4.4.

Figure 5. An integrated portable Raman sensor by coupling a fiber-optic SERS probe with a commercial Raman analyser: (a) EZRaman-M system or (b) EZRaman-I system.

4.0 METHODS, RESULTS, AND TECHNICAL ACCOMPLISHMENTS

4.1 Evaluation of SERS Technology for Perchlorate Detection

For the initial evaluation of the applicability of SERS technology for energetics detection, we first used colloidal gold nanoparticles or particle aggregates as SERS substrates according to our previously established methodologies (GU and RUAN, 2007; OLSON et al., 2001). This part of the work forms the basis for further developing SERS substrates using EBL techniques since relatively few studies have used SERS for energetics detection and analysis. We first used self-assembled Au nanoparticles for the detection and analysis of perchlorate in both simulated and field groundwater samples as described below.

4.1.1 Materials and Methods: Perchlorate Detection

All chemicals used in this experiment were of reagent grade or better. Gold chloride trihydrate ($HAuCl_4 \cdot 3H_2O$), nitric acid (HNO_3) (70%), 2-(dimethylamino)-ethanethiol hydrochloride (DMAE) [$(CH_3)_2NCH_2CH_2SH \cdot HCl$] (98%), sodium citrate ($Na_3C_6H_5O_7$) (98%), sodium borohydride ($NaBH_4$) (98%), and hydrochloric acid (HCl) (36.5%) were obtained from Aldrich (St. Louis, Missouri). Sodium perchlorate ($NaClO_4 \cdot H_2O$) was purchased from EM Science (Cherry Hill, New Jersey). Micro-glass slides were from Corning Glass Works (Corning, New York). For substrate and solution preparations, deionized water (18.2 MΩ cm^{-1}) was used throughout the experiment. All glassware was cleaned in a freshly prepared acid bath and rinsed thoroughly with deionized water prior to use.

Colloidal Au nanoparticles were prepared according to previously published methods (GU and RUAN, 2007; OLSON et al., 2001). In brief, a "seed" colloidal suspension of Au was first prepared by mixing 1 mL of 1% aqueous $HAuCl_4 \cdot 3H_2O$ in 100 mL of H_2O with vigorous stirring for about 1 min, followed by sequential additions of 1 mL of 1% trisodium citrate and 1 mL of 0.075% $NaBH_4$ in 1% trisodium citrate. This seed Au suspension was stirred continuously for an additional 5 min and then stored at 4°C. Au nanoparticles of ~54 nm in diameter were then prepared by heating 900 mL of dilute

$HAuCl_4$ solution (~0.004%) to boiling, followed by the addition of 1 mL of the "seed" Au nanoparticles and 3.6 mL of a 1% trisodium citrate solution. The solution mixture was refluxed for an additional 10 min before it was cooled under stirring. The average size of synthesized Au nanoparticles (~54 nm) was determined by means of dynamic light scattering using a ZetaPlus particle size analyzer (Brookhaven Instruments, Holtsville, New York). Data were collected for every batch of the Au colloid at room temperature.

DMAE-modified Au nanoparticles were prepared by adding 0.28 g DMAE into 400 mL of the above prepared Au colloid suspension, upon which the color of Au colloids immediately turned from red to deep purple, suggesting the aggregation of Au nanoparticles by interacting with DMAE. The UV-visible spectrum showed a red shift in its primary absorption maxima from 525 to 790 nm, the latter of which is attributed to multipolar resonances of Au nanoparticles in higher-order coupled spheres (WEISBECKER et al., 1996; ZHONG et al., 2004). After mixing for approximate 5 h, the suspension was centrifuged at 14,000 rpm, and the concentrated Au nanoparticles were collected, washed with deionized water, re-suspended in 0.01 M HCl solution (pH ~2), and then used as SERS substrates for perchlorate detection. This concentrated Au nanoparticle suspension was found to be stable for at least 8 months, although ultrasonification was necessary to ensure well dispersed Au colloids before use.

For SERS analysis, the analyte ClO_4^- solution in the concentration range of 10^{-9} to 10^{-4} M was prepared by dilution in series (10×) from a stock solution of 10^{-3} M in deionized water. To evaluate potential matrix interferences from competing ions, measurements were also performed in a synthetic groundwater (SGW) consisted of a mixture of SO_4^{2-}, PO_4^{3-}, and NO_3^- each at 10^{-4} M and Cl^- at 10^{-3} M, respectively. In addition, two contaminated groundwater samples (GW-1 and GW-2) were obtained from a DoD field site and used for testing. Table 1 lists major anionic compositions and pH of the site groundwater samples and SGW. The analyte and SGW or GW samples (0.1 mL) were then mixed with 0.1 mL of the modified Au nanoparticle concentrate and 0.8 mL of water for analysis. A small drop (~10 μL) of the mixed suspension was placed on a glass slide, air-dried, and SERS spectra were collected after about 30 min.

Table 1. Major anionic composition of two field contaminated groundwater samples (GW-1 and GW-2) and a simulated groundwater (SGW).

Property	SGW	GW-1	GW-2
Perchlorate (μM)	0 – 1	8.3	0.01
Chloride (mM)	1.0	0.28	3.0
Sulfate (mM)	0.1	0.16	0.49
Nitrate (mM)	0.1	0.16	0.52
Phosphate (mM)	0.1	ND*	ND
Bicarbonate (mM)	0	2.8	3.1
pH	6.5	7.3	8

* ND = not detected.

As described earlier, Raman spectra were obtained using the Renishaw micro-Raman system equipped with a near-infrared diode laser at a wavelength of 785 nm for excitation (Renishaw Inc, New Mills, UK) (GU and RUAN, 2007; GU et al., 2004; RUAN et al., 2006). The laser beam was set in position with a Leica Raman imaging microscope equipped with a 50× objective lens (0.5 numerical aperture) at a lateral spatial resolution of ~2 μm. The optics polarization was set perpendicular to the laser, and its intensity at the exit of the objective lens was ~1 mW by using a set of neutral density filters. A CCD array detector was used to achieve signal detection from a 1200 grooves/mm grating light path controlled by Renishaw WiRE software and analyzed by Galactic GRAMS software.

4.1.2 Results and Discussion: Perchlorate Detection

Quantitative Analysis of Perchlorate: SERS spectra of perchlorate were first examined at concentrations ranging from 10^{-10} to 10^{-6} M in purified water (Figure 6A). Each spectrum in Figure 6A was offset for the clarity of presentation. The primary Raman scattering peak (due to symmetric stretching vibration) of ClO_4^- occurred at about 934 cm^{-1},

which is consistent with literature data using both normal and surface enhanced Raman spectroscopic techniques (GU et al., 2004; MOSIER-BOSS and LIEBERMAN, 2003a; RUAN et al., 2006; TAN et al., 2007). The lowest ClO_4^- concentration detected was about 10^{-10} M (~ 10 ng/L), and a small ClO_4^- peak was visible (spectrum b). However, the detection limit was estimated at 10^{-9} M (or ~100 ng/L) with a signal to noise ratio >3. These results suggest that the SERS technique is highly sensitive for ClO_4^- detection using DMAE-modified Au nanoparticle substrates. This detection limit is about two orders of magnitude lower than those reported by using either cystamine-modified gold nanoparticles (RUAN et al., 2006) or positively charged silver nanoparticles sorbed with polyethyleneimine fragments (containing primary amino and amide functional groups) (TAN et al., 2007). These previous techniques give a relatively high background scattering as a result of the complicated molecular structures of the organic modifiers (both cystamine and polyethyleneimine or its fragments) (RUAN et al., 2006; TAN et al., 2007). The background scattering in the spectral region between 900 and 950 cm^{-1} could interfere with the detection of ClO_4^- or overlap with the Raman band of ClO_4^-, especially at sub-micromolar concentrations. On the other hand, no significant background Raman scattering was observed in the spectral region of ~890–960 cm^{-1} using DMAE-modified Au nanoparticles as SERS substrates.

The rationale for using DMAE as a modifier or a molecular recognition agent is based on the development of selective ion-exchangers for ClO_4^- sorption, in which the selectivity is found to strongly depend on the charge and size of the quaternary alkyl-ammonium functional groups (GU and BROWN, 2006; GU et al., 2007). The electrostatic attraction between ClO_4^- anions and positively charged, DMAE modified Au nanoparticles, enables a close contact and the concentration of ClO_4^- onto Au-nanoparticle surfaces (GU et al., 2004; RUAN et al., 2006). Additionally, the amine functional groups could have facilitated the aggregation of Au nanoparticles, which is necessary to obtain strong electromagnetic plasmon enhancement on gold metal surfaces (KNEIPP et al., 1999; NIE and EMORY, 1997; ZHAO et al., 2006). Theoretical calculations have shown that the maximal SERS signal could be obtained when the analyte molecule is situated within the nanoneck regions of adjacent metal nanoparticles, where maximal electromagnetic field enhancement is achieved upon laser excitation (XU et al., 2000; ZHAO et al., 2006).

Therefore, the use of DMAE-modified Au SERS substrates offers advantages in sensitive detection of ClO_4^- in aqueous media. It yielded an enhancement factor of about 10^7–10^8 because, by using normal Raman spectroscopy (or without using Au nanoparticles), no Raman signal could be detected directly from the aqueous solution at ClO_4^- concentrations below 10^{-2} M (RUAN et al., 2006).

Analysis of the spectra (Figure 6A) also showed that the Raman band at 934 cm^{-1} increased consistently with an increase of aqueous ClO_4^- concentrations. A logarithmic plot between the peak intensity and the ClO_4^- concentration yielded a linear relationship over a wide concentration range between 10^{-10} and 10^{-6} M (Figure 6B). This observation is consistent with that observed for the detection of pertechnetate (TcO_4^-) ions using similar techniques (GU and RUAN, 2007). Sackmann and Materby (2006) also reported that the SERS intensity of adenine increased exponentially with its concentration when silver colloids were used as a SERS substrate. These observations suggest that the technique could potentially be used as a quantitative or semi-quantitative tool for the analysis or rapid screening of perchlorate in aqueous media.

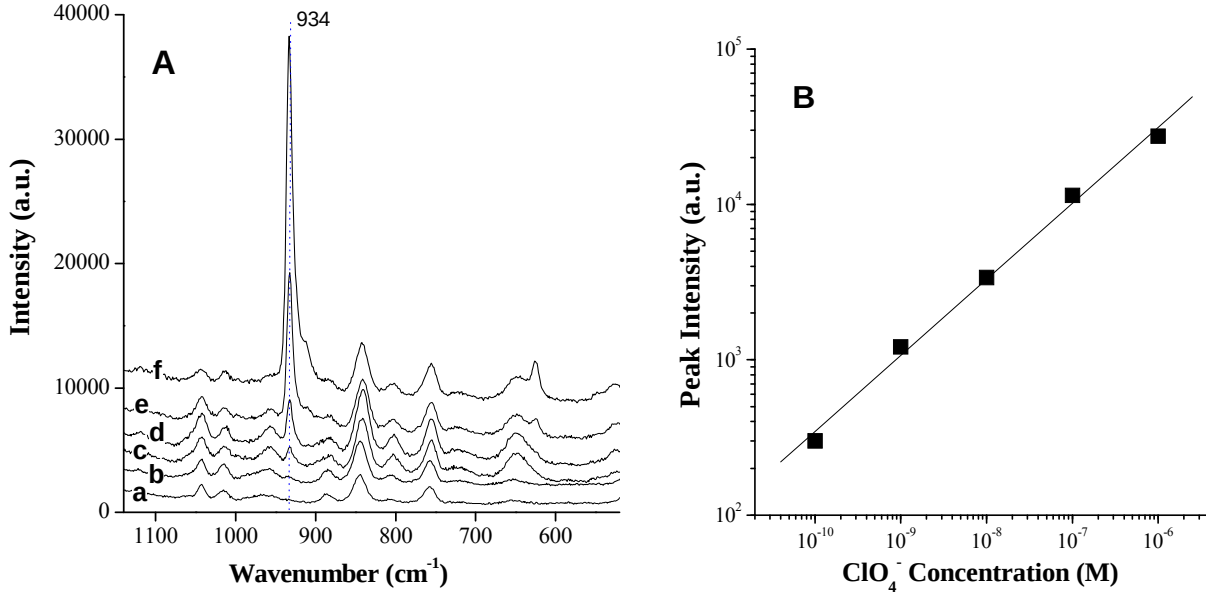

Figure 6. (A) Raman spectroscopic analysis of ClO_4^- at concentrations of a: 0, b: 10^{-10}, c: 10^{-9}, d: 10^{-8}, e: 10^{-7}, and f: 10^{-6} M using DMAE-modified Au nanoparticles as a SERS substrate; (B) a log-log plot of the peak intensity at 934 cm^{-1} against the ClO_4^- concentration.

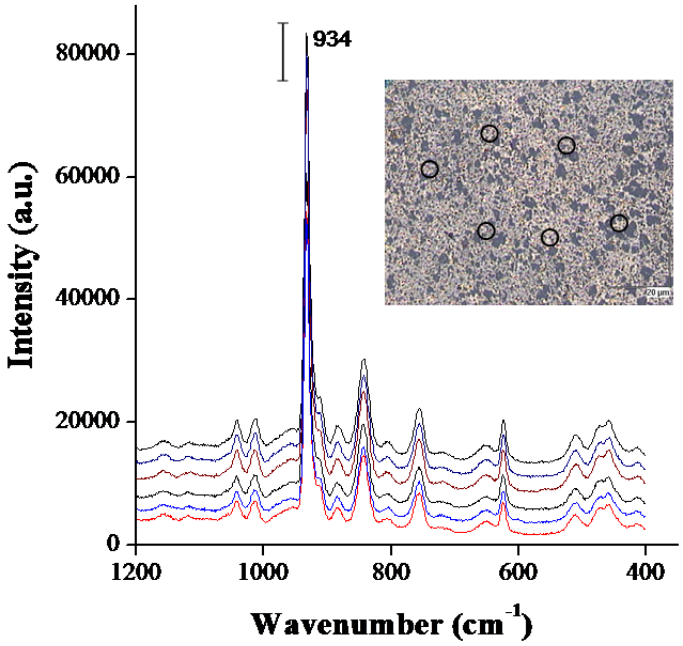

Figure 7. SERS spectra of ClO_4^- (1×10^{-5} M) obtained from six randomly selected spots (inset) on a substrate made of DMAE-modified Au nanoparticles. Each spectrum was offseted for the clarity of presentation, and the error bar represents a standard deviation of about 16% at peak position 934 cm^{-1}.

The surface modification of Au nanoparticles with DMAE enabled not only a high sensitivity but also a fairly good reproducibility in detecting ClO_4^- in aqueous solution. The spot-to-spot reproducibility of Raman signal at 934 cm^{-1} was evaluated by randomly selecting about 6 spots under the microscope and measuring their corresponding SERS spectra (Figure 7). Results indicate that the standard deviation of the peak intensity at 934 cm^{-1} was about 16% from six different spots. Similarly, the batch-to-batch variations were found to be about ±15% when different batches of the modified Au nanoparticles were used. These observations are attributed to the fact that the positively-charged amine functional groups result in the sorption and thus a good distribution of ClO_4^- on Au nanoparticles. Also as indicated earlier, the amine functional groups could have facilitated the aggregation of Au colloids, as evidenced by the self-assembly of DMAE-modified Au nanoparticles (Figure 7, inset). Without surface modification, the analyte would be distributed unevenly after drying or crystallization on metal nanoparticle surfaces (one of the contributing factors to observations of so-called "hot spots"). The probability of finding such hot spots is usually extremely low for detecting the target analyte (KNEIPP et al., 1999;

NIE and EMORY, 1997). Nie and Emory have shown that about one in 100–1,000 silver colloids are perhaps "hot" or SERS-active (NIE and EMORY, 1997). This has been a major limiting factor for the use of SERS as a routine analytical tool.

Analysis of Perchlorate in Contaminated Groundwater Samples. To assess the potential interferences in the quantitative analysis of ClO_4^- in realistic contaminated water samples, we further examined the detection of ClO_4^- in the presence of background electrolytes including SO_4^{2-}, PO_4^{3-}, and NO_3^- at ~ 10^{-4} M and Cl^- at 10^{-3} M. In initial studies, test water was prepared with these competing anions. These anion concentrations are orders of magnitude higher than those expected for ClO_4^- in groundwater. The resulting SERS spectra are shown in Figure 8A at perchlorate concentrations of 10^{-9} to 10^{-6} M (0.1 to 100 μg/L). In comparison with those shown in Figure 6A, the general features of the spectra remain unchanged with exception of the band at 1045 cm^{-1} (Figure 8A), which was assigned to the stretching vibration of the NO_3^- ion. However, we note that the peak intensity at 1045 cm^{-1} decreased with increasing concentrations of ClO_4^- in solution, especially at concentrations of 10^{-7} and 10^{-6} M. These observations suggest possible

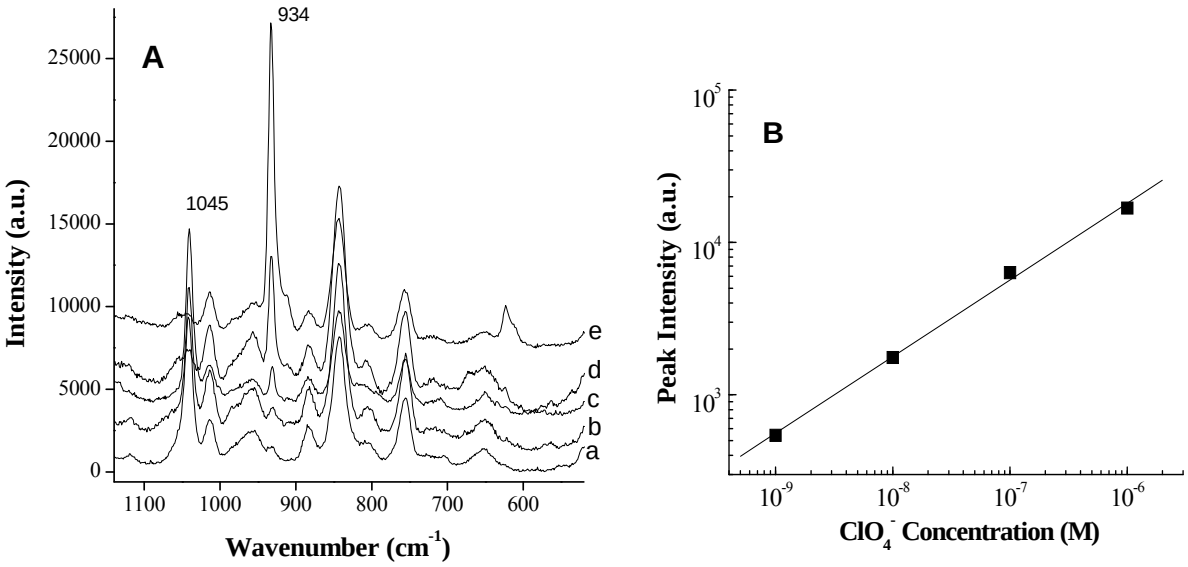

Figure 8. (A) SERS spectroscopic analysis of ClO_4^- in the presence of background electrolytes of SO_4^{2-}, PO_4^{3-}, and NO_3^- at 10^{-4} M each and Cl^- at 10^{-3} M. Perchlorate concentrations varied from a: 0, b: 10^{-9}, c: 10^{-8}, d: 10^{-7}, to e: 10^{-6} M. (B) A log-log plot of the peak intensity at 934 cm^{-1} against the ClO_4^- concentration.

competitive interactions between ClO_4^- and NO_3^- ions for sorption onto the Au nanoparticle substrate. The fact that the nitrate band at 1045 cm^{-1} was substantially suppressed could be attributed to the preferential sorption of ClO_4^- ions because of limited sorption sites on DMAE-modified Au nanoparticles. Similar observations have been reported when cystamine-modified Au nanoparticles were used for the detection of ClO_4^- and NO_3^- (RUAN et al., 2006).

Although SO_4^{2-} and PO_4^{3-} show vibrational bands at about 980 and 925 cm^{-1}, respectively (NIAURA and JAKUBENAS, 2001), their Raman scattering apparently was not enhanced by using DMAE-modified Au nanoparticles as a SERS substrate and thus did not significantly interfere with the detection of ClO_4^- ions (Figure 8). These results suggest that the SERS substrate enhanced the Raman scattering only for some selected anionic species, although exact mechanisms by which the Raman scattering of different ions or molecules is selectively enhanced remain a subject of intensive investigation (KNEIPP et al., 1999; NIAURA and JAKUBENAS, 2001; NIE and EMORY, 1997; RUAN et al., 2006; RUAN et al., 2007c; ZHAO et al., 2006). One possible explanation is that SO_4^{2-} and PO_4^{3-} ions are only weakly sorbed on the SERS substrate because of their relatively high hydration energy as compared with that of the ClO_4^- ion (GU and BROWN, 2006). However, we note that the presence of these background ionic species caused an overall decrease in peak intensity at 934 cm^{-1} for perchlorate. For example, at the ClO_4^- concentration of 10^{-6} M, its peak intensity decreased about 35% as compared with that measured in deionized water (Figure 6A). Such a decrease in peak intensity of ClO_4^- can be expected because of the presence of 2–5 orders of magnitude higher concentrations of background ionic species (NO_3^-, SO_4^{2-}, PO_4^{3-}, Cl^-), which may compete for interactions with the SERS substrate and thus reduce the scattering signal of ClO_4^-. On the other hand, the presence of these background electrolytes did not appear to significantly impact on the quantitative analysis of ClO_4^-. A plot of the peak intensity (at 934 cm^{-1}) and the ClO_4^- concentration yielded a fairly linear relationship on a log scale (Figure 8B). These results again indicate that the DMAE-modified Au SERS substrates could be used for quantitative or semi-quantitative analysis of ClO_4^- in aqueous media. Thus, the technique has significant potential to be used as a screening tool for environmental analysis under real world conditions.

We further analyzed two contaminated groundwater samples obtained from a field site. The groundwater GW-1 contained ClO_4^- at a concentration of 8.3×10^{-6} M, which is about 3 orders of magnitude lower than those of competing ions. The other sample (GW-2) had a ClO_4^- concentration of 1×10^{-8} M, which is 5–6 orders of magnitude lower than those of competing ions in the water. These samples were analyzed as is or diluted 10 times with deionized water, and the results are shown in Figure 9. Using Figure 8B as the standard calibration curve, the calculated ClO_4^- concentrations were 7.86×10^{-6} and 1.02×10^{-8} M for undiluted GW-1 and GW-2 samples, respectively. These data are in general agreement with those analyzed by ion chromatography (EPA Method 314.0), which were 8.3×10^{-6} and 1×10^{-8} M, respectively. However, for 10× diluted samples, the SERS analysis substantially overestimated the ClO_4^- concentrations, which were 3.43×10^{-5} and 1.15×10^{-8} M for the GW-1 and GW-2 samples. This observation is not surprising because the background electrolyte concentrations in diluted samples were substantially lower than those used in the calibration "standards" (Figure 8B). As a result, an increased SERS signal was observed for ClO_4^- because of less matrix interference in diluted samples. However, by

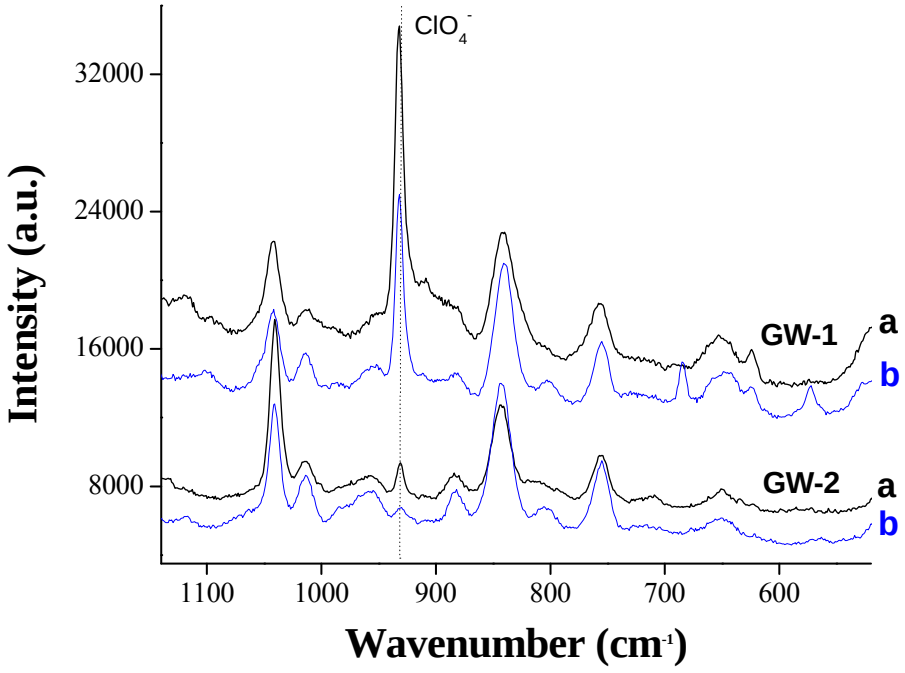

Figure 9. SERS spectra of two contaminated groundwater samples (GW-1 and GW-2) without dilution (a) or with a 10x dilution (b).

using the calibration curve in Figure 6B (in deionized water), the calculated ClO_4^- concentration in GW-1 was 1.08×10^{-5} M, which is close to its true value measured by the ion chromatography. These results thus emphasize the need to prepare samples and reference standards in the same or similar matrixes, as a common practice used in any quantitative analysis. For practical applications, standard addition techniques may be used to correct matrix interferences and thus to ensure good reproducibility in quantitative analysis.

4.2 Evaluation of SERS Technology for Cyclotrimethylenetrinitramine (RDX) Detection

4.2.1 Materials and Methods: RDX Detection

Similar to ClO_4^- detection, we initially used colloidal Au nanoparticles as a SERS substrate for detecting cyclotrimethylenetrinitramine (RDX). RDX reference standard (1 mg/mL in acetonitrile) was purchased from AccuStandard, Inc. Thionine, $HAuCl_4$, CTAB, trisodium citrate hydrate, and sodium borohydride were obtained from Aldrich. The Au nanoparticles were prepared similarly as described above. In brief, Au seeds were first prepared and used to grow larger nanoparticles in the presence of CTAB, additional $HAuCl_4$, and ascorbic acid as a reducing agent. Citrate was used as a capping agent, and the gold seeds were observed to be stable for at least one month in aqueous solution. Gold nanoparticles with different sizes were subsequently synthesized as follows. A 100 mL vial and four 45-mL vials were labeled "Vial 1" through "Vial 5". To each of these vials, 8 mL of 2.5×10^{-3} M $HAuCl_4$ and 0.5 mL 1×10^{-3} M CTAB were added, followed by the addition of 70 μL of freshly prepared ascorbic acid solution (0.10 M) under gentle stirring. The seed solution (3 mL) was then added to Vial 1 and, after 1 min, the Vial 1 suspension (11.5 mL) was drawn and added to Vial 2 with gentle stirring. This procedure was repeated from Vial 2 to Vial 5, and the ending Au nanoparticle suspension (Vial 5) was stored in the refrigerator for 48 h before use. Excess CTAB was removed by centrifugation and washing with deionized water three times.

RDX working standard solutions of 10^{-7} to 10^{-4} M (~ 0.022 mg/L to 22 mg/L) were prepared from a stock solution of 8×10^{-4} M by diluting the reference standard in DI water. SERS samples were prepared by mixing 0.5 mL of the Au nanoparticle suspension with

250 μL of RDX standard solutions at different concentrations. This mixed RDX and Au nanoparticle suspension (50 μL) was then placed on a glass slide for SERS analysis after the droplet was air-dried. The calibration curves and the reproducibility studies were performed on the same day to minimize error associated with instrument variability. SERS spectra were obtained using a Renishaw micro-Raman system as described earlier.

To evaluate the applicability of SERS technique to detect RDX in the environment, a contaminated groundwater sample was obtained from a US Navy facility in Virginia and used as received. This sample had mildly acidic pH and contained 18 mg/L of total organic carbon (TOC). Major cations and anions included sulfate (21.5 mg/L), chloride (18.0 mg/L), sodium (39.7 mg/L), magnesium (7.65 mg/L), calcium (19.7 mg/L) and potassium (7.5 mg/L). The analysis was performed by the standard addition method, in which 15 mL volumes of the groundwater sample (with an unknown concentration of RDX) were spiked with 0, 50, 70, 175, or 300 μL of a stock solution of RDX (at 177.7 mg/L). The final volume was made up to 25 mL with DI water. The characteristic Raman band intensity at 874 cm^{-1} for RDX for each sample was plotted against the final added concentration of RDX, and a linear regression routine was used to calculate the absolute value of the X-intercept, which is equal to the concentration of RDX in groundwater.

4.2.2 Results and Discussion: RDX Detection

The detection of RDX explosive using Au nanoparticles was first performed at varying RDX concentrations ranging from 10^{-4} to 10^{-6} M. The resulting SERS spectra are shown in Figure 10a. All spectra were collected in the range from 300 to 2000 cm^{-1} to cover most Raman bands of RDX along with the conventional Raman spectrum of pure RDX for comparison. Since only the vibrational modes of analyte moieties adsorbed on the Au surface are enhanced, there are typically fewer peaks in the SERS spectrum than in the conventional Raman spectrum (without using Au as a SERS substrate). This observation is consistent with those reported in literature (KARPOWICZ and BRILL, 1984; TORRES et al., 2004). The typical Raman band assignments for RDX are as follows: the band at 874 cm^{-1} is attributed to the symmetric ring vibration mode; the band at 930 cm^{-1} is assigned to ring stretching and N-O deformation; the band at 1258 cm^{-1} is due to CH_2 scissoring and N-N

stretching vibration (KARPOWICZ and BRILL, 1984); the band at 1312 cm^{-1} results from CH_2 bending; the band at 1370 cm^{-1} is υNO_2 symmetric stretching vibration and βCH_2 scissoring; finally, the band at 1560 cm^{-1} is attributed to the υNO_2 asymmetric stretch in nitro amines (KARPOWICZ and BRILL, 1984; TORRES et al., 2004).

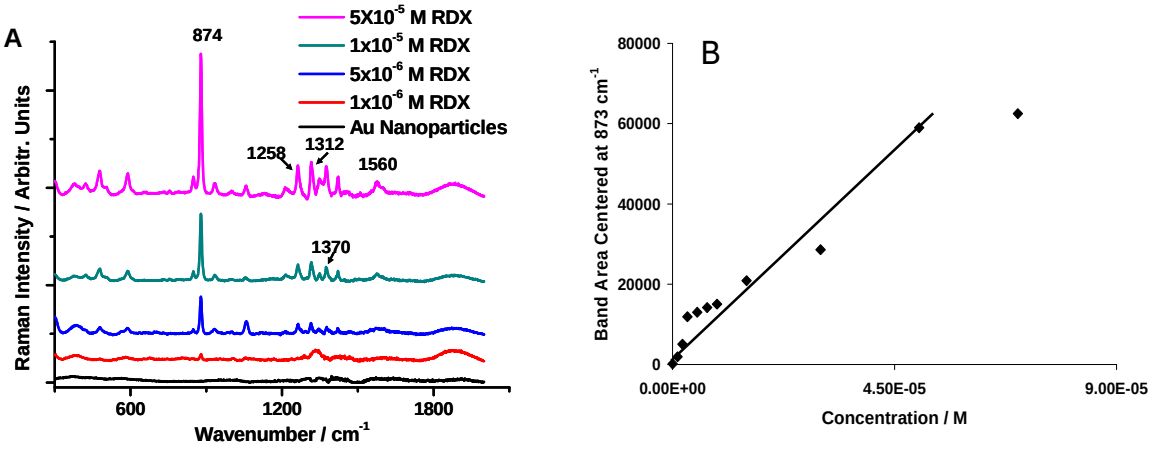

Figure 10. (A) SERS spectra of RDX at concentrations ranging from 1×10^{-6} M to 5×10^{-5} M. Laser power was ~1 mW at the exit of the microscope objective, and the scan time was ~10s. (B) Peak area at 873 cm^{-1} as a function of RDX concentration.

The strongest SERS Raman band for RDX occurred at 874 cm^{-1} and its intensity increased with an increase in the aqueous RDX concentration (Figure 10A). SERS spectra of RDX at different concentrations showed that most of the bands can be identified at the lowest concentration of 1×10^{-6} M RDX with the background being negligible. On the basis of previously established techniques (Section 3.5), the calculated *EF* for SERS detection of RDX explosive was about 6×10^{4}, based on the maximum adsorbed RDX molecules of approximately 4.65×10^{6} per Au particle (DING et al., 2006). This EF is higher than that previously observed for thionine by our group (RUAN et al., 2007d). The enhancement, which can be attributed to an enhanced electromagnetic field upon laser excitation, is consistent with many theoretical and experimental studies showing that a large SERS enhancement occurs when the analyte is situated at the junction or nanoneck of two adjacent Au nanoparticles (FREEMAN et al., 1995; JIANG et al., 2003; MICHAELS et al., 2000).

Quantitative SERS analysis of RDX at different concentrations was evaluated (Figure 10B). The characteristic peak area at 874 cm^{-1} was integrated through the instrument software and plotted as a function of the RDX concentration. The linear dynamic range for SERS analysis of RDX was found from the lower detection limit of 1×10^{-6} M to 5×10^{-5} M. The band area increased linearly with RDX concentration throughout this range, but linearity was lost when the RDX concentration exceeded 5×10^{-5} M. This detection limit (1×10^{-6} M or 0.22 mg/L) is more than two orders of magnitude lower than that previously reported in literature (4.5×10^{-4} M or 100 mg/L) using SERS analysis (CALZZANI et al., 2008). However, we note that the previous study used a Au coated polystyrene nanosphere film as the SERS substrate and data were recorded using a portable Raman spectrometer. The reported differences in sensitivity are partially attributed to the use of different SERS substrates and instrumentation.

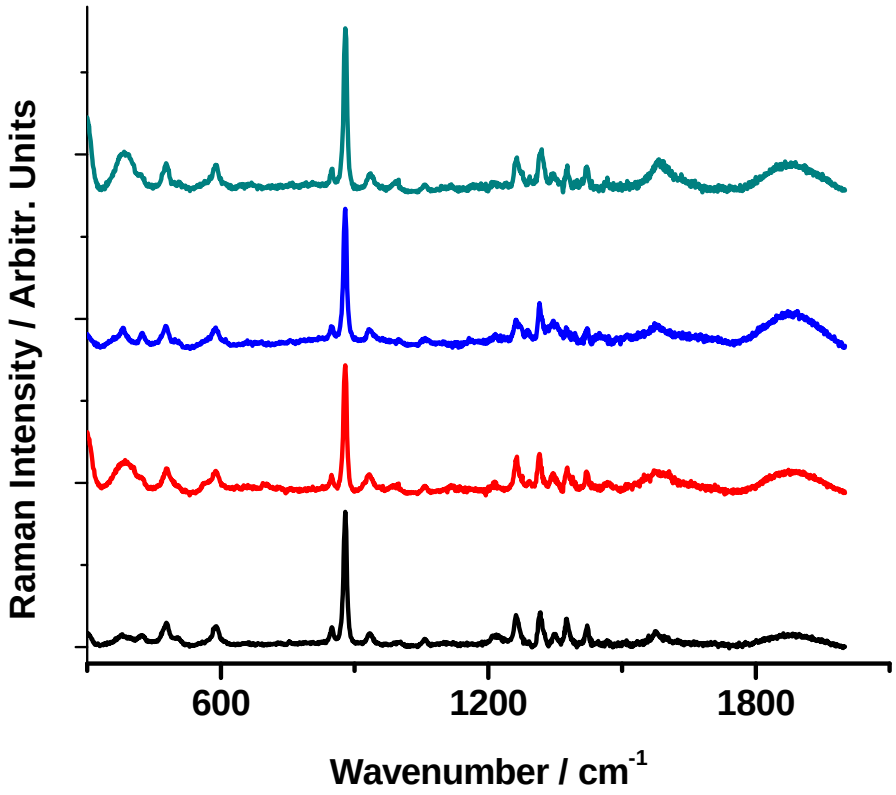

Figure 11. SERS spectra of 5×10^{-5} M RDX using different batches of Au nanoparticles as SERS substrates for reproducibility evaluation.

The reproducibility of SERS measurements of RDX from a given substrate is important especially for trace level detections. We thus evaluated sample to sample variations using different batches of Au nanoparticles at a fixed concentration of 5×10^{-5} M RDX (Figure 11). Results indicate a standard deviation of about 21% for the band area centered at 874 cm^{-1}. This standard deviation is not unexpected for SERS measurements using self-assembled nanoparticles, and our results suggest that the SERS technique may have the potential as a quantitative and qualitative tool for rapid screening of RDX in groundwater.

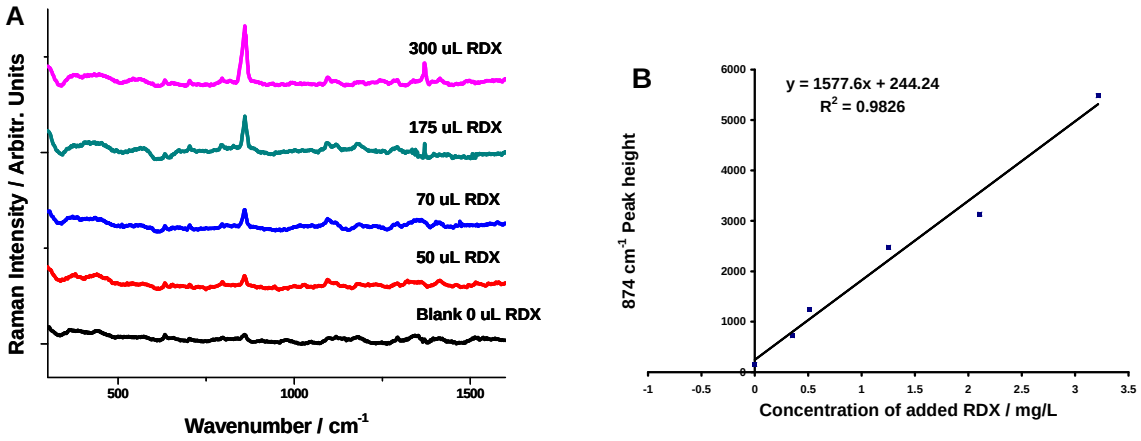

Figure 12. (A) SERS spectra of a contaminated groundwater sample using the standard addition method. (B) Standard addition curve for determining the RDX concentration (0.12 mg/L analyzed by HPLC) in groundwater.

The SERS technique for detecting RDX was further validated using a contaminated groundwater sample obtained from a US Navy site (Figure 12A,B). Rapid detection and screening of explosives in the environment represents a significant challenge because current analytical techniques involve lengthy laboratory preparations and the use of expensive instrumentation (e.g., EPA Method 8330 with SPE). Moreover, groundwater can contain organic impurities which can interfere with the detection and identification of explosives such as RDX, since the EPA method relies on HPLC with analyte detection via retention time only, and is potentially susceptible to false positives. The SERS Raman technique is useful because the vibrational mode of SERS spectrum of a given molecule is

specific and can provide unique fingerprinting for various organic or inorganic molecules. We show that SERS can be used for detection of RDX in environmental samples and could potentially serve as a valuable tool for rapid screening and characterization of energetics in the environment (Figure 12A,B). Using the standard addition technique, SERS analysis revealed that the groundwater from the US Navy site contained 0.15±0.12 mg/L RDX. The concentration determined by SERS compared favorably with that determined by HPLC via EPA Method 8330 (0.12±0.4 mg/L) for the same sample. The standard addition technique was used to correct for matrix interferences because of the presence of unknown constituents in the groundwater. Results showed that the peak intensity at about 874 cm^{-1} increased consistently by spiking the groundwater sample with increasing concentrations of RDX. The error reported in the RDX concentration represents the standard deviation.

Our results are the first to use SERS to detect RDX in a contaminated groundwater at an environmentally relevant concentration. Using the same technique, we also were able to detect TNT at trace concentrations (up to 10^{-9} M by using the desktop micro-Raman system). Figure 13 shows the spectra of TNT at different concentrations. These results again demonstrate the potential of the SERS technology and the need to develop a field portable SERS sensor for environmental detection and analysis. The tool could provide environmental professionals with the ability to rapidly screen samples and/or identify a range of pollutants in the field.

4.2.3 Molecular Simulation of RDX Interactions

Additional literature search, molecular simulation, and experiments were conducted at Navy SPAWAR in an attempt to improve the design of SERS substrates for RDX detection. Previous studies have shown that RDX can effectively be extracted from aqueous samples using fluoroalkylated polysilane films (SAXENA et al., 2005). We therefore selected nitrocyclohexane and 1,3,5-triacryloylhexahydro-1,3,5-triazine (as a simulant of RDX) for the initial study. Thiols with trifluoromethyl groups were purchased, and SERS substrates were prepared. Of these substrates, it was observed that only SERS substrates coated with 2,2,2-trifluoroethanethiol and S-ethyl trifluorothioacetate interacted with simulants. However, the peaks due to the simulants were very weak indicating that the interaction was not particularly strong.

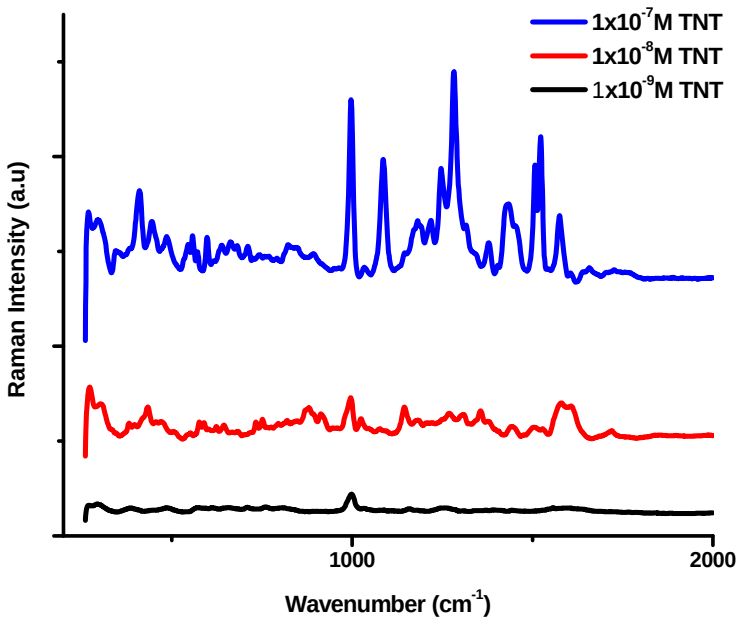

Figure 13. SERS detection of TNT at varying concentrations (from about 0.23 to 23 μg/L) using Au nanoparticles as a SERS substrate.

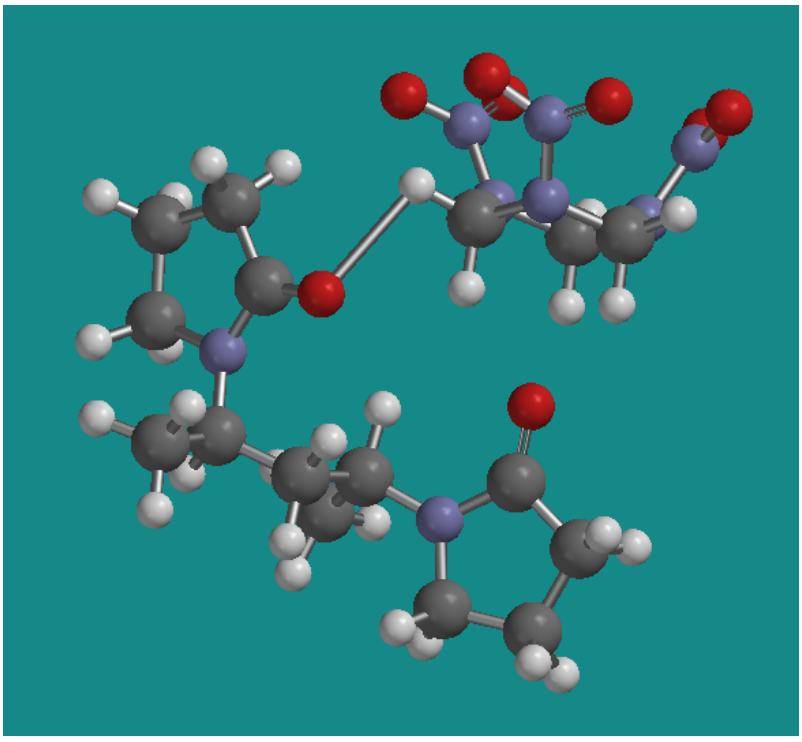

Figure 14. Calculated structure of the RDX complex with pyrrolidone. RDX shows a bowl-like shape (upper right of the figure).

Additional literature searches indicated that polyvinylpyrrolidone strongly adsorbs RDX (FREEMAN et al., 1976). Molecular simulations show that the oxygens of the pyrrolidone moiety interact with the hydrogens of RDX (Figure 14). An attempt was thus made to coat a SERS substrate with polyvinylpyrrolidone (average molecular weight of 1,300,000). However, it was found that the polymer was water soluble and thus unsuitable to be used for SERS measurements.

Molecular simulation also shows that the RDX molecule has a bowl-like shape suggesting that it could potentially interact with cavitand compounds. Modeling of calixarene compounds suggest that RDX can fit inside the cavity of calix[6]arene. Cahill and Bulusu (1993) reported that RDX formed complexes with cyclodextrins, another class of cavitands. Molecular modeling of gamma cyclodextrin (CD), RDX, and the 1:1 complex were thus performed using the semi-empirical (SE) molecular orbital model with AM1 basis sets on supercomputer Spartan 06. While not as accurate as the density function models, the SE model requires less computational time. This is especially significant when modeling molecules as large as gamma-CD. Results show that RDX has the right dimensions to fit inside the cavity of CD. Our calculations also show that, for RDX, the methylene groups present in the ring are positively charged while the nitro groups are negatively charged. Both the methylene and nitro groups of RDX could interact with the exterior ring hydroxyl groups of CD through hydrogen bonding. However, proton NMR spin-lattice relaxation times obtained by Cahill and Bulusu (1993) suggest that the methylene protons of RDX are involved in interactions with CD. Spartan 06 is able to calculate the infrared spectra of the modeled molecules. Results (Figure 15) indicate that there are significant changes in the OH stretching region of CD. There are also changes in the methylene stretching regions of both CD and RDX. In the absence of RDX, the methylene stretching region of CD appears as a broad band between 3100-3000 cm^{-1} consisting of multiple overlapping peaks. Upon complexation with RDX, this band splits into two distinct bands at 3100-3000 and 3000-2970 cm^{-1}. For RDX, the symmetric and asymmetric C-H stretches occur at 2982 and 2910 cm^{-1}, respectively. Upon complexation with CD, these bands shift to 2967 and 2905 cm^{-1}. The modeling also indicates that there are changes in the skeletal region of CD at 500-1500 cm^{-1}.

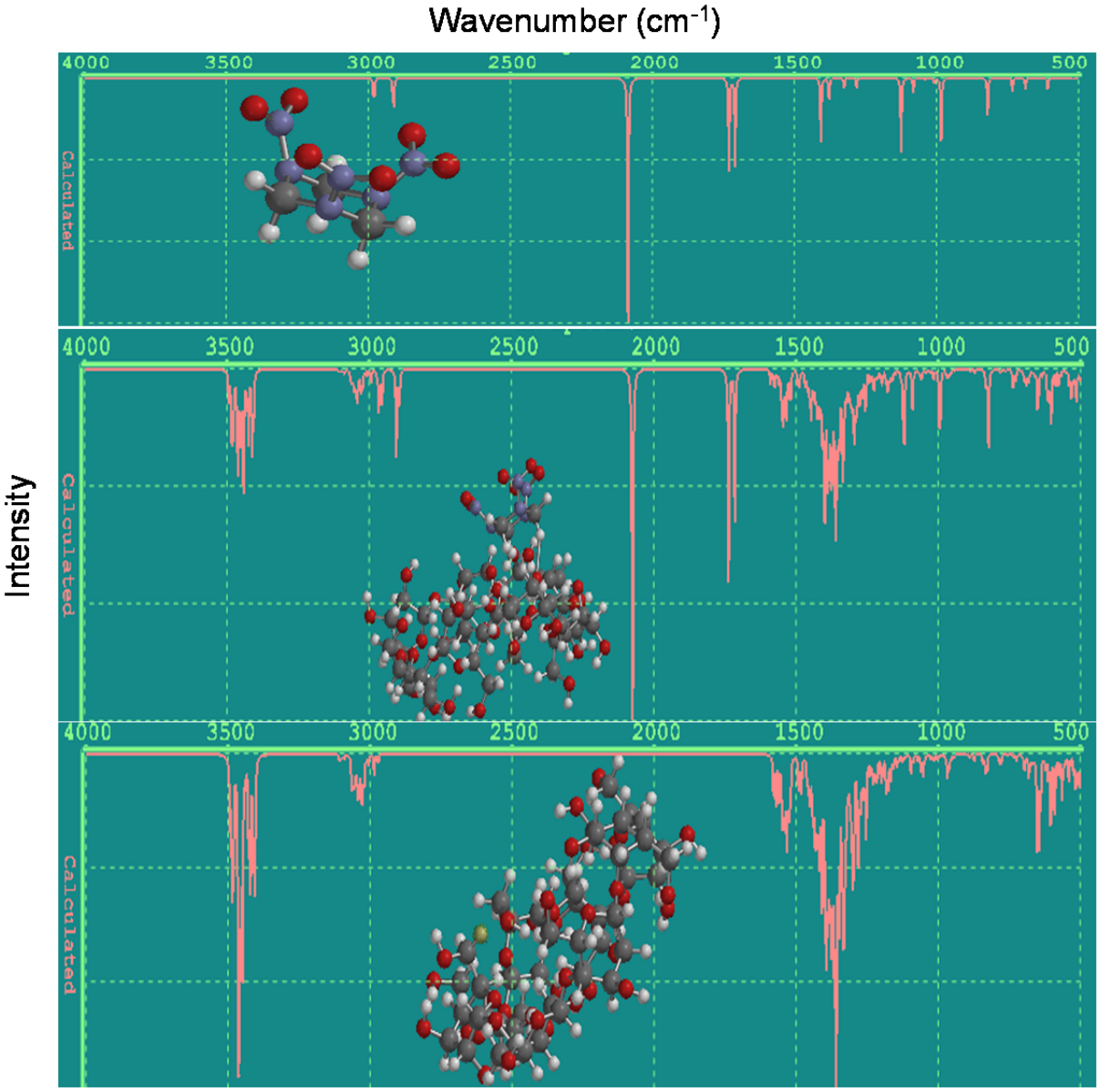

Figure 15. Calculated infrared spectra and molecular structures of RDX, the RDX and γ-cyclodextrin adduct, and γ-cyclodextrin.

4.3 Development and Evaluation of EBL-Fabricated SERS substrates

As stated earlier, one of the major disadvantages of using wet-chemical techniques for SERS preparation is the reproducibility in the synthesis of nanoparticles and the self-assembly of these nanoparticles (to form the SERS substrate). This is also one of the key challenges for SERS to be used as a routine analytical tool. Samples prepared by the wet-chemical techniques usually have relatively high variability such as particle size, size distribution, and gap distance between particles. As such, it is difficult to achieve high reproducibility for materials prepared from different batches or by different laboratories. For practical applications, it is imperative to develop SERS substrates with reproducible and controllable SERS enhancement. Therefore, a major part of this research was focused on the development of novel fabrication techniques to produce reproducible and sensitive SERS substrates using EBL nano-lithography techniques.

4.3.1 Screening and Evaluation of SERS substrates by EBL

During this project, highly ordered SERS substrates were created using electron beam lithography (EBL) and lift-off techniques. These substrates contain a series of two-dimensional models of squares, hexagonal, triangles (bowties), and elliptical nanoparticle arrays. We performed systematic studies of these patterns by varying particle size, spacing, shape, and geometric distributions (partially listed in Table 2) so as to allow determination of SERS responses over large volumetric areas of the substrate (~1600 um^2). For example, the size of nanoparticle array patterns varied between 100 and 350 nm, and the gap distance varied from about 8 nm to >50 nm. Figure 16 shows some selected SEM images of the fabricated nanoparticle arrays as examples. Initially these nanoparticle arrays were fabricated by directly attaching them to the Si wafer, but we later discovered that the SERS enhancement can be further increased by elevating the nanoparticle arrays above the Si wafer (see Figure 17 and details discussed in Section 4.3.2). These SERS-active substrates were prepared with an electron beam evaporator, with the average mass thickness and deposition rate being measured for each film with a Quartz-crystal microbalance (QCM). The substrates were also coated with varying amount of Au at the same deposition rate to evaluate the effect of Au thickness on SERS enhancement For all the other studies, a layer

of 40-nm Au was deposited. Substrates and SERS efficiencies were then evaluated by measuring the relative SERS intensity using either thionine or *p*-mercaptoaniline (*p*MA) as probing molecules. These probing molecules can form a monolayer on Au surfaces and were thus used initially for the determination of SERS enhancement factors.

Table 2. Fabrication of different patterns and dimensions of SERS substrates by EBL nanofabrication techniques.

Pattern	Shape	Size
3_1	Ellipses	150x50 nm
4_4	Circles	200x200 nm
7_1	Ellipses	350x50 nm
7_7	Circles	350x350 nm
50_100	Squares	100x100 nm
50_200	Squares	200x200 nm
50_300	Squares	300x300 nm
H_100	Hexagonals	100x100 nm
H_200	Hexagonals	200x200 nm
H_300	Hexagonals	300x300 nm
T_100	Triangles	100x100 nm
T_200	Triangles	200x200 nm
T_300	Triangles	300x300 nm

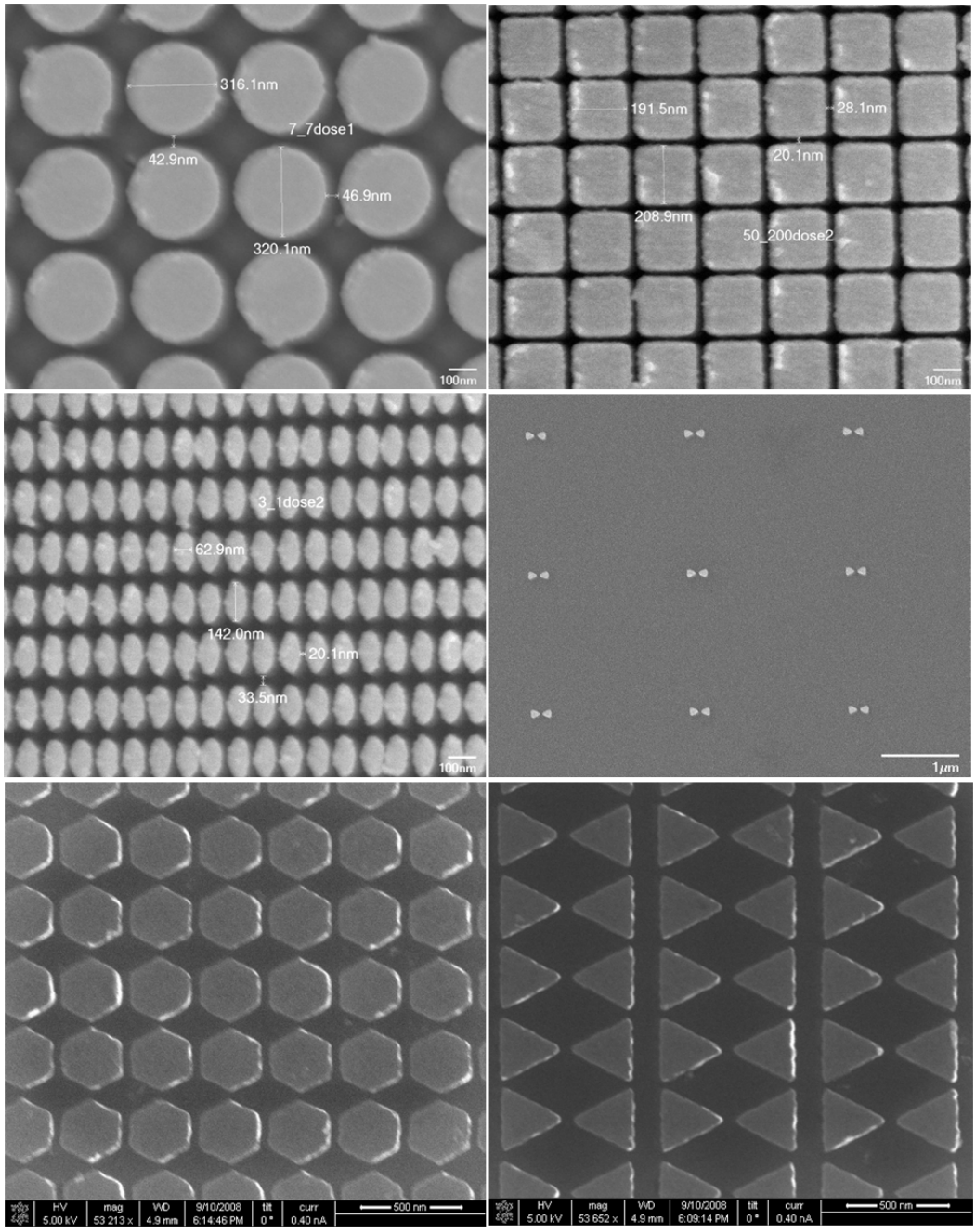

Figure 16. Scanning electron micrographs (SEM) and examples of SERS patterns fabricated by EBL and lift-off techniques after the deposition of 40 nm gold.

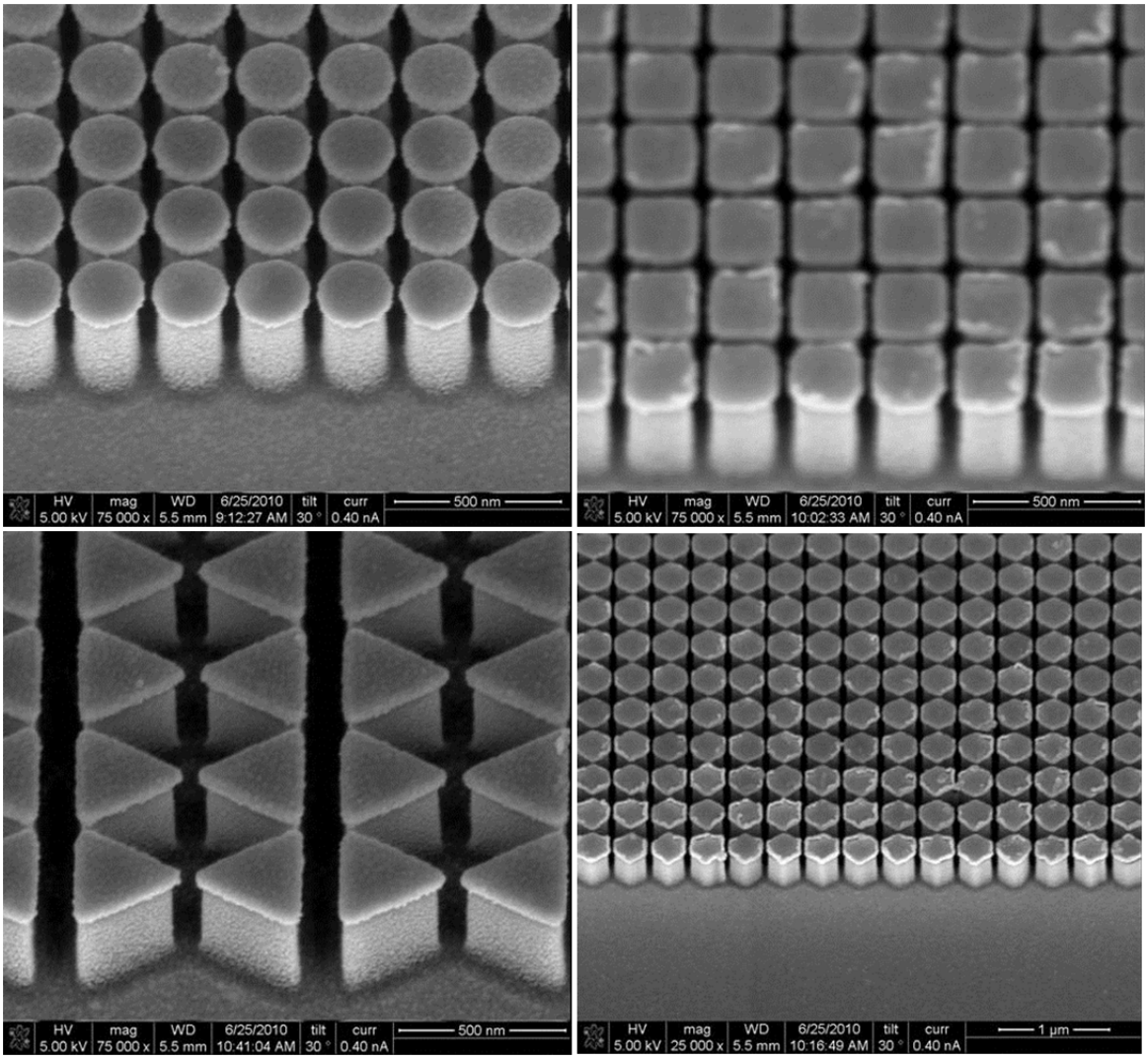

Figure 17. Scanning electron micrographs (SEM) and examples of elevated gold nanoparticle arrays and patterns fabricated by EBL and lift-off techniques.

Figure 18 compares some sample spectra of thionine sorbed onto plane Au surfaces to those of threonine sorbed onto triangular Au bowtie arrays. Results clearly indicate significantly enhanced Raman signal using EBL-fabricated bowtie arrays. We further examined the effect of deposited gold thickness on SERS enhancement. Figure 19 shows the SERS signal of 1×10^{-8} M thionine on triangular bowtie pattern (T-100) coated with Au at different thicknesses. The best enhancement is seen when 40-nm Au is deposited.

Therefore, unless otherwise noted, we subsequently used 40-nm Au deposition for all SERS substrate preparation and evaluation studies. Figure 20 shows examples of systematic studies of SERS enhancement using different nanoparticle geometries or patterns (e.g., ellipses or rods, disks, and bowties) with varying sizes. Results indicate that smaller size nanoparticles (e.g., 100 nm) generally give higher SERS enhancement. However, among all the geometries studied, small triangular bowties were found to give the best SERS enhancement and performance. These EBL fabricated gold bowties were thus selected for subsequent detailed studies of both enhancement mechanisms and field applications for energetics detection (detailed below).

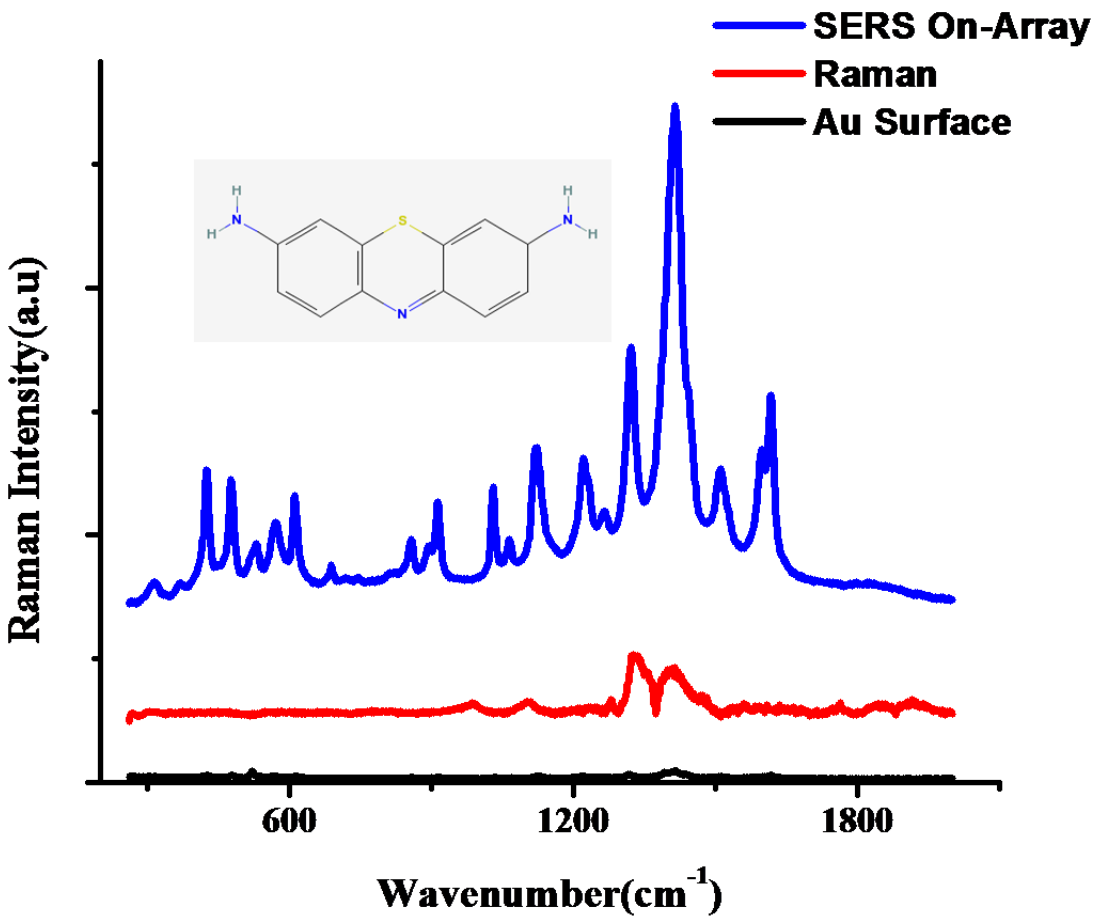

Figure 18. Illustration of nanostructure SERS substrate efficiency, spectra from top to bottom are: nanofabricated SERS substrate (T_1) of thionine (1×10^{-7}M); thionine (1×10^{-7} M) Raman spectrum dry on glass slide; and spectra of 1×10^{-7}M) thionine on flat Au surface.

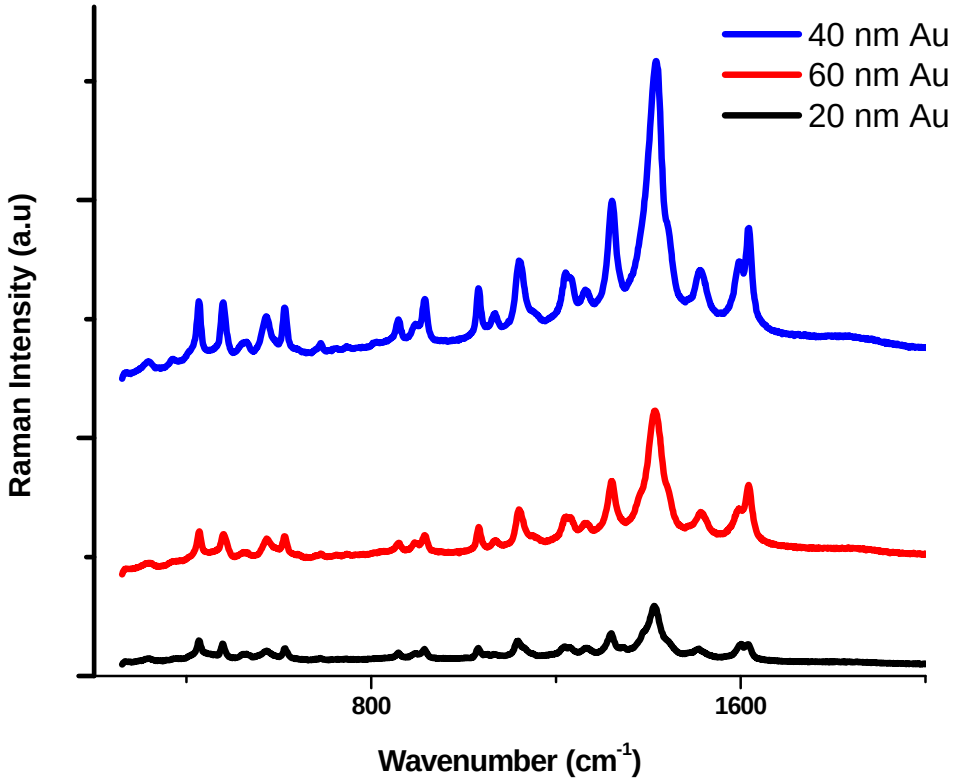

Figure 19. SERS spectra of 1×10^{-8} M thionine collected on patterns T-100 at three different thicknesses of Au deposition.

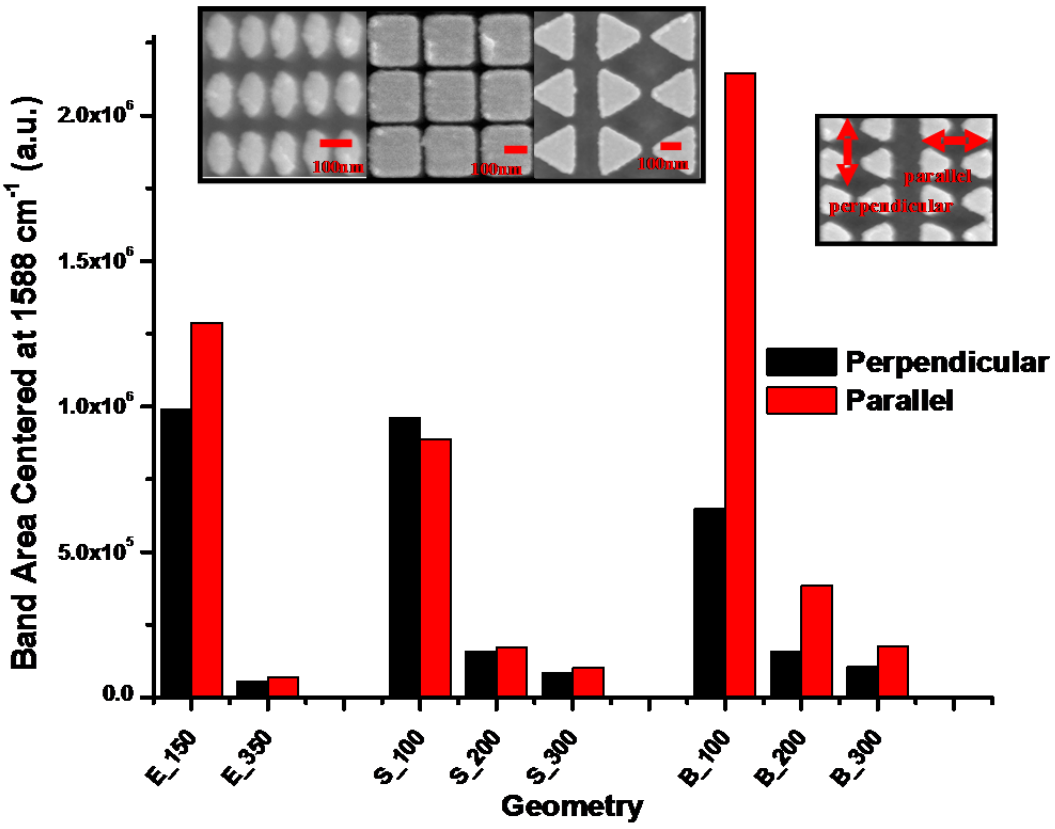

Figure 20. Changes in 1321 cm^{-1} band SERS signal of *p*-mercaptoaniline (*p*MA) (1×10^{-7} M) as a function of geometric pattern and orientation. The direction of laser polarization relative to pattern orientation is shown in the upper right SEM image.

4.3.2 Evaluation of Free-Standing Gold Bowtie Arrays for SERS

Following the initial screening and evaluation of various EBL-fabricated SERS substrates, our work was focused on the use of elevated or free-standing gold bowtie arrays which gave superior SERS performance in preliminary studies. Gold bowtie arrays were fabricated by EBL using a JEOL JBX-9300FS EBL system (JEOL, Japan). First, a 300-nm thick layer of ZEP520A e-beam resist (ZEON Chemical, Japan) was spun on a 10-cm silicon wafer that was subsequently baked at 180 ˚C for 2 min to harden the resist. The resist was then patterned at an acceleration voltage of 100 kV and exposed to a dose of 450 $\mu C/cm^2$. After exposure, the resist was developed in xylene for 30 s, rinsed in isopropyl alcohol for another 30 s and then dried under a stream of nitrogen. Following the development, the sample was exposed to oxygen plasma for 6 s at 100 W (Technics Reactive Ion Etching System) to remove residual resists on the arrays. For the lift-off process, an 8-nm Cr layer was first deposited using an electron-beam dual gun evaporation chamber (VE-240, Thermonics Laboratory, Port Townshend, WA) equipped with a quartz crystal monitor to measure the thickness; the excess resist and Cr were removed via lift-off using an acetone bath followed by an isopropyl alcohol rinse. Note that a Cr-layer is used as an adhesion layer for Au or Ag; without a Cr-adhesion layer, Au does not stick to silicon so it is easily removed by subsequent cleaning and rinsing. Following the lift-off process, the wafer was dried under a stream of nitrogen. An Oxford Reactive Ion Etching (RIE) instrument (Oxfordshire, UK) was subsequently used at a rate of 100 nm/min for 1.5 minutes to create the silicon post with the Cr metal pattern on the top and to generate elevated bowtie arrays.

A 40-nm thick gold film was subsequently deposited using the same evaporation chamber to generate the SERS active substrate. All bowtie arrays were made with pairs of triangular prisms (with varying sizes from 100 to 500 nm) with a tip-to-tip gap distance of about 8 to 50 nm and a center-to-center distance ranging from 300 nm to 2 μm. The array size was typically 1×1 mm, and each wafer (10-cm diameter) contained 24 identical arrays for sample analysis. These bowtie arrays were then used for sensitivity, reproducibility, and gap-dependent SERS studies and the analysis of samples. Bowtie arrays with different spacing were produced by varying the center-to-center distance (ccd) or row-to-row distance (rrd). They include an isolated bowtie array with ccd = rrd = 2 μm, a high-density

array with ccd = rrd = 300 nm, and a low density array that matches the incident laser wavelength with rrd = 2 μm and ccd = 785 nm.

Our studies serve to provide new mechanistic understanding of SERS enhancement resulting from elevated gold bowtie arrays, which were subsequently used for the detection of energetics both in the laboratory and in the field. Moreover, we demonstrated large SERS enhancement factors (exceeding 10^{11}) resulting from a new configuration of elevated gold bowtie nanoanatenna arrays with optimized array periodicity. Figure 21a provides a schematic illustration of these structures, together with a SEM image of the actual structures in Figure 21b, and the spatial distribution of the *E* field intensity calculated by finite difference time domain (FDTD) simulations in Figure 21c. As stated earlier, a process combining nanofabrication steps of pattern definition by EBL, metal deposition, liftoff, and reactive ion etching arranged in a particular sequence enabled the fabrication of the elevated gold bowtie arrays on Si wafers. A precisely controlled deposition of 40 nm gold on a Cr adhesion layer located on top of 200-nm tall Si posts was used to close the 20-nm gap size defined by EBL to 8±1 nm. This step also produces the characteristic overhang that along with the post defines the three-dimensional bowtie nanoantenna (Figure 21b) and distinguishes these structures from gold bowties that remain attached to the substrate (FROMM et al., 2006; FROMM et al., 2004; KIM et al., 2008; KINKHABWALA et al., 2009). The contrast in SEM backscattered electron images shows that only the bowties and not the posts are coated with gold (Figure 22) (HATAB et al., 2010b). A comparison of SERS spectra of elevated bowties with that of bowties attached to the substrate is provided in Figure 21d. The elevated bowties allow manifestation of intrinsic plasmonic coupling effects in suspended nanocavities, or the tip-to-tip nanogaps, from structures that are not in physical contact with a substrate. This configuration results in up to 2 orders of magnitude additional enhancement in SERS response compared to that of non-elevated bowtie arrays (Figure 21d). The influence of the post heights on the SERS response is confirmed by and qualitatively agrees with FDTD simulation results (described below).

Different density arrays shown in Figure 23a were fabricated by changing the center-to-center distance (ccd) in rows along the bowtie axis, and the row-to-row distance (rrd). The isolated bowtie arrays shown in image II of Figure 23a have a dimension of ccd = rrd = 2 μm that is close to the laser spot size, which ensures that the SERS measurements

represent local response from a single bowtie. We next compared the SERS response of isolated bowties with that from *high-density* (III) and *low-density* (I) arrays in Figure 23a with specific periodicity of ccd = rrd = 300 nm, and ccd = 785 nm, rrd = 2 μm, respectively. The Raman EF for these arrays, as shown in Figure 23b, was determined first from the SERS intensity of a probing molecule, *p*-mercaptoaniline (*p*MA) (HAYNES and VAN DUYNE, 2003; JACKSON and HALAS, 2004). Exposure of the bowties to a *p*MA solution (10^{-5} M) results in the chemisorption and uniform coating of the gold surface by a monolayer of *p*MA molecules that ensures unambiguous determination of the SERS enhancement and good reproducibility. The EF was determined following a procedure established in the literature (see Section 3.5) (FROMM et al., 2004; HAYNES and VAN DUYNE, 2003; HU et al., 2007; JACKSON and HALAS, 2004; WELLS et al., 2009). Here the EF represents the ratio of the SERS signal to the non-enhanced bulk Raman signal measured and normalized per molecule for the 1588 cm^{-1} Raman band.

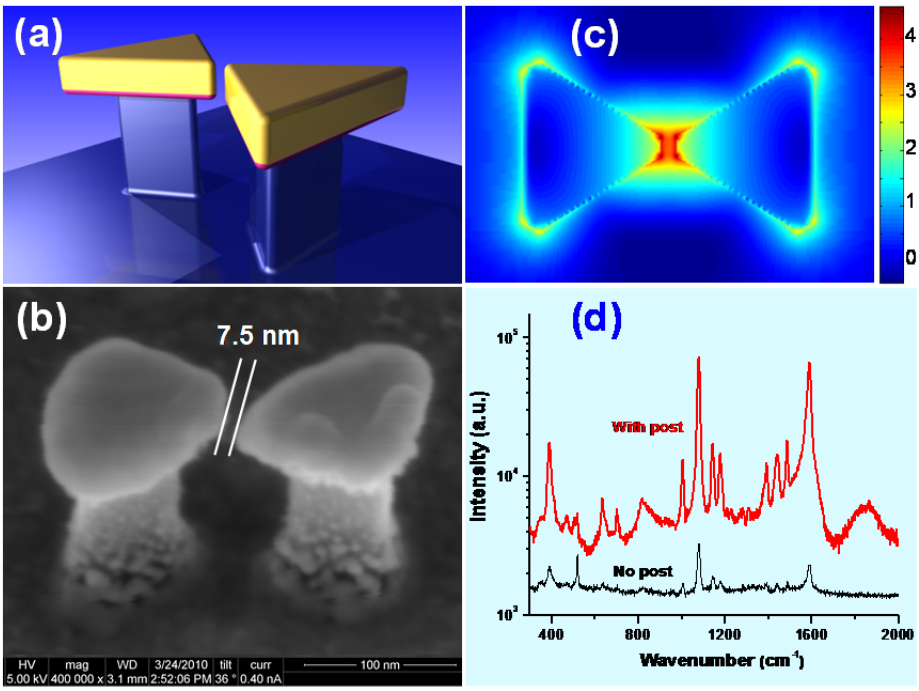

Figure 21. (a) Schematic illustration of elevated gold bowties on top of Si posts etched into a Si wafer with a magenta colored Cr adhesion layer between the gold layer and the Si post. (b) Side view SEM image of a three-dimensional gold bowtie nanoantenna with a gap of 8±1 nm. (c) The spatial distribution of the *E* field intensity calculated by FDTD simulations. The intensity is given by a logarithmic scale color bar. (d) Comparison of SERS spectra of *p*-mercaptoaniline from elevated and non-elevated bowtie array substrates.

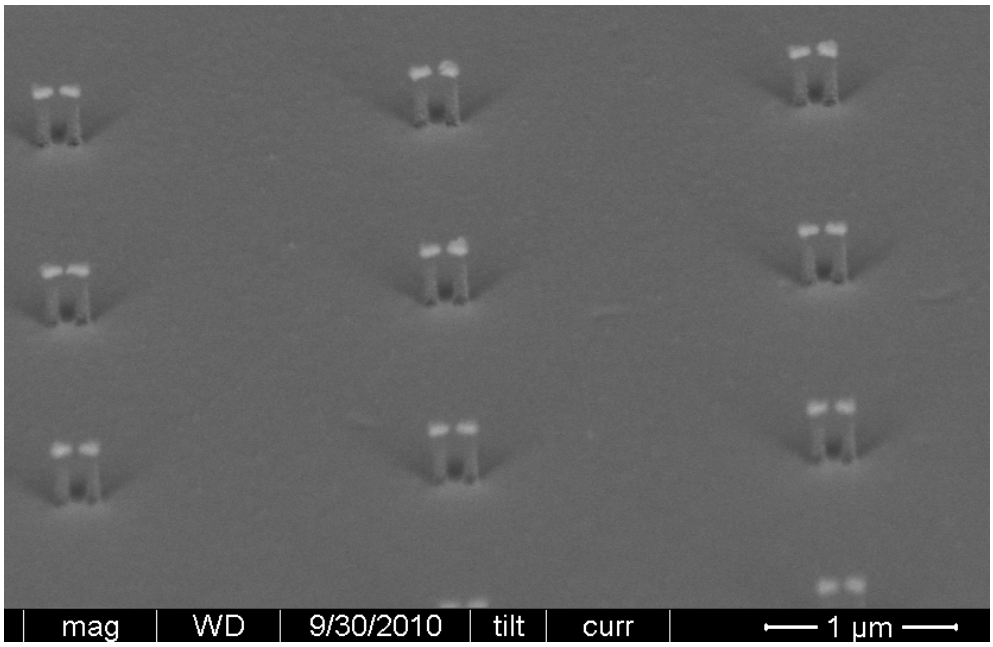

Figure 22. SEM image of bowtie arrays using a backscattered electron detector. The technique is used to distinguish heavy element gold (white triangles) from light element Si (gray posts).

For all bowtie arrays, the EF increases with decreasing gap size and reaches 2×10^{11} and 7×10^{11} at the smallest gap of 8±1 nm for the isolated and low-density bowtie arrays (Figure 23b). These values match the largest enhancements reported for nanoshells and nanoparticle aggregates that typically contain a number of randomly distributed hot spots (HAYNES and VAN DUYNE, 2003; JACKSON and HALAS, 2004; KNEIPP et al., 1997; NIE and EMORY, 1997). In addition to the distinct gap size dependence that dominates the response of isolated bowties, we also observed that the bowtie arrays are subject to collective interactions that either degrade or further enhance the overall SERS response. The trends in Figure 23b identify the array periodicity as the critical factor that determines the EF change. The maximal enhancement is achieved when the periodicity of the arrays matches the laser wavelength. In particular, we note that the EF from the high-density bowtie array with *ccd* = *rrd* = 300 nm (III in Figure 23) was about one order of magnitude lower than that for the isolated bowties. In contrast, the low-density arrays with optimized periodicity of *ccd* = 785 nm (I in Figure 23) that matches the Raman laser wavelength, produced an EF with nearly an order of magnitude additional increase above that for isolated bowties.

These observations represent the first definitive experimental confirmation of the theoretically predicted long-range collective photonic effect (HAYNES et al., 2003; ZHAO et al., 2006; ZOU and SCHATZ, 2005). This important finding suggests that even greater enhancements might have been realized in previous experiments (FANG et al., 2008; KIM et al., 2008) had the bowtie or nanoparticle arrays been more sparsely distributed.

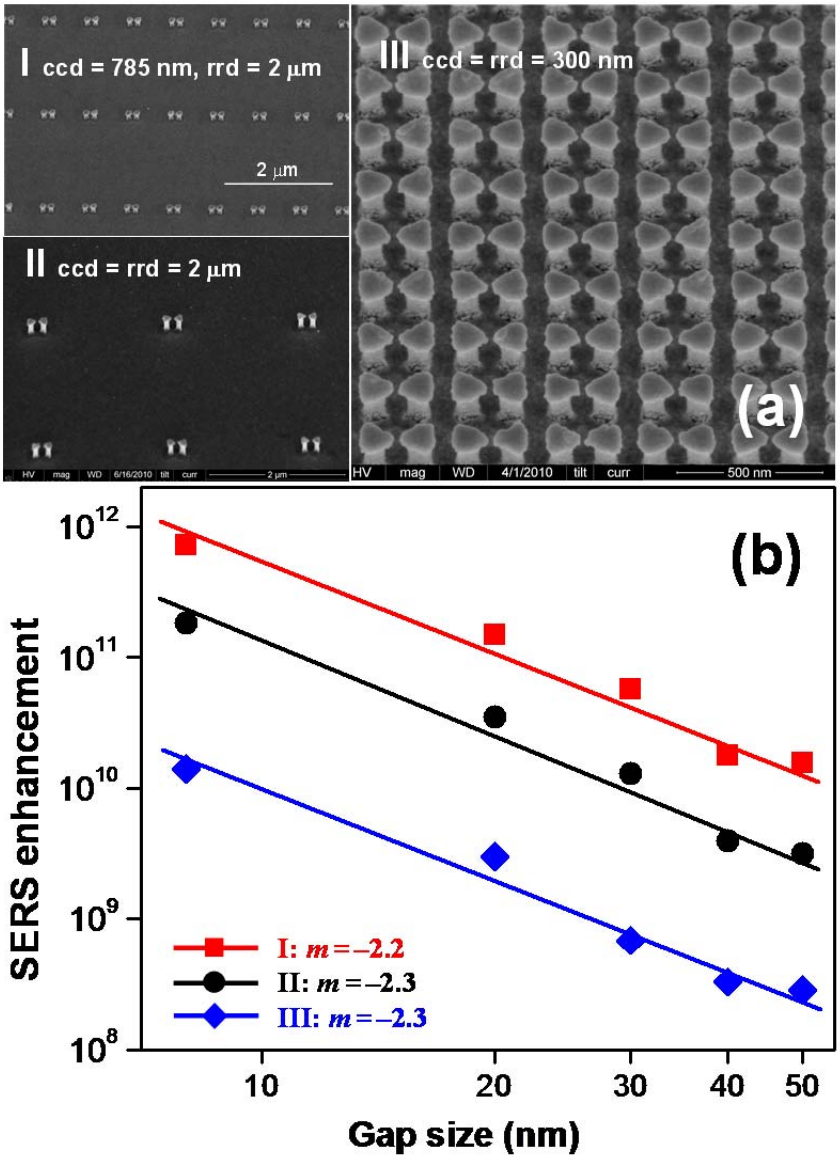

Figure 23. Determination of the gap size dependence and the long-range collective plasmonic effects in SERS enhancement using elevated gold bowtie nanoantenna arrays. (a) SEM images of the elevated gold bowtie arrays with varying center-to-center distance (ccd) in rows along the bowtie axis, and row-to-row distance (rrd). (b) A log-log plot of SERS enhancement factors (*EF*) as a function of bowtie nanogap size in arrays I, II, and III with different bowtie spacing. The slope (*m*) is determined by fitting the power-law relationship of $EF \propto Ad^m$ to the experimental data.

The spatial distribution plot of the *E* field intensity in Figure 21c shows that for elevated bowties the nanogap effect is strongly localized in the volume between the tips of the triangles. The simulation results of the maximum electric field enhancement $|E|^4$ as a function of the post height are shown in Figure 24. The plot of $|E|^4$ normalized by that for bowties directly attached on Si substrate (no posts) shows periodic crests (at ~100, ~400, and ~700 nm) and valleys (at ~300 and ~600 nm) with a period of ~300 nm. This behavior is similar to the resonance in a cavity, which has the standing wave resonance for every half wavelength along the cavity length. Based on the periodicity of ~300 nm, the guiding wavelength in the cavity should be ~600 nm. However, it should be noted that unless it is an idealized cavity, this guiding wavelength is not necessarily the same as the incident wavelength.

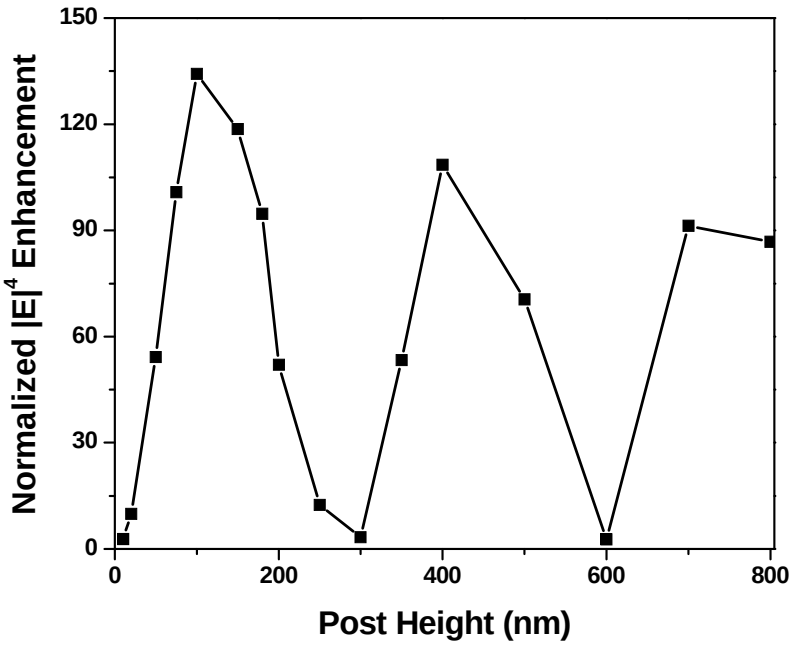

Figure 24. The calculated maximum field enhancement $|E|^4$ normalized by that without the Si post as a function of the post height showing the characteristics of nanocavity resonance.

The FDTD simulations also identify the shape and sharpness (*w*) of the triangle's apex (Figure 25) as factors that affect efficient coupling of the incident optical radiation into the bowtie gap. FDTD simulations of the maximum $|E|^4$ enhancement as a function of

the gap size, d, are also performed at varying apex widths for ccd = rrd = 300 nm (Figure 25). For d > 50 nm, the FDTD results show that the $|E|^4$ enhancement is insensitive to the gap size because the two triangular prisms are sufficiently far apart to eliminate near-field coupling. However, for d < 50 nm, the maximum $|E|^4$ enhancement versus d can be fitted by a power law: $|E|^4 = Ad^m$, where A and m are fitting parameters with A the intercept of the line and m the slope in the log-log plot. It is of interest to explore the meaning of the power-law dependence. The E field intensity in a plasmonic nanocavity is a function of the cavity geometry and quality factor. A general equation to describe this field intensity for all plasmonic cavity structures is unattainable, and a semiquantitative approach is thus used in the present study to describe the bowtie nanocavity effect. For a bowtie nanocavity, the field intensity is inversely proportional to the effective volume. For a small gap size, the field is highly confined in the gap region and the radiation loss is neglected for simplicity in analyses because the field is highly confined at the resonant frequency. While the effective volume of the bowtie cavity is proportional to the product of the apex width, w, the gap size, d, and the height of the bowtie, the E field intensity is approximately inversely proportional to the product of w and d when the height is fixed. Hence, for a fixed bowtie height, the $|E|^4$ enhancement is proportional to $(wd)^{-2}$. Figure 26 shows the maximum $|E|^4$ enhancement versus wd on a log-log plot. These results show that the slope falls within a narrow range at about –2.5 that qualitatively agrees with the predicted value of –2 and also the experimentally determined value of about –2.2 (Figure 24).

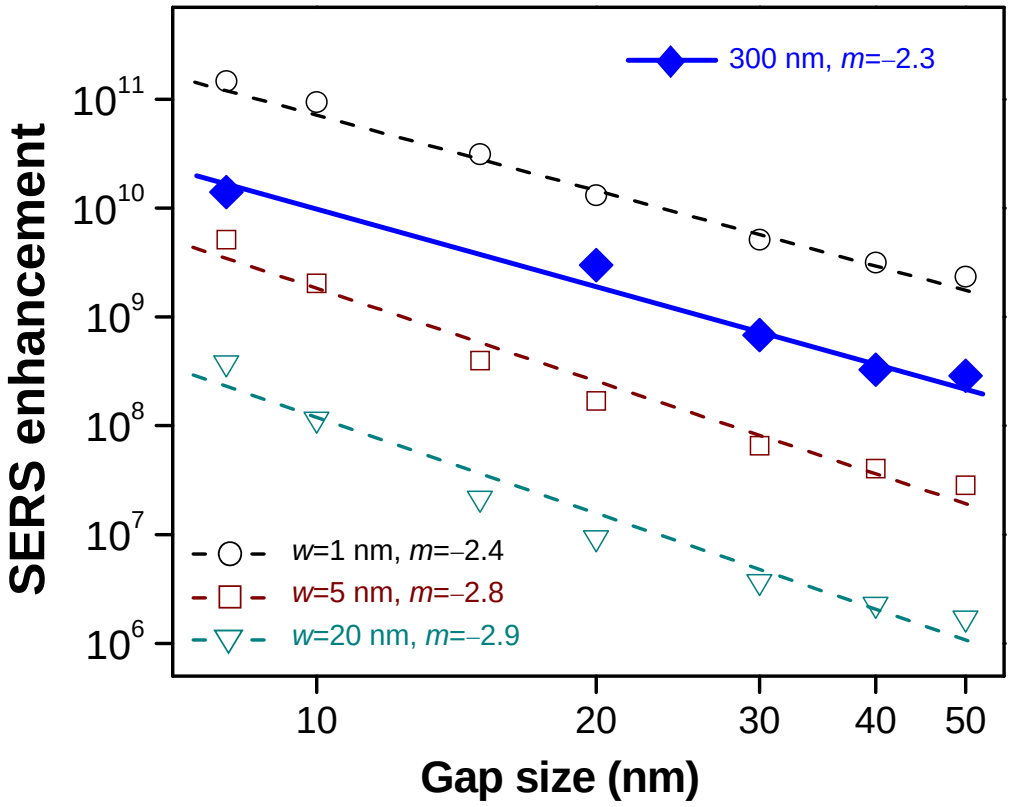

Figure 25. Comparison of the FDTD calculated maximum field $|E|^4$ enhancement (dashed lines with open symbols) for apex widths w = 1, 5, and 20 nm with the experimentally determined SERS enhancement (solid line with solid diamonds) as a function of nanogap size for elevated bowtie arrays with ccd = rrd = 300 nm (III in Figure 21). The slope (m) is determined by fitting the power-law relationship of EF $\propto |E|^4 = Ad^m$ to the data.

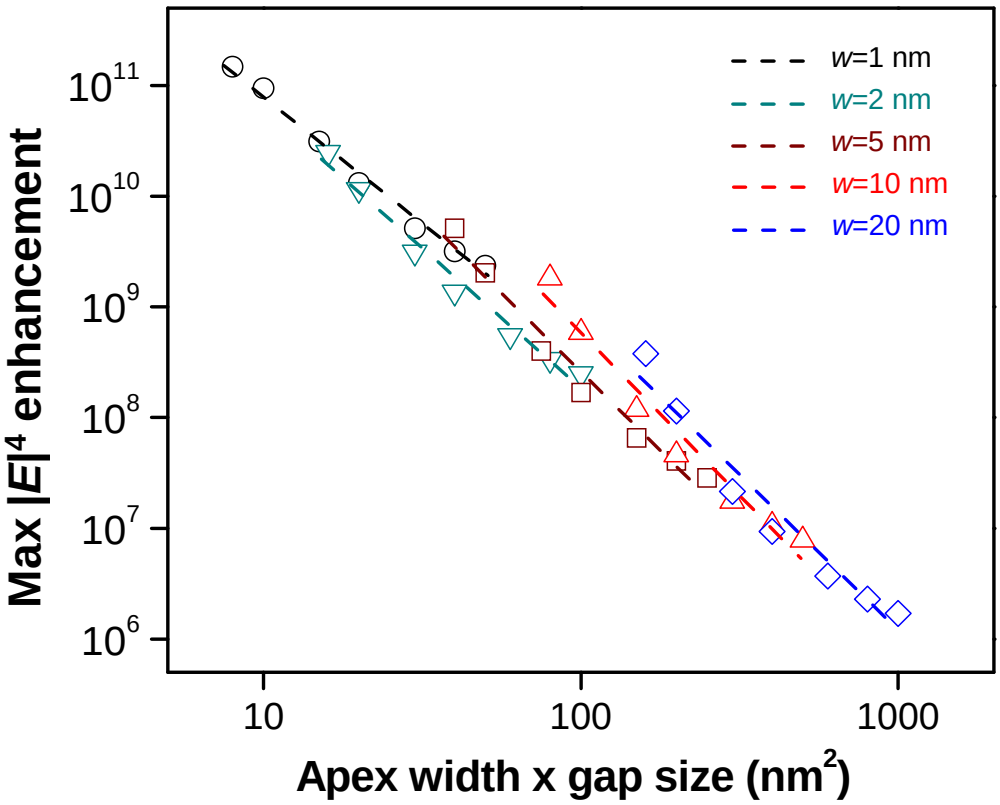

Figure 26. The maximum field enhancement $|E|^4$ calculated by FDTD as a function of the product of the apex width and the gap size, wd, for varying apex widths. The open symbols are FDTD data and the lines are the power-law fit. The inter-bowtie distances are ccd = rrd = 300 nm. The diameter of the Si posts is 40 nm, and the height is 200 nm. The calculated slope falls in a narrow range of about –2.5.

Figure 26 illustrates that the nanogap effect and the resulting SERS response become stronger with the apex sharpness (w) increasing from 20 to 1 nm. The elevated gold bowtie arrays reveal another important feature of the EF. A log-log plot of the EF against the gap size, d, gives a straight line with a slope (m) near –2.2±0.1 for the bowtie arrays (Figure 23b). Similar magnitude and slope are obtained using FDTD simulations for the high-density bowtie arrays with apex width near 1 nm (Figure 25). Based on the general relationship of the EF $\propto |E|^4 = Ad^m$, this behavior is equivalent to a weak power law dependence of E on the gap size given by $E \sim d^{-0.56}$, that is even weaker than the decay of a monopole field according to Coulomb's law of $E \sim d^{-2}$. These findings suggest that

narrowing the gap separation between the two prisms below ~50 nm the bowties enter into a regime characterized by exceptionally strong *E* field within the gap region. In this strongly coupled regime the *E* field shows little attenuation possibly due to resonant nanocavity effects (DONG et al., 2010) supported by both experimental observations and the FDTD simulation (Figure 26). However, the weak power law dependence may also include a component resulting from red shifting of the plasmon resonant frequency with decreasing gap size (SUNDARAMURTHY et al., 2005; ZHAO et al., 2006; ZHAO et al., 2003). According to the plasmon ruler equation (JAIN et al., 2007; ZULOAGA et al., 2009) the plasmon wavelength shift reaches maximum for very small gap sizes and decays exponentially with the gap size. Nevertheless, an important technological significance of this weak attenuation comes with the realization that in the strong coupling regime the arrays can tolerate a certain degree of gap size non-uniformity and geometrical imperfection without losing their ability for large field enhancement. The spatial localization of a free-standing, finite plasmonic volume enabled by the three-dimensional elevated bowtie nanoantenna substantially expands the versatility of utilizing *E* field enhancement that has numerous applications in chemistry and physics including single molecule spectroscopy, chemical and biological detection (used in this study), and a variety of advanced optical characterization using periodic metallic nanostructures.

4.4 Development and Construction of a Field Portable Raman Sensor

The ultimate goal of this project was to field apply the SERS technology for rapid screening and analysis of energetics in contaminated groundwater and surface water. This required the coupling of nano-fabricated SERS substrates with a portable Raman analyzer. During the course of this project, we developed and constructed a portable Raman/SERS sensor which was interfaced with a fiberoptic SERS probe. Figure 27 illustrates the design of the SERS probe with all optical lens necessary for the laser excitation and signal collection, the constructed fiberoptic sensor, and the portable Raman spectrometer. A key component of the optical probe is an adjustable SERS interface, where the SERS substrate is attached. The focal point of the SERS substrate can be adjusted, allowing for field optimization of the SERS signal to noise ratio. As stated earlier, the initial configuration of

the portable Raman sensor included a EZRaman-M system equipped with a fiber optic probe (see Figure 5a).

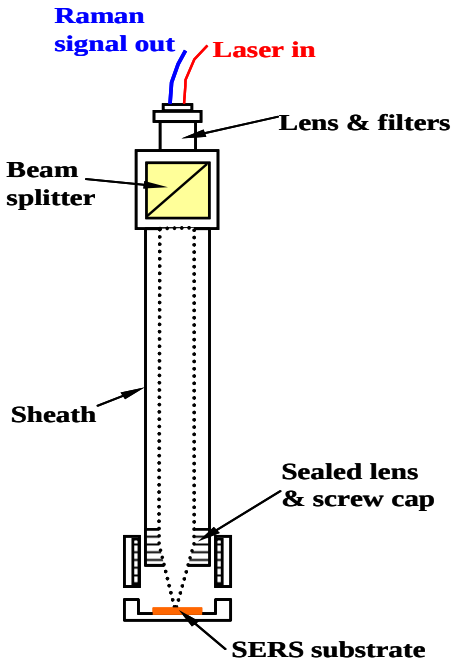

Figure 27. Design of the surface enhanced Raman scattering (SERS) probe and a constructed portable Raman spectrometer interfaced with a fiberoptic SERS probe.

Initially, the portable Raman system was tested using thionine and perchlorate as probing molecules (Figure 28). The initial data showed that thionine could be detected at ~ 10^{-6} M and perchlorate at ~ 10^{-3} M using the portable instrument. These concentrations were significantly higher than those for the laboratory Raman spectrometer, largely due to signal loss and misalignment through the optical fibers. This is primarily because SERS is very sensitive to the focal point where the laser beam interacts with the substrate to generate electromagnetic enhancement. Despite the fact that each SERS substrate contains thousands of nano-patterned bowtie arrays, the EBL-fabricated substrate is limited to be ~1 mm^2 in size. Therefore any mis-alignment between the laser beam and the substrate could result in low or no Raman signal.

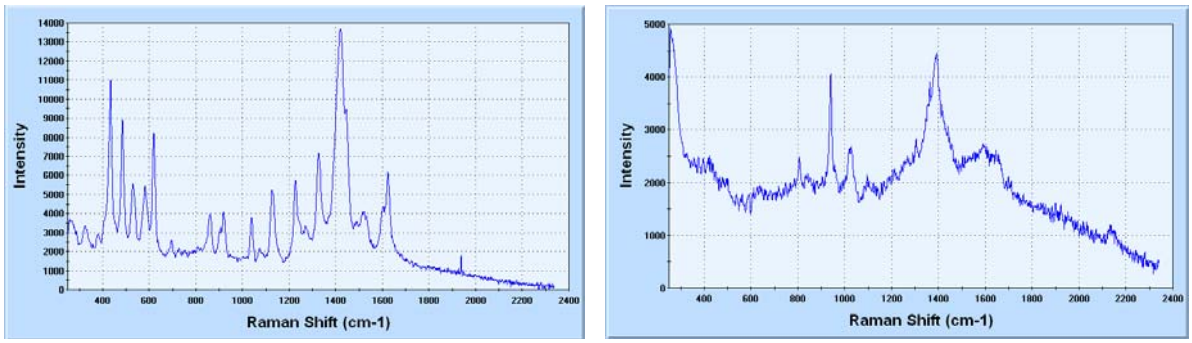

Figure 28. Initial testing results using a constructed portable Raman sensor interfaced with a fiberoptic SERS probe. The probing molecules are thionine (10^{-6} M) (left panel) and perchlorate (10^{-3} M) (right panel).

We subsequently modified the design of the portable Raman system to improve its sensitivity for laboratory and field detection of energetics. Major improvements included (1) acquiring and integrating an EZRaman-I system equipped with a cooled charge-coupled device (CCD) detector (up to -50°C) for improved detection sensitivity; (2) shortening the optic fiber (for decreased signal loss) and encasing it in a stainless steel case (for increased stability and rigidity), and (3) utilizing a mini- XYZ stage that is used to adjust the focusing of the SERS probe to sample analyte. Furthermore the entire sensor system was fitted in a 6×12×18-inch casing for improved portability and durability (Figure 5b). These modifications were successful in improving the instrument sensitivity (primarily by allowing better laser alignment) and, at the same time, permit rapid screening of field samples without the need for lengthy sample preparation and transportation.

For example, Figure 29 shows the SERS spectra of thionine at different concentrations using the portable Raman sensor. The intensity of the signal increased significantly with the improved system setup. To confirm these observations, another study was performed using *p*-ATP as the probing molecule. Figure 30 shows the SERS spectra of *p*-ATP at different concentrations. Again, we observe that the intensity of the signal was greatly enhanced, and the detection limit was ~ 10^{-7} M, compared to 10^{-9} M for the laboratory desktop instrument.

More importantly, we show greatly improved detection of ClO_4^- at different concentrations as low as ~ 5×10^{-8} M (or 5 μg/L). Typical SERS spectra of ClO_4^- at different concentrations (from 10^{-3} to 10^{-6} M) were shown in Figure 31 using bare Au arrays. With additional surface modifications of the SERS substrate, we recently observed the detection of ClO_4^- at concentrations as low as ~ 5×10^{-8} M. These results illustrate significant improvements compared with previously measured detection limits of ~ 10^{-3} M (before modifications). Perchlorate concentrations of 10^{-7}–10^{-8} M can be readily detected after system improvements and optimization of SERS substrates.

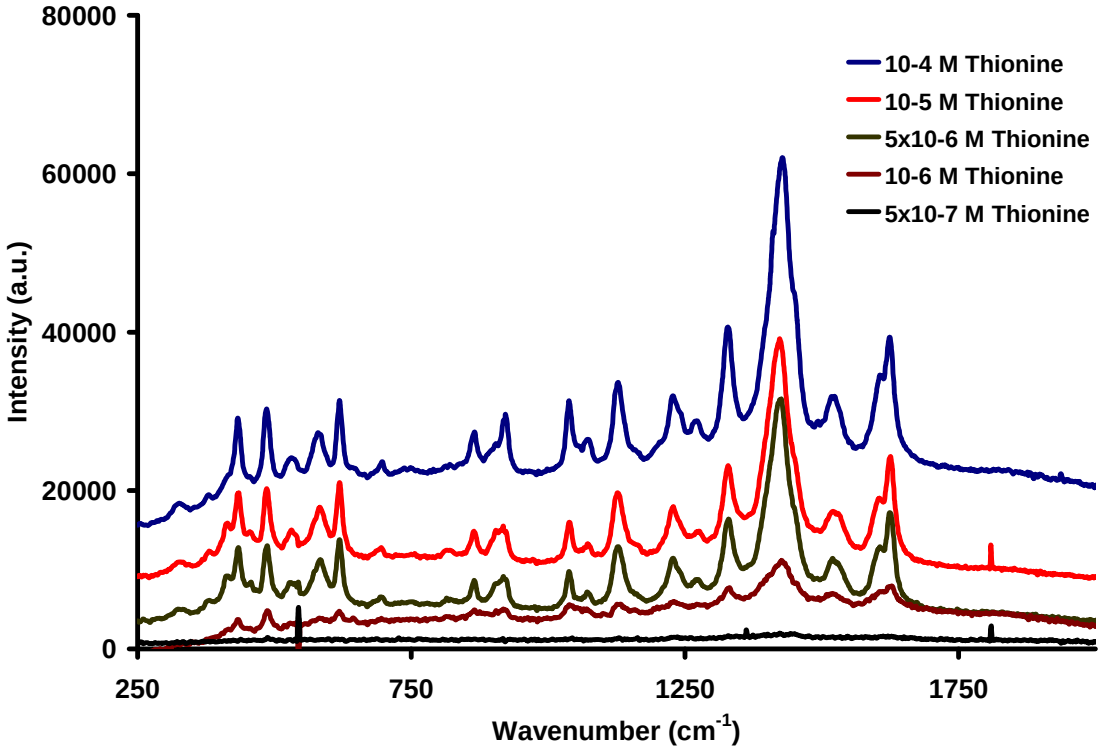

Figure 29. SERS detection of thionine at different concentrations collected with the portable Raman sensor.

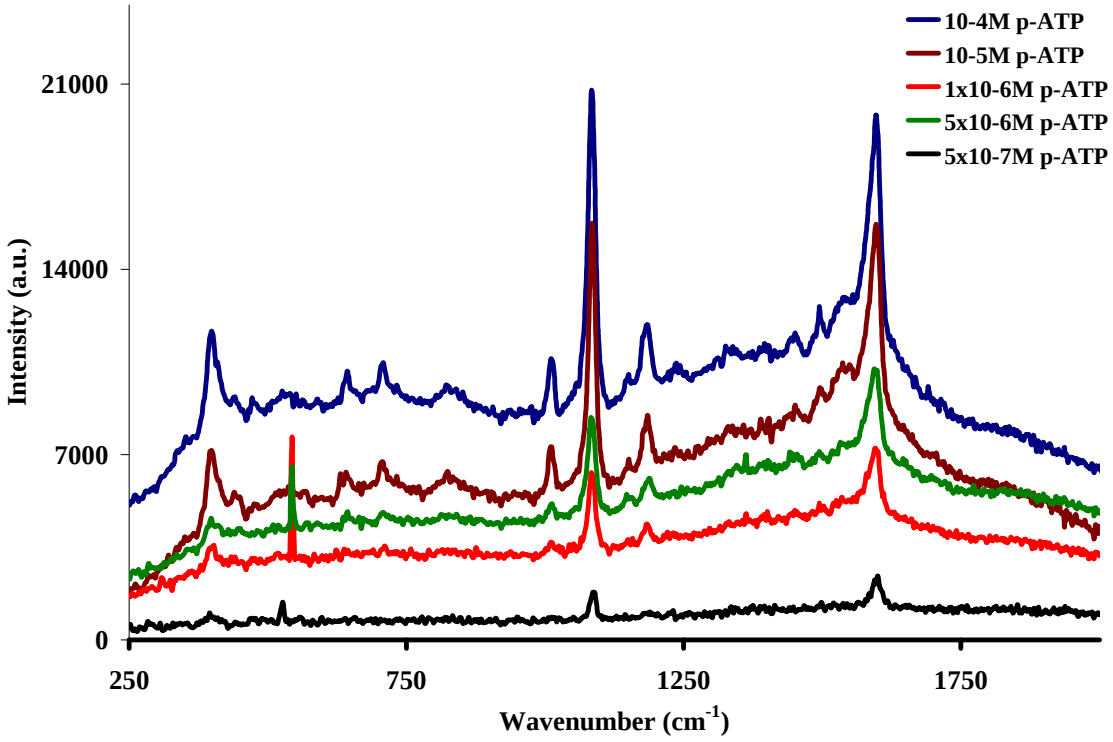

Figure 30. SERS detection of *p*-aminothiophenol (*p*-ATP) at different concentrations collected with the portable Raman sensor.

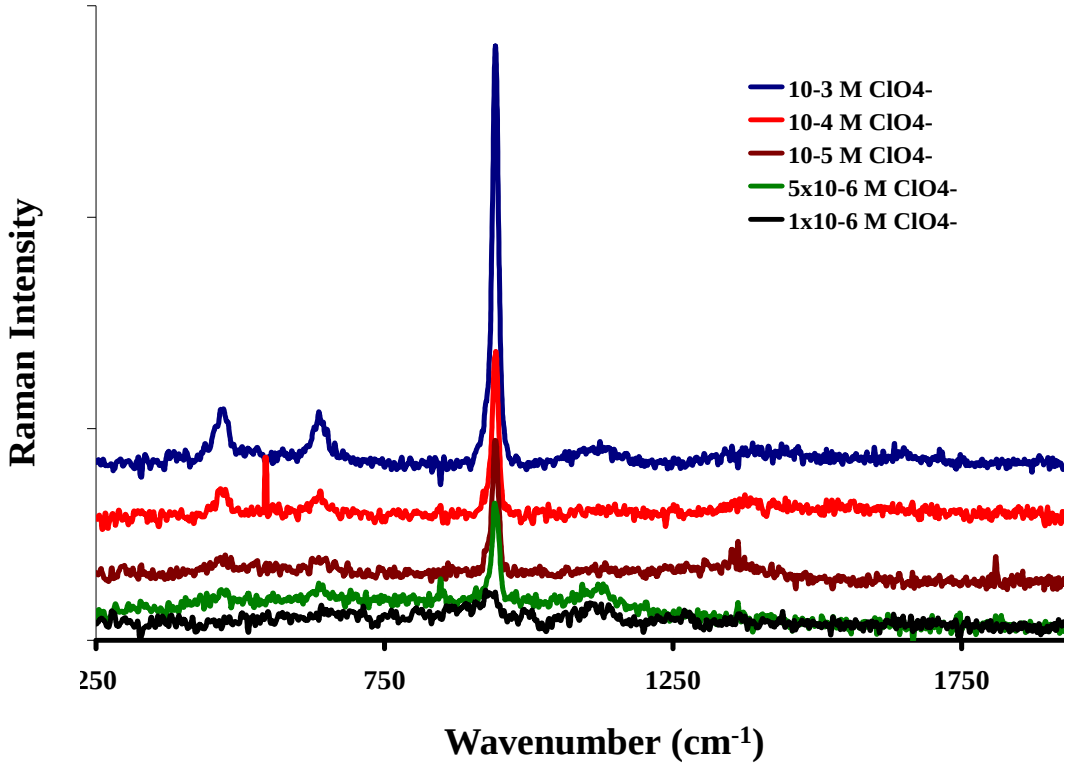

Figure 31. Portable SERS-Raman sensor detection of perchlorate (ClO_4^-) at concentrations as low as ~ 10^{-6} M using unmodified Au array substrates.

4.5 Performance Evaluation of a Field Portable Raman Sensor

4.5.1 Materials and Methods: Portable Raman Sensor

SERS Substrates Preparation: Elevated gold bowtie nanostructural arrays were fabricated by EBL and used for the evaluation of the constructed portable Raman sensor for energetics detection, as described previously in Section 4.3.2.

Similarly to the initial evaluation using a desktop Raman spectrometer, we used the self-assembled monolayer of *p*MA was prepared by exposing the Au bowtie arrays to an aliquot of freshly prepared aqueous solution of *p*MA at 10^{-5} M (1.5 mL) in a plastic petri-dish for 12 hours at room temperature. Samples were then rinsed in a solution containing 10% ethanol and 90% deionized water (18.2 MΩ) to remove unbound *p*MA and dried with

a flow of N_2. The maximum SERS signal was obtained by focusing the laser beam on the substrate, and the spectral data (N = 8–13) were collected by moving the stage at ~10 µm intervals (one spectral acquisition per step) over 1600 μm^2 area. All SERS spectra were collected with a portable Raman system equipped with a miniaturized camera stage attached to it (Figure 32). For sample analysis, the Au bowtie array substrates were mounted on the xyz stage to allow precise focusing and mapping of the entire surface. The incident laser was then focused onto the array substrates, and the scattered SERS signals were collected by the spectrograph /detector system. Each spectrum was accumulated over a period of 60 s and analyzed by ThermoGalactic GRAMS software.

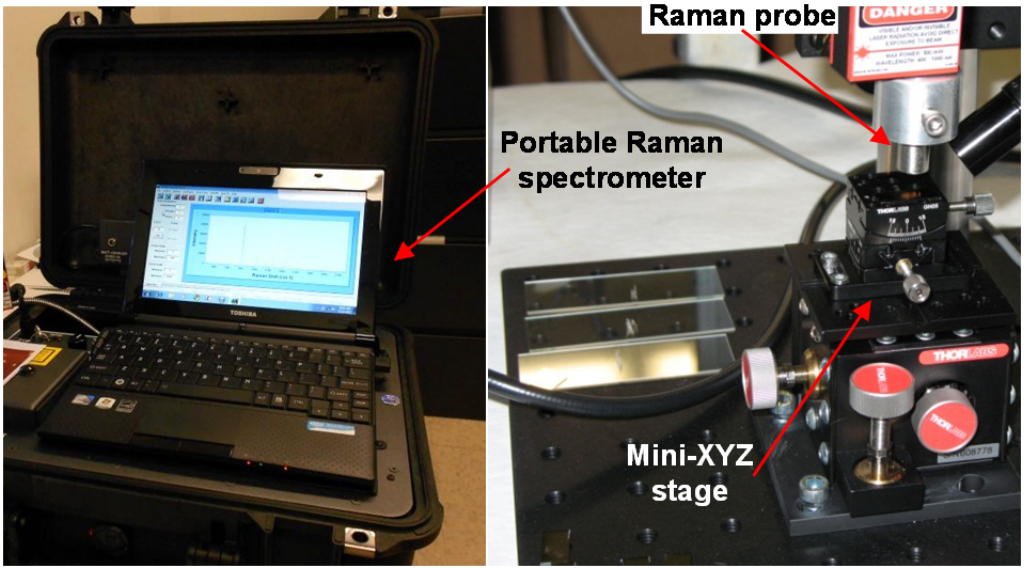

Figure 32. Illustration of a portable Raman sensor coupled with a fiber-optic Raman probe and a miniaturized XYZ stage.

Analyte samples and data acquisition: Standard solutions of ClO_4^- in the concentration range of 5×10^{-6} to 10^{-3} M were prepared from a stock solution of 1×10^{-2} M ClO_4^-. The calibration curves and reproducibility studies were performed on the same day and from the same wafer to reduce errors associated with instrument variation. A small droplet of standards or samples (~20 µL) were placed on the array substrate and subsequently analyzed after air drying.

To evaluate the applicability of the SERS probe for field analysis, contaminated groundwater samples were collected from several US Department of Defense facilities including US Naval Surface Warfare Centers (NSWC) at Dahlgren, VA (*Site 1*) and at Indian Head, MD (*Site 2*), and US Army Pueblo Chemical Depot at Pueblo, CO (*Site 3*). Samples were taken in accordance with EPA low-flow groundwater sampling procedures (PULS and BARCELONA, 1996). Groundwater samples were placed on ice immediately after collection and stored at 4^{o}C prior to analysis. The general characteristics and ionic compositions of these samples are shown in Table 3. Anions were measured by EPA Method 300, pH using a field meter, and TOC by EPA Method 415.1. To avoid potential matrix interferences due to unknown background organic or inorganic ions in the groundwater, the standard addition method was used whereby varying amounts of the ClO_4^- or TNT standard solution were added to a fixed amount of the groundwater. The final volumes were made up to 25 mL using DI water. The sample was then analyzed, and the characteristic Raman intensities at 947 cm^{-1} for ClO_4^- and 1367 cm^{-1} for TNT were plotted against the final concentration of each compound. A linear regression was used to calculate the absolute value of the X-intercept, which corresponds to the true concentrations of ClO_4^- or TNT in the groundwater.

Table 3. General geochemical properties of groundwater samples from Dahlgren NSWC (*Site 1*), Indian Head NSWC (*Site 2*), and Pueblo Chemical Depot (*Site 3*).

Sample Name	Chloride (mg/L)	Sulfate (mg/L)	Nitrate (mg/L)	Phosphate (mg/L)	TOC (mg/L)	pH
Site1						
GWOBOD02	8.4	9.5	1.2	<0.1	5	5.2
GWOBOD03	6.7	6.4	0.9	<0.1	3.4	5.45
Site 2						
MW-01	77.4	1.7	<0.1	<0.1	20.3	5.91
MW-04	193.0	13.5	1.6	<0.1	12.6	6.32
Site 3						
TNTMW38	23.8	94.8	8.8	<0.1	4.8	7.39

4.5.2 Results and Discussion: Portable Raman Sensor

We performed a series of tests of the portable Raman system by collecting SERS spectra of standard perchlorate solutions at concentrations ranging from 10^{-3} M to 10^{-6} M in water. Figure 33 shows the spectra of perchlorate, which are offset for clarity. The strongest SERS peak occurred at about 947 cm^{-1} as a result of the symmetric stretching vibration of the perchlorate molecule as previously shown for the laboratory instrument. This peak location is in close agreement with what has been previously reported in the literature (RUAN et al., 2006; WANG et al., 2006). The lowest ClO_4^- concentration used for the study with a notable Raman peak was ~ 5×10^{-6} M (500 μg/L). This detection is equivalent to an enhancement factor of 10^4 to 10^5 by SERS due to enhanced electromagnetic fields generated at or near the surface of the elevated gold bowtie arrays. The detection limit is comparable to or better than those reported in several previous studies (GU et al., 2009; GU et al., 2004; MOSIER-BOSS and LIEBERMAN, 2003a; MOSIER-BOSS and LIEBERMAN, 2003b; RUAN et al., 2006; WANG and GU, 2005; WANG et al., 2006), but it is about two orders of magnitude higher than detection limits reported recently using surface modified gold nanoparticles (RUAN et al., 2006; WANG et al., 2006). These observations represent the first reported case of ClO_4^- being detected using a portable Raman spectrometer on elevated gold bowtie array substrates. We also note that many previous studies reported the use of organic modifiers such as cystamine (RUAN et al., 2006), polyethyleneimine fragments containing primary amino and amide functional groups (TAN et al., 2007), and dimethylamino-ethanethiol (GU et al., 2009) in order to increase the sorption or surface concentration of ClO_4^-, leading to improved detection. One of the disadvantages of using these organic modifiers is the relatively high background scattering resulting from complicated molecular structures of the modifiers (e.g., cystamine and polyethyleneimine) (RUAN et al., 2006; TAN et al., 2007), which could potentially interfere with detection particularly at relatively high concentrations.

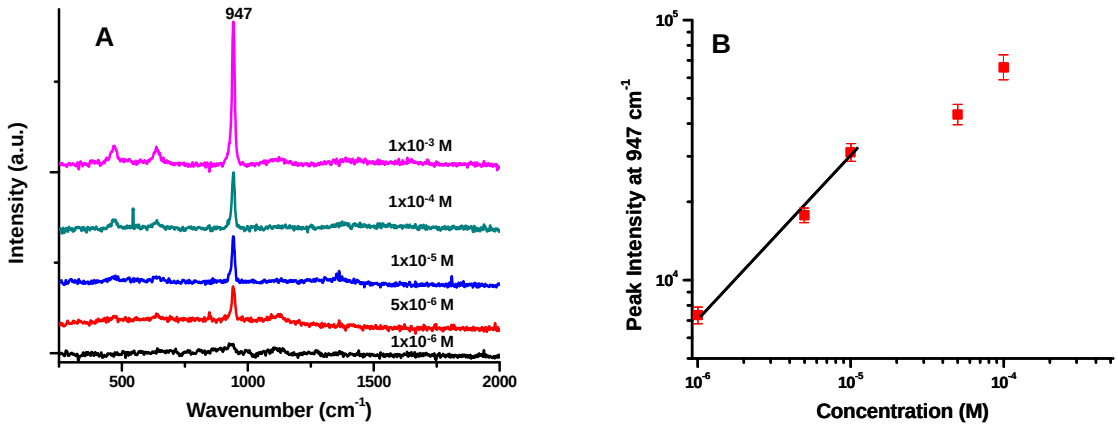

Figure 33. (A) Detection and spectral analysis of perchlorate (ClO_4^-) at varying concentrations using a portable Raman sensor. (B) A log-log plot of the peak intensity at 947 cm^{-1} as a function of the ClO_4^- concentration.

A log-log plot of the peak intensity of the primary Raman scattering band at 947 cm^{-1} indicates that, at relatively low perchlorate concentrations (1×10^{-6} M – 1×10^{-5} M), the peak intensity increases linearly with the perchlorate concentration (R^2=0.998), but it levels off at higher concentrations (5×10^{-5}M – 1×10^{-4}M) (Figure 33B). This nonlinear correlation between peak intensity and perchlorate concentration is common when using vibrational spectroscopic techniques such as SERS (GU and RUAN, 2007; GU et al., 2009). The observation is partially attributed to limited sorption sites within the gap region of the gold bowtie arrays and also a wide ClO_4^- concentration range used in the study. Nonetheless these results suggest that the technique can be used for quantitative or semi-quantitative analysis of ClO_4^- within a given concentration range.

Reproducible substrates are important for SERS to become a valuable tool for quantitative analysis. Figure 34 shows the SERS spectra collected from five different 1-mm^2 substrate arrays (A) or from five different spots within a given substrate array (B) in order to evaluate the reproducibility of the new bowtie substrates and the portable Raman system. Results indicate that, at a given ClO_4^- concentration (1×10^{-4} M), the spot-to-spot reproducibility is about 10% across five randomly selected spots (Figure 34B). These observations are attributed to the fact that EBL is capable of fabricating highly uniform or evenly distributed nanogaps with spatial resolution of nanometers serving as hot spots for ClO_4^- detection. As described earlier, although high enhancement has also been observed

on substrates such as metallic colloids and roughened electrode surfaces, reproducibility is an issue because it is difficult to achieve uniform particles, particle aggregates or nanogap sizes across a large measuring area for SERS. Nie and Emory reported that with silver colloids there are only a minute fraction of colloid nanoparticles that are likely to be SERS active or considered to be "hot" (NIE and EMORY, 1997). Therefore, the use of elevated gold bowtie arrays as SERS substrates shows clear advantages with respect to sensitivity and reproducibility for SERS applications.

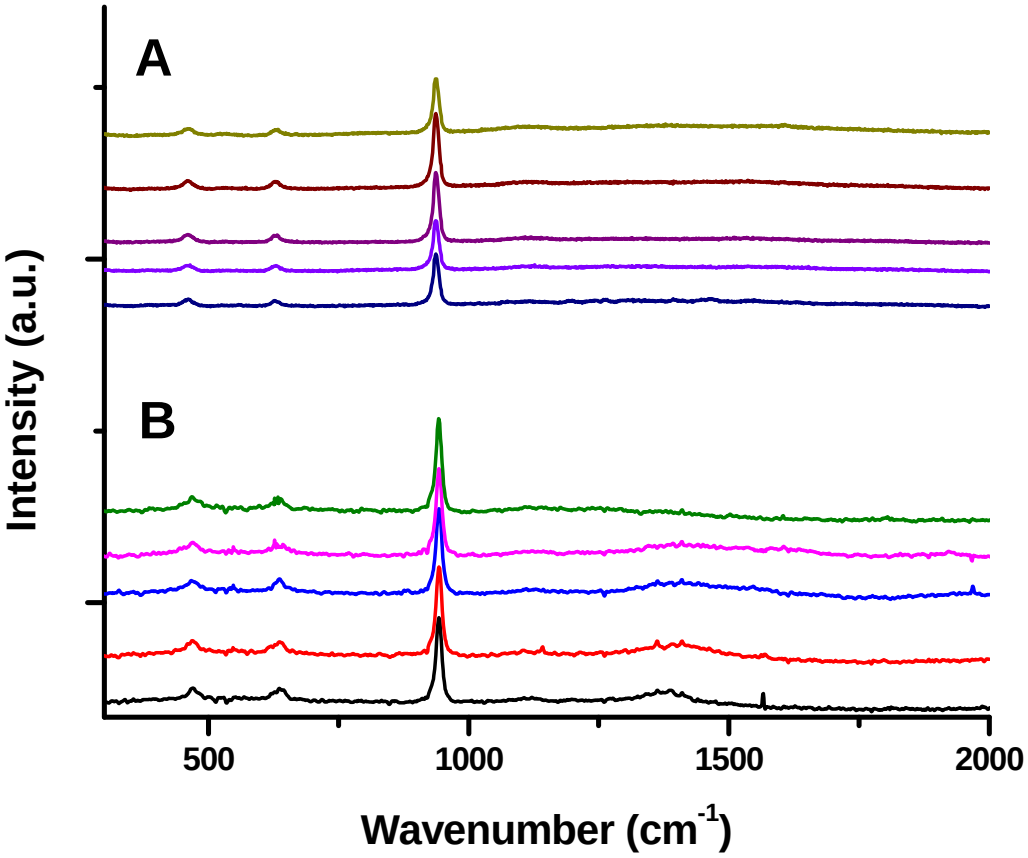

Figure 34. Reproducibility evaluation of the SERS sensor: (A) SERS spectra of ClO_4^- (1×10^{-4} M) obtained from five different gold bowtie array substrates, and (B) spectra of ClO_4^- (5×10^{-3} M) obtained from five different spots on a single gold bowtie array substrate.

To evaluate the applicability of the SERS sensing system for field applications, we collected and analyzed a number of realistic contaminated groundwater samples from several US Department of Defence sites (Table 3). As with many other techniques, analysis

of realistic environmental samples by SERS presents a challenge because samples often have multiple contaminants and complex geochemistry, resulting in interference with the analysis or false positive responses. This is further complicated by the fact that concentrations of the analytes of interest (ClO_4^- and TNT in this case) are usually orders of magnitude lower than organic and inorganic interfering ions such as total organic carbon (TOC), chloride and sulfate (Table 3). As a result, we used the standard addition technique to correct for matrix interferences (GU et al., 2009; HATAB et al., 2010a; SKOOG et al., 2000). Results are shown in Figures 35 and 36 as examples and all additional data are summarized in Table 4 along with the concentration data determined by standard EPA Method 314 for perchlorate and EPA Method 8330 for TNT for comparison.

For groundwater sample GWOBOD03, the major contaminant is ClO_4^-. Results reveal that the peak intensity for ClO_4^- at 947 cm^{-1} increased consistently with increasing concentration of the added ClO_4^- in solution (Figure 35). The measured concentration by SERS, which was 0.66±0.20 mg/L (~6.6 μM), compared favorably with that determined by IC via EPA Method 314 (i.e., 0.59 mg/L). The errors reported in the SERS perchlorate concentration data represent the standard deviation determined using the method by Skoog et al (SKOOG et al., 2000). For all groundwater samples, data analyzed by SERS are in general agreement with those analyzed by IC, but significant deviations occurred at relatively high ClO_4^- concentrations for MW-1 and MW-4 samples (Table 4). This deviation may be partially attributed to the non-linearity of the calibration curve measured by SERS, especially at relatively high concentrations. It is commonly observed by using spectroscopic techniques. Nonetheless, our results suggest that the portable Raman system could be useful as a convenient tool for rapid screening of environmental samples in the field.

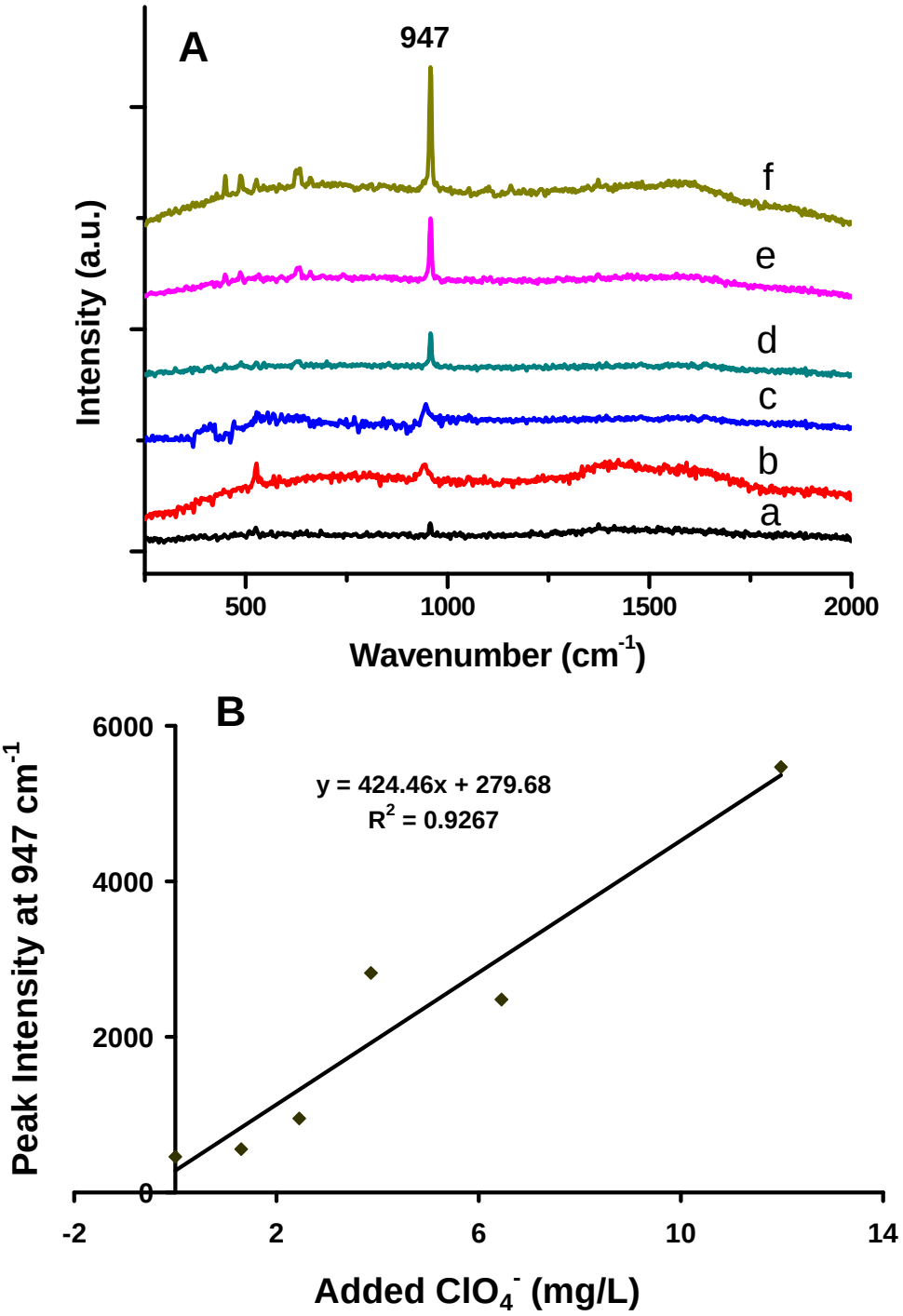

Figure 35. SERS determination of ClO_4^- in a contaminated groundwater sample (GWOBOD03) by the standard addition method. (A) SERS spectra with the addition of varying concentration of ClO_4^- at (a) 0, (b) 0.01, (c) 0.03, (d) 0.04, (e) 0.07, and (f) 0.12 mM. (B) The calibration curve for determining the actual ClO_4^- concentration in groundwater.

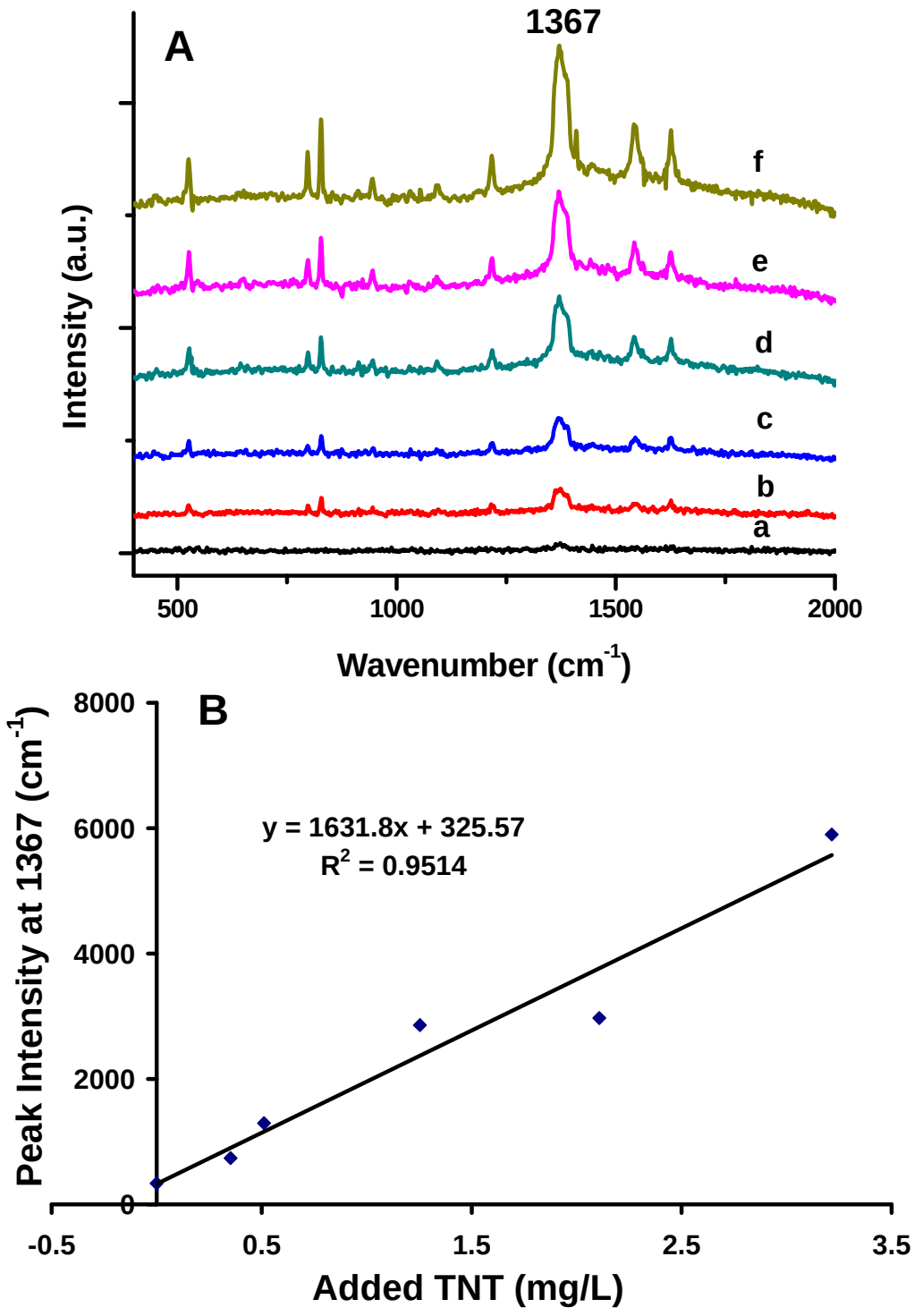

Figure 36. SERS determination of TNT in a contaminated groundwater sample (MW38) by the standard addition method. (A) SERS spectra with the addition of varying concentrations of TNT standard at (a) 0, (b) 1.6, (c) 2.3, (d) 5.5, (e) 9.3, and (f) 14.0 µM, and (B) the calibration curve for determining the actual TNT concentration in groundwater.

Table 4. Analysis of groundwater samples by the portable Raman sensor and comparisons of the analytical results with those determined by EPA Methods 314 and 8330 for ClO_4^- and TNT respectively.

Sample	Perchlorate (mg/L)		TNT (mg/L)	
	IC	SERS	HPLC	SERS
GWOBOD02	0.26	0.85	ND	ND
GWOBOD03	0.59	0.66	ND	ND
MW-01	18.4	11.5	ND	ND
MW-04	14.7	6.15	ND	ND
MW38	ND	ND	0.26	0.20

* ND = non-detect.

An additional advantage of using SERS is its versatility for detecting different contaminants or compounds either individually or simultaneously based upon the characteristic vibrational frequencies of the molecules (HAYNES et al., 2005; TAN et al., 2007). We have previously reported the use of SERS for detecting the explosive cyclotrimethylenetrinitramine **(**RDX) (Section 4.2) (HATAB et al., 2010a). Here we also show the use of a SERS sensor for detecting TNT in contaminated groundwater from a military site. The groundwater (sample MW38) is contaminated with TNT at 0.26 mg/L based on HPLC analysis using EPA Method 8330, but perchlorate was below detection by EPA Method 314 (< 0.001 mg/L) (Table 4). Similarly, using the standard addition technique, we observe that the TNT peak intensity at 1367 cm^{-1} increased consistently with increasing concentration of TNT in solution (Figure 36). The measured concentration by SERS was 0.20±0.11 mg/L (~ 0.9 μM), which agrees well with that determined by HPLC (Table 4). Our detection limit for TNT by SERS is comparable to that reported by Kneipp et al. for the detection of TNT (10^{-7} M) using silver and gold nanoparticles in laboratory prepared solutions (KNEIPP et al., 1995). However, it is higher than the detection limit recently reported using cysteine modified gold nanoparticles (DASARY et al., 2009). This is

not surprising, because, in addition to the use of modifiers, their analyses were performed in pure laboratory prepared solutions using a desktop Raman spectrometer.

4.5.3 Field Detection and Analysis

We subsequently conducted a field test of our portable Raman sensor for the detection of energetics in the contaminated groundwater at the US Naval Surface Warfare Center (NSWC) at Indian Head, MD. The primary purpose was to evaluate the performance of the portable Raman sensor for detection of energetics under realistic field environmental conditions.

Figure 37. (A) Field sampling and baseline groundwater characterization by Dr. Paul Hatzinger at the US NSWC site at Indian Head, MD. (B) Detection and analysis of groundwater contaminants using a field portable Raman sensor developed in this project by Dr. Nahla Hatab.

Figure 37A illustrates groundwater sampling and basic field parameter characterization at the site and Figure 37B shows the groundwater analysis using the portable Raman spectrometer. In this work, we analyzed groundwater samples from 4 monitoring wells, including CPMW-5, CPMW-2D, 1419-1, and CPMW-3S. The groundwater at this contaminated site contains ClO_4^- as the major energetics contaminant. No other energetics was detected in the groundwater. The groundwater samples were taken using the established low-flow sampling methodology (PULS and BARCELONA, 1996) and samples were then transfer onto the SERS substrate for direct analysis (without any pretreatment) by the portable Raman sensor. To avoid potential matrix interferences due to unknown background organic or inorganic materials in the groundwater, the standard addition method was used. In this methodology, a given amount of the ClO_4^- standard

solution (10 uL) was added to a fixed amount of the groundwater (1 mL). The samples were analyzed, and the characteristic Raman intensities at about 940 cm^{-1} for ClO_4^- were plotted against the final concentration of perchlorate. A linear regression was then used to calculate the absolute value of the X-intercept, which corresponds to the true concentration of ClO_4^- in the groundwater. The resulting ClO_4^- concentrations were 0.30, 0.69, 5.98 and 2.49 mg/L in CPMW-3S, 1419-1, CPMW-2D, and CPMW-5, respectively.

Similarly a split sample from the same monitoring well was taken and analyzed for major anions and energetics in the groundwater. Perchlorate was analyzed by EPA Method 314, and results are summarized in Table 5 below. The ClO_4^- concentration detected by the portable Raman sensor was in general agreement or in the same trend with those analyzed by the standard EPA method, but significant deviations were also observed. In particular, large deviations occurred for Samples CPMW-3S and CPMW-5, possibly due to defects, or misalignment of the laser beam, or the use of different SERS substrates for these samples. As stated earlier, SERS is particularly sensitive to where the laser spot shines on the gold bowtie arrays. Misalignments and defects on SERS substrates can cause large deviations of measured SERS intensity. Nonetheless, these results as well as results presented earlier (Section 4.5.2) represent the first step in developing a SERS-based field sensing system that could be potentially deployed in the field for rapid screening and analysis of energetics

Table 5. Analysis of major anions and perchlorate in the contaminated groundwater at the US NSWC site, Indian Head, MD. The unit for all anions is mg/L, and the unit for conductivity is μmhos/cm.

Groundwater Property	**Monitoring Well ID**			
	CPMW-3S	**1419-1**	**CPMW-2D**	**CPMW-5**
Chloride	2.02	49.4	25.1	2.86
Nitrate as N	0.54	3.37	1.46	0.30
Sulfate	82.6	41.8	63.0	46.6
Bromide	0.20	0.20	0.20	0.20
Phosphate as P	0.20	0.20	0.20	0.20
Perchlorate	0.027	1.76	4.87	0.40
Conductivity	292	384	288	273

in contaminated environments. In addition, this new SERS technology has the potential to be utilized as a tool for rapid screening of other chemical and biological agents that are important for environmental monitoring and are of interest to national security.

4.6 Potential Cost Savings by Using a Portable Raman Sensor

The ultimate goal of developing portable Raman sensor technology is to provide a significant cost savings to DoD for environmental monitoring and to allow better remedial decision making by giving program managers real-time data during site assessment and monitoring efforts. While an accurate estimation of cost-savings with this technology cannot be fully assessed until further validation and commercialization, for example, through DoD Environmental Security and Technology Certification program (ESTCP), we provide comparisons and preliminary analysis of potential cost savings when the sensor is ready to be deployed. The cost of the Raman sensor and its analysis on a per sample basis is estimated and compared below with those using standard groundwater analyses such as EPA Method 314 for perchlorate and EPA Method 8330 for TNT and RDX.

First, the capital equipment cost for a portable Raman sensor (including a SERS probe and Raman analyzer) is estimated to be about $20,000 to $25,000 at commercialization, whereas a typical IC or GC chromatograph costs about $30,000 to $40,000, and an IC-MS or GC-MS can easily cost greater than $150,000. Moreover the use of IC or GC requires substantial laboratory space preparation and accessories (such as compressed gas, water purification systems, and reagents). Therefore a portable Raman sensor can readily reduce the capital cost by more than 50% when compared with the use of GC, IC, or GC/IC-MS systems for in-house analysis.

Additional cost savings can be realized during field sampling and long-term monitoring and analysis. As an example, the costs for a typical day of groundwater sample collection by one field technician are as follows: 1) rental of field parameter meter for low flow sampling ($200/day); 2) rental of Grunfos pump, pump controller, and generator ($250/day); 3) disposable supplies ($20/day); 4) field labor (60 per hr × 8 hr; $480); 5) mileage, meal, and vehicle costs ($150/day); and (6) overnight cooler shipping ($100 per cooler). The typical cost for analysis of perchlorate by EPA Method 314.0 is $100 per

sample and analysis of energetics by EPA 8330 is $150 per sample. One technician can typically sample 6–8 wells in a day (allowing time for well stabilization by low-flow sampling and the set-up and break-down of equipment). Thus, based on a conservative assumption of sampling 6 wells containing explosives and perchlorate, the cost for 1 day of sampling and analysis is approximately $2,800. Moreover, a typical turnaround time for samples for perchlorate and energetics analysis is 2–3 weeks.

On the other hand, using a field portable Raman sensor, a qualified technician could be expected to sample a greater number of wells in a given day, since the time required for sample packaging and shipping to an analytical laboratory each day will be reduced. The cost for the SERS substrate is expected to be < $10 each upon commercialization, and the substrate may also be used for multi-component analyses, depending on groundwater chemistry and target molecules to be analyzed. Moreover, the ability to have real-time field measurements when monitoring remediation systems is likely to result not only in cost savings, but also in more effective and timely decision making during remediation projects. In many instances, decisions made concerning the location and screening of wells during site assessment work could be vastly improved if real-time contaminant data were available. Field-based analytical methods, such as that developed during this SERDP effort, are the best means to provide real-time data.

5.0 TECHNOLOGY TRANSFER

Five technical manuscripts from this work were published in *Applied Spectroscopy, Analyst, Nano Letters, Optics Express, and Raman Spectroscopy,* respectively (See Appendix A). In addition, two US patent or patent applications were filed, and one was granted in 2010. Three presentations were given at national and international scientific meetings or workshops between 2009 and 2011.

5.1 Publications

- Gu, B.; Ruan, C.; Wang, W. Perchlorate detection at nanomolar concentrations by surface-enhanced raman scattering. *Applied Spectroscopy* **2009**, 63, 98-102.
- Hatab, N. A., Hsueh, C. H., Gaddis, A., Retterer, S. T. Li, J. H., Eres, G., Zhang, Z., Gu, B. Free-standing optical gold bowtie nanoantenna with variable gap size for enhanced Raman spectroscopy. *Nano Letters*, 2010, 10, 4952-4955.
- Hatab, N. A.; Eres, G.; Hatzinger, P. B.; Gu, B., Detection and analysis of cyclotrimethylene-trinitramine (RDX) in environmental samples by surface enhanced Raman spectroscopy. *Journal of Raman Spectroscopy.* 2010, 41, 1131-1136.
- Hatab, N. A., Rouleau, C. M., Retterer, S. T., Eres, G., Hatzinger, P. B., Gu, B. An integrated portable Raman sensor with nanofabricated gold bowtie array substrates for energetics detection. *Analyst*, 2011, 136, 1697-1702.
- Xu, X.; Seal, K.; Xu, X.; Ivanov, I.; Hsueh, C. H.; Hatab, N. A.; Gu, B.; Zhang, Z.; Shen, J. High tunability of the SERS response with a metal-multiferroic composite. *Nano Letters,* 2011, 11, 1265-1269.
- Hsueh, C. H., Lin, C. H., Li, J. H., Hatab, N. A., Gu, B. 2011. Resonance modes, cavity field enhancements, and long-range collective photonic effects in periodic bowtie nanostructures. *Optics Express*, 19, 19660-19667.

5.2 Presentations

- Nahla A. Hatab, Gyula Eres, Scott Retterer, and Baohua Gu. Lithographically Produced Gold Arrays as Surface Enhanced Raman Spectroscopy Substrate, American Chemical Society Pittsburg Conference (Pittcon), March 2009, Pittsburgh, PA.
- Nahla A. Hatab, Paul Hatzinger, and Baohua Gu. Detection and Analysis of RDX, TNT, and other Energetics in Environmental Samples by Surface Enhanced Raman Spectroscopy, American Chemical Society Pittsburg Conference (Pittcon), March 2010, Pittsburgh, PA.
- Hatab, N. A., Rouleau, C. M., Retterer, S. T., Eres, G., Hatzinger, P. B., Gu, B. Energetics detection and analysis using an integrated portable Raman sensor with nanofabricated gold bowtie array substrates. The 242nd American Chemical Society National Meeting & Exposition, August 28-September 1, 2011, Denver, CO.

5.3 Patents and Patent Applications

- Baohua Gu, Chuanming Ruan and Wei Wang. 2010. Functionalized gold surface-enhanced Raman scattering substrate for rapid and ultra-sensitive detection of anionic species in the environment. (*US Patent, 12,645,017*).
- Baohua Gu, Nahla Abu Hatab, Scott T. Retterer, Gyula Eres, Zhenyu Zhang. 2011. The fabrication and use of elevated noble metallic nanostructures for enhanced Raman spectroscopy, plasmonic and optoelectronic applications. *U.S. patent pending.*

6.0 REFERENCES CITED

Böhlke, J. K., Sturchio, N. C., Gu, B., Horita, J., Brown, G. M., Jackson, W. A., and Batista, J. R., 2005. Perchlorate isotope forensics. *Anal. Chem.* **77**, 7838-7842.

Cahill, S. and Bulusu, S., 1993. Molecular complexes of explosives with cyclodextrins I: characterization of complexes with the nitramines RDX, HMX, and TNAZ in solution by 1H NMR spin-lattice relaxation time measurements. *Magne. Reson. Chem.* **31**, 731-735.

Calzzani, F., Chhay, B., Zimmerman, R., Oztarhan, A., and Ila, D., 2007. Nano- and micro-structural evolution of UHMWPE by ion beam. *Mater Res Soc Symp P* **1020**, 165-170.

Calzzani, J. F. A., Sileshi, R., Kassu, A., Taguenang, J. M., Chowdhury, A., Sharma, A., Ruffin, P. B., Brantley, C., and Edwards, E., 2008. Detection of residual traces of explosives by surface enhanced Raman scattering using gold coated substrates produced by nanospheres imprint technique. *SPIE*, 69451O.

Clausen, J., Cramer, R., Clough, S., Gray, M., and Gwinn, P., 2009. Assessing the sensitivity of quantitative structural activity analysis models for evaluating new military compounds. *Water Air Soil Poll.* **202**, 141-147.

Clausen, J. L., Korte, N., Dodson, M., Robb, J., and Rieven, S., 2006. Conceptual model for the transport of energetic residues from surface soil to groundwater by range activities. *ERDC-CRREL TR–06-18*, US Army Corps of Engineers, Environmental Research and Development Center, Cold Regions Research and Engineering Laboratory. Hanover, NH.

Crockett, A. J., Craig, H., and Sisk, W., 1998. *US Army Corps of Engineers, Cold Regions Research & Engineering Laboratory*, Special report 98-4.

Dasary, S. S. R., Singh, A. K., Senapati, D., Yu, H. T., and Ray, P. C., 2009. Gold nanoparticle based label-free SERS probe for ultrasensitive and selective detection of trinitrotoluene. *Journal of the American Chemical Society* **131**, 13806-13812.

Ding, Y. H., Zhang, X. M., Liu, X. X., and Guo, R., 2006. Adsorption characteristics of thionine on gold nanoparticles. *Langmuir* **22**, 2292-2298.

Docherty, F. T., Monaghan, P. B., McHugh, C. J., Graham, D., Smith, W. E., and Cooper, J. M., 2005. Simultaneous multianalyte identification of molecular species involved in terrorism using Raman spectroscopy. *IEEE Sensors J.* **5**, 632-640.

Dong, Z. C., Zhang, X. L., Gao, H. Y., Luo, Y., Zhang, C., Chen, L. G., Zhang, R., Tao, X., Zhang, Y., Yang, J. L., and Hou, J. G., 2010. Generation of molecular hot electroluminescence by resonant nanocavity plasmons. *Nature Photonics* **4**, 50-54.

Fang, Y., Seong, N. H., and Dlott, D. D., 2008. Measurement of the distribution of site enhancements in surface-enhanced Raman scattering. *Science* **321**, 388-392.

Fleischmann, M., Hendra, P. J., and McOuilan, A. J., 1974. Raman Spectra of Pyridine Adsorbed at a Silver Electrode. *Chem. Phys. Lett.* **26**, 163.

Freeman, D. H., Angeles, R. M., and Poinescu, I. C., 1976. High-performance liquid chromatographic separation of RDX and HMX explosives on adsorptive polymers. *J. Chromatogr. A.* **118**, 157-166.

Freeman, R. G., Grabar, K. C., Allison, K. J., Bright, R. M., Davis, J. A., Guthrie, A. P., Hommer, M. B., Jackson, M. A., Smith, P. C., Walter, D. G., and Natan, M. J., 1995. Self-assembled metal colloid Monolayers - an approach to SERS substrates. *Science* **267**, 1629-1632.

Fromm, D. P., Sundaramurthy, A., Kinkhabwala, A., Schuck, P. J., Kino, G. S., and Moerner, W. E., 2006. Exploring the chemical enhancement for surface-enhanced Raman scattering with Au bowtie nanoantennas. *J. Chem. Phys.* **124**, 061101.

Fromm, D. P., Sundaramurthy, A., Schuck, P. J., Kino, G., and Moerner, W. E., 2004. Gap-dependent optical coupling of single "Bowtie" nanoantennas resonant in the visible. *Nano Letters* **4**, 957-961.

Gu, B. and Brown, G. M., 2006. Recent advances in ion-exchange for perchlorate treatment, recovery and destruction. In: Gu, B. and Coates, J. D. Eds.), *Perchlorate Environmental Occurrences, Interactions, and Treatment*. Springer, New York.

Gu, B., Brown, G. M., and Chiang, C. C., 2007. Treatment of perchlorate-contaminated groundwater using highly selective, regenerable ion-exchange technologies. *Environ. Sci. Technol.* **41**, 6277-6282.

Gu, B. and Coates, J. D., 2006. *Perchlorate Environmental Occurrence, Interactions and Treatment*. Springer, New York.

Gu, B. and Ruan, C., 2007. Determination of technetium and its speciation by surface enhanced Raman spectroscopy. *Anal. Chem.* **79**, 2341-2345.

Gu, B., Ruan, C., and Wang, W., 2009. Perchlorate detection at nanomolar concentrations by surface-enhanced Raman scattering. *Appl. Spectr.* **63**, 98-102.

Gu, B., Tio, J., Wang, W., Ku, Y., and Dai, S., 2004. Raman spectroscopic detection for perchlorate at low concentrations. *Appl. Spectr.* **58**, 741-744.

Hatab, N. A., Eres, G., Hatzinger, P. B., and Gu, B., 2010a. Detection and analysis of cyclotrimethylene-trinitramine (RDX) in environmental samples by surface enhanced Raman spectroscopy. *J. Raman Spectr.* **41**, 1131-1136.

Hatab, N. A., Hsueh, C. H., Gaddis, A., Retterer, S. T., Li, J. H., Eres, G., Zhang, Z., and Gu, B., 2010b. Free-standing optical gold bowtie nanoantenna with variable gap size for enhanced Raman spectroscopy. *Nano Letters* **10**, 4952-4955.

Haynes, C. L., McFarland, A. D., and Van Duyne, R. P., 2005. Surface-enhanced Raman spectroscopy. *Analytical Chemistry* **77**, 338A-346A.

Haynes, C. L., McFarland, A. D., Zhao, L. L., Van Duyne, R. P., Schatz, G. C., Gunnarsson, L., Prikulis, J., Kasemo, B., and Kall, M., 2003. Nanoparticle optics: The importance of radiative dipole coupling in two-dimensional nanoparticle arrays. *J. Phys. Chem. B* **107**, 7337-7342.

Haynes, C. L. and Van Duyne, R. P., 2003. Plasmon-sampled surface-enhanced Raman excitation spectroscopy. *J. Phys. Chem. B* **107**, 7426-7433.

Hu, X. G., Wang, T., Wang, L., and Dong, S. J., 2007. Surface-enhanced Raman scattering of 4-aminothiophenol self-assembled monolayers in sandwich structure with nanoparticle shape dependence: Off-surface plasmon resonance condition. *J. Phys. Chem. C* **111**, 6962-6969.

Jackson, J. B. and Halas, N. J., 2004. Surface-enhanced Raman scattering on tunable plasmonic nanoparticle substrates. *PNAS USA* **101**, 17930-17935.

Jain, P. K., Huang, W. Y., and El-Sayed, M. A., 2007. On the universal scaling behavior of the distance decay of plasmon coupling in metal nanoparticle pairs: A plasmon ruler equation. *Nano Letters* **7**, 2080-2088.

Jiang, J., Bosnick, K., Maillard, M., and Brus, L., 2003. Single molecule Raman spectroscopy at the junctions of large Ag nanocrystals. *J. Phys. Chem. B* **107**, 9964-9972.

Karpowicz, R. J. and Brill, T. B., 1984. Insitu Characterization of the Melt Phase of Rdx and Hmx by Rapid-Scan Ftir Spectroscopy. *Combust Flame* **56**, 317-325.

Kim, S., Jin, J. H., Kim, Y. J., Park, I. Y., Kim, Y., and Kim, S. W., 2008. High-harmonic generation by resonant plasmon field enhancement. *Nature* **453**, 757-760.

Kinkhabwala, A., Yu, Z. F., Fan, S. H., Avlasevich, Y., Mullen, K., and Moerner, W. E., 2009. Large single-molecule fluorescence enhancements produced by a bowtie nanoantenna. *Nature Photonics* **3**, 654-657.

Kneipp, K., Kneipp, H., Itzkan, I., Dasari, R. R., and Feld, M. S., 1999. Ultrasensitive chemical analysis by Raman spectroscopy. *Chem. Rev.* **87**, 2957-2975.

Kneipp, K., Wang, Y., Dasari, R. R., Feld, M. S., Gilbert, B. D., Janni, J., and Steinfeld, J. I., 1995. Near-infrared surface-enhanced Raman scattering of trinitrotoluene on colloidal gold and silver. *Spectrochim. Acta A.* **51**, 2171-2175.

Kneipp, K., Wang, Y., Kneipp, H., Perelman, L. T., Itzkan, I., Dasari, R., and Feld, M. S., 1997. Single molecule detection using surface-enhanced Raman scattering (SERS). *Phys. Rev. Lett.* **78**, 1667-1670.

Michaels, A. M., Jiang, J., and Brus, L., 2000. Ag nanocrystal junctions as the site for surface-enhanced Raman scattering of single Rhodamine 6G molecules. *J. Phys. Chem. B* **104**, 11965-11971.

Mina, N., Cotte, I., Colon, Y., Ramos, C. M., Alzate, L. F., Hernandez-Rivera, S. P., Castro, M. E., Chamberlain, R. T., and Lareau, R. T., 2003. *SPIE*, 363.

Moore, D. S. and Scharff, R. J., 2009. Portable Raman explosives detection. *Analytical and Bioanalytical Chemistry* **393**, 1571-1578.

Mosier-Boss, P. A. and Lieberman, S. H., 2003a. Detection of anions by normal Raman spectroscopy and surface enhanced Raman spectroscopy of cationic-coated substrates. *Appl. Spectr.* **57**, 1129-1137.

Mosier-Boss, P. A. and Lieberman, S. H., 2003b. Surface-enhanced Raman spectroscopy (SERS) and molecular modeling of the chromate interaction with 4-(2-mercaptoethyl)pyridinium. *Langmuir* **19**, 6826-6836.

Niaura, G. and Jakubenas, R., 2001. The alkali metal cation effect on the surface-enhanced Raman spectra of phosphate anions adsorbed at silver electrodes. *J. Electroanal. Chem.* **510**, 50-58.

Nie, S. and Emory, S. R., 1997. Probing single molecules and single nanoparticles by surface-enhanced Raman scattering. *Science* **275**, 1102-1106.

Olson, L. G., Lo, Y. S., Beebe, T. P., and Harris, J. M., 2001. Characterization of silane-modified immobilized gold colloids as a substrate for surface-enhanced Raman spectroscopy. *Anal. Chem.* **73**, 4268-4276.

Primera-Pedrozo, O. M., Jerez-Rozo, J. I., De la Cruz-Montoya, E., Luna-Pineda, T., Pacheco-Londono, L. C., and Hernandez-Rivera, S. P., 2008. Nanotechnology-based detection of explosives and biological agents simulants. *Ieee Sens J* **8**, 963-973.

Puls, R. W. and Barcelona, M. J., 1996. Low-Flow (Minimal Drawdown) Ground-Water Sampling Procedures. *Office of Research and Development, Office of Solid Waste and Emergency Response*, EPA/540/S-95/504.

Qin, L. D., Zou, S. L., Xue, C., Atkinson, A., Schatz, G. C., and Mirkin, C. A., 2006. Designing, fabricating, and imaging Raman hot spots. *PNAS USA* **103**, 13300-13303.

Ruan, C. M., Gu, B., Wang, W., Eres, G., and Zhang, Z., 2007a. Controlled fabrication of nanopillar array substrates for surface-enhanced Raman spectroscopy. *Langmuir* **23**, 5757-5760.

Ruan, C. M., Gu, B., Wang, W., Eres, G., and Zhang, Z., 2007b. Controlled fabrication of nanopillar array substrates for surface-enhanced Raman spectroscopy. *Langmuir*, (in press).

Ruan, C. M., Wang, W., and Gu, B., 2006. Surface-enhanced Raman scattering for perchlorate detection using cystamine-modified gold nanoparticles. *Anal Chim Acta* **567**, 114-120.

Ruan, C. M., Wang, W., and Gu, B., 2007c. Determining uranium in environmental samples by surface-enhanced Raman spectroscopy. *Anal Chim Acta* **605**, 80-86.

Ruan, C. M., Wang, W., and Gu, B., 2007d. Single-molecule detection of thionine on aggregated gold nanoparticles by surface enhanced Raman scattering. *J. Raman Spectr.* **38**, 568-573.

Sackmann, M. and Materny, A., 2006. Surface enhanced Raman scattering (SERS) - a quantitative analytical tool? *J. Raman Spectr.* **37**, 305-310.

Sass, J., 2004. US Department of Defense and white house working together to avoid cleanup and liability for perchlorate pollution. *International Journal of Occupational and Environmental Health* **10**, 330-334.

Saxena, A., Fujiki, M., Rai, R., and Kwak, G., 2005. Fluoroalkylated polysilane film as a chemosensor for explosive nitroaromatic compounds. *Chem. Mater.* **17**, 2181-2185.

Skoog, D. A., West, D. M., Holler, F. J., and Crouch, S. R., 2000. Analytical Chemistry, An Introduction. 7th ed. Harcourt College, Orlando, Florida, p 601.

Suidan, M. T., Atikovic, E., and Maloney, S. W., 2008. Anaerobic treatment of army ammunition production wastewater containing perchlorate and RDX. *Chemosphere* **72**, 1643-1648.

Sundaramurthy, A., Crozier, K. B., Kino, G. S., Fromm, D. P., Schuck, P. J., and Moerner, W. E., 2005. Field enhancement and gap-dependent resonance in a system of two opposing tip-to-tip Au nanotriangles. *Phys. Rev. B* **72**, 1098-0121.

Sylvia, J. M., Janni, J. A., Klein, J. D., and Spencer, K. M., 2000. Surface-enhanced Raman detection of 1,4-dinitrotoluene impurity vapor as a marker to locate landmines. *Analytical Chemistry* **72**, 5834-5840.

Tan, S., Erol, M., Attygalle, A., Du, H., and Sukhishvili, S., 2007. Synthesis of positively charged silver nanoparticles via photoreduction of AgNO3 in branched polyethyleneimine/HEPES solutions. *Langmuir* **23**, 9836-9843.

Torres, P., Mercado, L., Cotte, I., Hernandez, S. P., Mina, N., Santana, A., Chamberlain, R. T., Lareau, R., and Castro, M. E., 2004. Vibrational spectroscopy study of beta and alpha RDX deposits. *Journal of Physical Chemistry B* **108**, 8799-8805.

Wang, W. and Gu, B., 2005. New surface-enhanced Raman spectroscopy substrates via self-assembly of silver nanoparticles on surface functionalized glass for perchlorate detection. *Appl. Spectr.* **59**, 1509-1515.

Wang, W., Ruan, C. M., and Gu, B., 2006. Development of gold-silica composite nanoparticle substrates for perchlorate detection by surface-enhanced Raman spectroscopy. *Anal Chim Acta* **567**, 121-126.

Wani, A. H., Felt, D. R., and Davis, J. L., 2003. Biologically active zone enhancement (BAZE) supplemental study: mass balance of RDX biotransformation and influence of aquifer temperature on RDX biodegradation in groundwater. *Technical Report ERDC/EL TR-03-11*, US Army Corps of Engineers, Engineer Research and Development Center, Vicksburg, MS.

Weisbecker, C. S., Merritt, M. V., and Whitesides, G. M., 1996. Molecular self-assembly of aliphatic thiols on gold colloids. *Langmuir* **12**, 3763-3772.

Wells, S. M., Retterer, S. D., Oran, J. M., and Sepaniak, M. J., 2009. Controllable nanotabrication of aggregate-like nanoparticle substrates and evaluation for surface-enhanced Raman spectroscopy. *ACS Nano* **3**, 3845-3853.

Xu, H., Aizpura, J., Kall, M., and Apell, P., 2000. Electromagnetic contributions to single-molecule sensitivity in surface-enhanced Raman scattering. *Phys. Rev. E* **62**, 4318-4324.

Zhao, K., Xu, H., Gu, B., and Zhang, Z., 2006. One-dimensional arrays of nanoshell dimers for single molecule spectroscopy via surface-enhanced Raman scattering. *J. Chem. Phys.* **125**, 081102.

Zhao, L. L., Kelly, K. L., and Schatz, G. C., 2003. The extinction spectra of silver nanoparticle arrays: Influence of array structure on plasmon resonance wavelength and width. *J. Phys. Chem. B* **107**, 7343-7350.

Zhong, Z. Y., Patskovskyy, S., Bouvrette, P., Luong, J. H. T., and Gedanken, A., 2004. The surface chemistry of Au colloids and their interactions with functional amino acids. *J. Phys. Chem. B.* **108**, 4046-4052.

Zou, S. L. and Schatz, G. C., 2005. Silver nanoparticle array structures that produce giant enhancements in electromagnetic fields. *Chem. Phys. Lett.* **403**, 62-67.

Zuloaga, J., Prodan, E., and Nordlander, P., 2009. Quantum description of the plasmon resonances of a nanoparticle dimer. *Nano Letters* **9**, 887-891.

7.0 CONCLUSIONS AND IMPLICATIONS FOR FUTURE RESEARCH AND IMPLEMENTATION

SERS is a technique that provides orders of magnitude higher enhanced Raman signal from analyte molecules that are adsorbed onto specially prepared noble metal surfaces. Such surfaces are usually made with nanostructured gold (Au) or silver (Ag) arrays, enabling the detection of analyte molecules at ultra-trace concentration levels. In comparison with fluorescence and optical absorption spectroscopic techniques, SERS is more sensitive with greater molecular selectivity (or fingerprinting) due to the molecular vibrational information provided by the Raman spectroscopy. The key is the fabrication of sensitive and reproducible SERS substrates using techniques such as wet-chemical and electron-beam lithography (EBL) nano-fabrication. The SERS substrate is then integrated with a portable Raman analyzer via a fiber optic sensor probe, allowing real-time or in-situ detection and analysis of contaminants in groundwater or surface water. Summarized below are major accomplishments resulting from this SERDP project.

- Developed and constructed an integrated, portable SERS-Raman sensor for energetics (ClO_4^-, TNT, RDX) detection and analysis;
- Fabricated and systematically evaluated a range of SERS substrates using wet-chemical and new EBL nano-fabrication techniques;
- Demonstrated the detection of ClO_4^-, TNT and RDX at concentrations as low as ~ 1, 2.3, and 120 μg/L, respectively, in contaminated water;
- Developed and demonstrated large SERS enhancement factors exceeding 10^{11} resulting from a novel EBL-fabricated gold bowtie arrays with controllable gap sizes to < 8 nm;
- Published 5 peer-reviewed journal articles related to the development and application of SERS technology for energetics detection;
- Filed 2 US patent applications (one granted and one pending) on nano-fabrication of SERS substrates; and
- Tested and evaluated the performance of the portable Raman sensor at limited numbers of contaminated DoD field sites.

This work represents the first step in developing a SERS/Raman based field sensor that combines a portable Raman spectrometer with novel elevated gold bowtie arrays. While we made significant advancement in SERS technology during last three years, as noted above, challenges remain to develop a field deployable and reliable portable Raman sensor. This is because SERS is particularly sensitive to where the laser spot shines on the SERS substrate, and misalignments and defects on SERS substrates can cause large deviation of measured SERS intensity and thus affect the quality of analytical results. Matrix interferences from environmental samples are also a concern, although this can usually be resolved by using the same or similar matrices for quantitative analysis or the standard addition technique. Future work can be directed to increase the reliability of quantification, optimize the sensitivity, and mass-produce SERS substrates at large scales. Additional work may be directed for detecting other contaminants of concern such as RDX, insensitive munition compositions, 2,4-dinitroanisol, and volatile organic compounds because SERS in principle can be used to detect any molecules that give Raman signal. Through further field validation and demonstration, a cost reduction of up to 50% may be realized using the portable Raman sensor because sample shipping and typical costs associated with laboratory analysis can be eliminated. The technology has the potential to provide a tool for rapid, in-situ screening and analysis of energetics and other chemical and biological agents that are both important for environmental monitoring and of interest for national security.

8.0 POINTS OF CONTACT

POINT OF CONTACT	ORGANIZATION	PHONE/FAX/EMAIL
Dr. Baohua Gu	Environmental Sciences Division Oak Ridge National Laboratory P. O. Box 2008, MS-6036 Oak Ridge, TN 37831	865-574-7286 (phone) 865-576-8543 (fax) gub1@ornl.gov
Dr. Paul B. Hatzinger	Shaw Environmental, Inc. 17 Princess Road Lawrenceville, NJ 08648	609-895-5356 (phone) 609-895-1858 (fax) Paul.hatzinger@shawgrp.com
Dr. Pamela A. Boss	Space and Naval Warfare Systems Center, Code 2373 San Diego, CA 92152	619-553-1603 (phone) 603-767-4339 (fax) pam.boss@navy.mil
Dr. Andrea Leeson	SERDP/ESTCP 901 N Stuart Street, Suite 303 Arlington VA 22203	703-696-2118 (phone) 703-696-2114 (fax) Andrea.leeson@osd.mil

9.0 APPENDIX A

Attached below are 5 peer-reviewed publications resulting from this project.

Perchlorate Detection at Nanomolar Concentrations by Surface-Enhanced Raman Scattering

BAOHUA GU,* CHUANMIN RUAN, and WEI WANG

Environmental Sciences Division, Oak Ridge National Laboratory, Oak Ridge, Tennessee 37831 (B.G., W.W.); and Oak Ridge Institute for Science and Education, Oak Ridge, Tennessee 37831 (C.R.)

Perchlorate (ClO_4^-) has emerged as a widespread environmental contaminant and has been detected in various food products and even in human breast milk and urine. This research developed a sensing technique based on surface-enhanced Raman scattering (SERS) for rapid screening and monitoring of this contaminant in groundwater and surface water. The technique was found to be capable of detecting ClO_4^- at concentrations as low as 10^{-9} M (or ~0.1 μg/L) by using 2-dimethylaminoethanethiol (DMAE) modified gold nanoparticles as a SERS substrate. Quantitative analysis of ClO_4^- was validated with good reproducibility by using both simulated and contaminated groundwater samples. When coupled with a portable Raman spectrometer, this technique thus has the potential to be used as an *in situ*, rapid screening tool for perchlorate in the environment.

Index Headings: **Perchlorate; Detection limit; Surface-enhanced Raman scattering; SERS; Sensor; Groundwater; Gold nanoparticles.**

INTRODUCTION

New technologies for rapid screening and quantitative analysis of perchlorate (ClO_4^-) in the environment are of great interest since perchlorate has emerged as a widespread contaminant in groundwater and surface water in the United States (US).[1–4] Perchlorate has been detected in drinking water, plants, food products, and human urine and breast milk in many areas of the US and abroad.[5–8] Perchlorate is manufactured primarily for use as an ingredient of solid rocket propellant and explosives but is also known to form naturally, such as that found in the hyperarid Atacama Desert in Chile.[1–3,9–11] Recent studies also indicate that naturally forming perchlorate is more widespread than originally thought (only in the arid regions), and this explains the wide occurrences of sub-parts per billion (ppb) concentration levels of perchlorate in the environment where no anthropogenic sources are known to exist.[10,12–14] Because of its potential health effects on thyroid function by interfering with iodide uptake, the widespread occurrence of perchlorate in the environment has generated considerable interest in its contamination source, risk assessment, and detection and remediation technologies. Perchlorate is highly soluble and exceedingly mobile in aqueous systems and can persist for many decades under typical groundwater and surface water conditions.[15] Therefore, methods for rapid and sensitive assay of this contaminant are particularly useful for its monitoring and detection in the environment.

Various techniques such as ion chromatography (IC),[14,16] electro-spray mass spectrometry (MS), IC-MS, and IC-MS-MS,[2,17] ion-selective electrodes,[18,19] and capillary electrophoresis[17,20] have been well developed and are routinely used for perchlorate detection and analysis. Currently, IC is perhaps the most commonly used technique for the analysis and screening of perchlorate in environmental samples, although IC-MS or EPA Methods 6850 and 6860 are preferred because of the specificity of MS in identifying ClO_4^- in complex environmental matrices. However, these methods are usually performed in analytical laboratories and require sample preparation and lengthy analytical time. For rapid screening and long-term monitoring, *in situ*, nondestructive, and sensitive analysis of ClO_4^- is highly preferred. Ion-selective electrodes have been developed for such purposes, but their sensitivity and selectivity remain an issue to be improved.[17–19]

The surface-enhanced Raman scattering (SERS) technique has the potential to allow rapid, sensitive, and *in situ* detection of ClO_4^-. SERS refers to the observation that the apparent Raman cross-section for an analyte adsorbed on roughened metal surfaces (e.g., silver or gold) is enhanced by many orders of magnitude over their normal values, allowing the detection up to single molecular levels.[21–24] The characteristic vibrational frequency of the symmetric stretch for ClO_4^- at about 950 cm^{-1} (dehydrated) and 930 cm^{-1} (in aqueous solution) also makes the technique highly selective. However, the key for this technology to be useful is the development of robust, sensitive, and reproducible SERS substrates, on which the Raman signal could be substantially enhanced. Using roughened gold electrode surfaces in a flow cell, previous studies have shown that the technique was capable of detecting ClO_4^- at 10^{-4}–10^{-5} M concentration levels,[25] and recent investigations reached a detection limit of about 10^{-6}–10^{-7} M by using surface-modified gold or silver nanoparticles as SERS substrates.[26–29] However, improved sensitivity (e.g., $<10^{-8}$ M), reproducibility, stability, and uniformity remain significant issues before SERS can be used as a routine analytical tool for ClO_4^- detection. Additionally, the quantitative relation or linearity has been found only within limited concentration ranges of the analyte or is nonexistent because of problems associated with poor reproducibility and substrate stability.[25,27,30–33] The surface modification, which may allow analyte to be sorbed or concentrated and distributed uniformly on a substrate, has been proposed as one of the key steps for enhancing the sensitivity, reproducibility and linearity of SERS.[26–28,30–32] Here we report a new SERS technique for detecting ClO_4^- at concentrations as low as 10^{-9} M (or 0.1 ppb) by using 2-dimethylaminoethanethiol (DMAE) modified gold nanoparticles as a SERS substrate.

MATERIALS AND METHODS

All chemicals used in this experiment were of reagent grade or better. Gold chloride trihydrate ($HAuCl_4 \cdot 3H_2O$), nitric acid (HNO_3) (70%), 2-(dimethylamino)-ethanethiol hydrochloride (DMAE) [$(CH_3)_2NCH_2CH_2SH \cdot HCl$] (98%), sodium citrate

Received 4 August 2008; accepted 17 October 2009.
* Author to whom correspondence should be sent. E-mail: gub1@ornl.gov.

0003-7028/09/6301-000000$2.00/0

TABLE I. Major anionic composition of two field groundwater samples (GW-1 and GW-2) and a simulated groundwater sample (SGW).

Property	SGW	GW-1	GW-2
Perchlorate (μM)	0–1	8.3	0.01
Chloride (mM)	1.0	0.28	3.0
Sulfate (mM)	0.1	0.16	0.49
Nitrate (mM)	0.1	0.16	0.52
Phosphate (mM)	0.1	ND[a]	ND
Bicarbonate (mM)	0	2.8	3.1
pH	6.5	7.3	8

[a] D = non-detectable.

($Na_3C_6H_5O_7$) (98%), sodium borohydride ($NaBH_4$) (98%), and hydrochloric acid (HCl) (36.5%) were obtained from Aldrich (St. Louis, MO). Sodium perchlorate ($NaClO_4 \cdot H_2O$) was purchased from EM Science (Cherry Hill, NJ). Micro-glass slides were from Corning Glass Works (Corning, NY). For substrate and solution preparations, deionized water (18.2 MΩ cm^{-1}) was used throughout the experiment. All glassware was cleaned in a freshly prepared acid bath and rinsed thoroughly with deionized water prior to use.

Colloidal Au nanoparticles were prepared according to previously published methods.[30,34] In brief, a "seed" colloidal suspension of Au was first prepared by mixing 1 mL of 1% aqueous $HAuCl_4 \cdot 3H_2O$ in 100 mL of H_2O with vigorous stirring for about 1 min, followed by sequential additions of 1 mL of 1% trisodium citrate and 1 mL of 0.075% $NaBH_4$ in 1% trisodium citrate. This seed Au suspension was stirred continuously for an additional 5 min and then stored at 4 °C. Au nanoparticles of ~54 nm in diameter were then prepared by heating 900 mL of dilute $HAuCl_4$ solution (~0.004%) to boiling, followed by the addition of 1 mL of the "seed" Au nanoparticles and 3.6 mL of a 1% trisodium citrate solution. The solution mixture was refluxed for an additional 10 min before it was cooled under stirring. The average size of synthesized Au nanoparticles (~54 nm) was determined by means of dynamic light scattering using a ZetaPlus particle size analyzer (Brookhaven Instruments, Holtsville, NY). Data were collected for every batch of the Au colloid at room temperature.

The DMAE-modified Au nanoparticles were prepared by adding 0.28 g DMAE into 400 mL of the above prepared Au colloid suspension, upon which the color of the Au colloids immediately turned from red to deep purple, suggesting the aggregation of Au nanoparticles by interacting with DMAE. The UV-visible spectrum showed a red shift in its primary absorption maxima from 525 to 790 nm, the latter of which is attributed to multipolar resonances of Au nanoparticles in higher-order coupled spheres.[35,36] After mixing for approximately 5 h, the suspension was centrifuged at 14 000 rpm, and the concentrated Au nanoparticles were collected, washed with deionized water, and re-suspended in 0.01 M HCl solution (pH ~ 2) and used as a SERS substrate for perchlorate detection. This concentrated Au nanoparticle suspension was found to be stable for at least 8 months (after preparation), although ultrasonification is necessary to ensure well dispersed Au colloids before use.

For SERS analysis, the analyte ClO_4^- solution in the concentration range of 10^{-9} to 10^{-4} M was prepared by dilution in series (10×) from a stock solution of 10^{-3} M in deionized water. To evaluate potential matrix interferences from competing ions, measurements were also performed in a synthetic groundwater (SGW) consisting of a mixture of SO_4^{2-}, PO_4^{3-}, and NO_3^-, each at 10^{-4} M, and Cl^- at 10^{-3} M. In addition, two contaminated groundwater samples (GW-1 and GW-2) were obtained from a field site in northern California and used for testing. Table I lists major anionic compositions and pH of the groundwater and SGW. The analyte, SGW, or GW samples (0.1 mL) were then mixed with 0.1 mL of the modified Au nanoparticle concentrate and 0.8 mL of water for analysis. A small drop (~10 μL) of the mixed suspension was placed on a glass slide and air-dried, and SERS spectra were collected after about 30 min.

Raman spectra were obtained using the Renishaw micro-Raman system equipped with a near-infrared diode laser at a wavelength of 785 nm for excitation (Renishaw Inc, New Mills, UK).[26,27,30] The laser beam was set in position with a Leica Raman imaging microscope equipped with a 50× objective lens (0.5 numerical aperture) at a lateral spatial resolution of ~2 μm. The optics polarization was set perpendicular to the laser, and its intensity at the exit of the objective lens was ~1 mW by using a set of neutral density filters. A charge-coupled device (CCD) array detector was used to achieve signal detection from a 1200 grooves/mm grating light path controlled by Renishaw WiRE software and analyzed by Galactic GRAMS software.

RESULTS AND DISCUSSION

Quantitative Analysis of Perchlorate. Surface-enhanced Raman scattering spectra of perchlorate were first examined at concentrations ranging from 10^{-10} to 10^{-6} M in purified water, and each spectrum in Fig. 1A was offset for clarity. The primary Raman scattering peak (due to symmetric stretching vibration) of ClO_4^- occurred at about 934 cm^{-1}, which is consistent with literature data using both normal and surface-enhanced Raman spectroscopic techniques.[25–27,29] The lowest ClO_4^- concentration detected was about 10^{-10} M, and a small ClO_4^- peak was visible (spectrum b). However, the detection limit was estimated at 10^{-9} M (or ~100 ng/L) with a signal-to-noise ratio greater than 3. These results suggest that the SERS technique was extremely sensitive to ClO_4^- through the use of DMAE-modified Au nanoparticle substrates. This detection limit is about two orders of magnitude lower than those reported recently by using either cystamine-modified gold nanoparticles[27] or positively charged silver nanoparticles sorbed with polyethyleneimine fragments (containing primary amino and amide functional groups).[29] These techniques give a relatively high background scattering resulting from complicated molecular structures of the organic modifiers (both cystamine and polyethyleneimine or its fragments).[27,29] The background scattering in the spectral region between 900 and 950 cm^{-1} could interfere with the detection of ClO_4^- or overlap with the Raman band of ClO_4^-, especially at submicromolar concentration levels. On the other hand, no significant background Raman scattering was observed in the spectral region of ~890–960 cm^{-1} by using DMAE-modified Au nanoparticles as SERS substrates (Fig. 1A, spectrum a).

To our knowledge, this is the first time that DMAE has been used as a modifier for SERS detection of ClO_4^-. The rationale for using DMAE is based on the development of selective ion exchangers for ClO_4^- sorption, in which the selectivity is found to strongly depend on the charge and size of the quaternary alkyl-ammonium functional groups.[3,37] The electrostatic attraction between ClO_4^- anions and positively

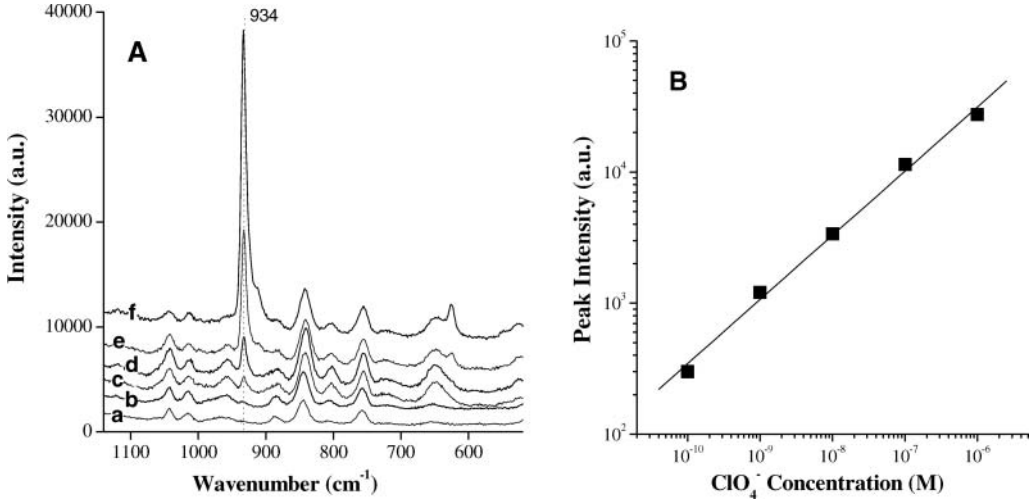

FIG. 1. (**A**) Raman spectroscopic analysis of ClO_4^- at concentrations of (***a***) 0, (***b***) 10^{-10}, (***c***) 10^{-9}, (***d***) 10^{-8}, (***e***) 10^{-7}, and (***f***) 10^{-6} M using DMAE-modified Au nanoparticles as a SERS substrate; (**B**) a log-log plot of the peak intensity at 934 cm^{-1} against the ClO_4^- concentration.

charged DMAE-modified Au nanoparticles enables a close contact and the higher concentration of ClO_4^- onto Au nanoparticle surfaces.[26,27] Additionally, the amine functional groups could have facilitated the aggregation of Au nanoparticles, which is necessary to obtain strong electromagnetic plasmon enhancement on gold metal surfaces.[21–23] Theoretical calculations have shown that the maximal SERS signal could be obtained when the analyte molecule is situated within the nanoneck regions of adjacent metal nanoparticles, where maximal electromagnetic field enhancement is achieved upon laser excitation.[21,38] Therefore, the use of DMAE-modified Au SERS substrates offers advantages in sensitive detection of ClO_4^- in aqueous media. It yielded an enhancement factor of about 10^7–10^8 because, by using normal Raman spectroscopy (or without using Au nanoparticles), no Raman signal could be detected directly from the aqueous solution at perchlorate concentrations below 10^{-2} M.[27]

Analysis of the spectra (Fig. 1A) also showed that the Raman band at 934 cm^{-1} increased consistently with an increase of aqueous ClO_4^- concentrations. A logarithm plot between the peak intensity and the ClO_4^- concentration yielded a linear relationship over a wide concentration range between 10^{-10} and 10^{-6} M (Fig. 1B). This observation is consistent with that observed for the detection of pertechnetate (TcO_4^-) ions by using similar techniques.[30] Sackmann and Materby also reported that the SERS intensity of adenine increased exponentially with its concentration when silver colloids were used as a SERS substrate.[33] These observations suggest that the technique could potentially be used as a quantitative or semi-quantitative tool for the analysis or rapid screening of perchlorate in aqueous media.

The surface modification of Au nanoparticles with DMAE enabled not only a high sensitivity but also a good reproducibility in detecting ClO_4^- in aqueous solution. The spot-to-spot reproducibility of Raman signal at 934 cm^{-1} was evaluated by randomly selecting about six spots under the microscope and measuring their corresponding SERS spectra (Fig. 2). Results indicate that all spectra virtually overlap (note that a small *y*-axis offset was used for clarity). The standard deviation of the peak intensity at 934 cm^{-1} was about 16% from these different spots. Similarly, the batch-to-batch variations were found to be about ±15% when different batches of the modified Au nanoparticles were used. These observations are attributed to the fact that the positively charged amine functional groups result in the sorption and thus an even distribution of ClO_4^- on Au nanoparticles. Also, as indicated earlier, the amine functional groups could have facilitated the aggregation of Au colloids, as evidenced by the self-assembly of DMAE-modified Au nanoparticles (Fig. 2, inset). Without surface modification, the analyte would be unlikely to be distributed evenly when it dries or crystallizes on metal nanoparticle surfaces (one of the contributing factors to observations of so-called "hot spots"). The probability of finding such hot spots is usually extremely low for detecting the target analyte.[22,23] Nie and Emory have shown that about one in 100 to 1000 silver colloids are perhaps "hot" or SERS-active.[22] This has been a major limiting factor for the use of SERS as a routine analytical tool. Therefore, techniques using

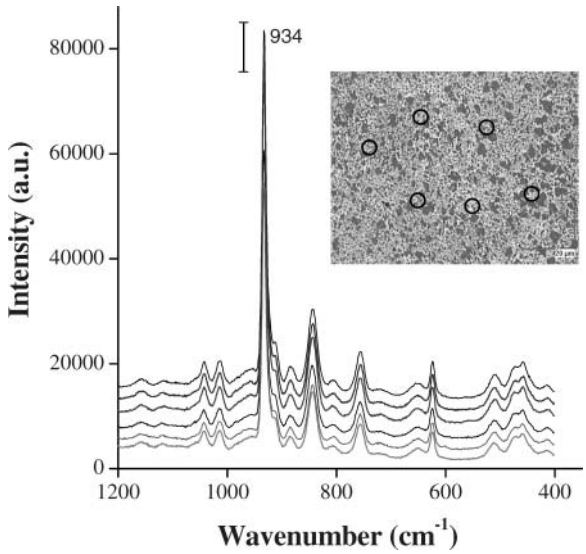

FIG. 2. SERS spectra of ClO_4^- (1×10^{-5} M) obtained from six randomly selected spots (inset) on a substrate made of DMAE-modified Au nanoparticles. Each spectrum was offset for clarity, and the error bar represents a standard deviation of about 16% at peak position 934 cm^{-1}.

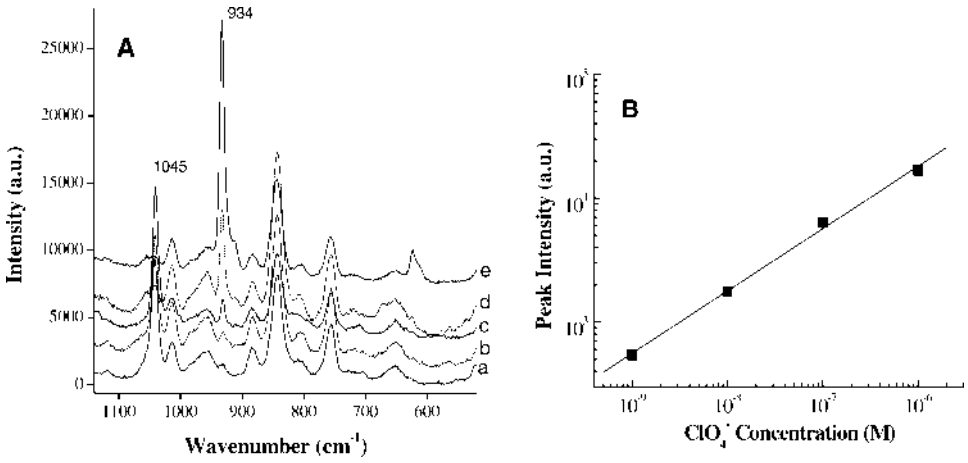

FIG. 3. (**A**) SERS spectroscopic analysis of ClO_4^- in the presence of background electrolytes of SO_4^{2-}, PO_4^{3-}, and NO_3^- at 10^{-4} M each, and Cl^- at 10^{-3} M. Perchlorate concentrations varied from (***a***) 0, (***b***) 10^{-9}, (***c***) 10^{-8}, (***d***) 10^{-7}, to (***e***) 10^{-6} M. (**B**) A log-log plot of the peak intensity at 934 cm^{-1} against the ClO_4^- concentration.

surface modified Au nanoparticles as SERS substrates offer clear advantages here for detecting ClO_4^- with improved sensitivity and reproducibility.[29,30]

Analysis of Perchlorate in Contaminated Samples. To assess the potential interferences in the quantitative analysis of ClO_4^- in realistic contaminated water samples, we further examined the detection of ClO_4^- in the presence of orders of magnitude higher concentrations of background electrolytes including SO_4^{2-}, PO_4^{3-}, and NO_3^-, each at 10^{-4} M, and Cl^- at 10^{-3} M. The resulting SERS spectra are shown in Fig. 3A at perchlorate concentrations of 10^{-6} to 10^{-9} M. In comparison with those shown in Fig. 1A, the general features of the spectra remain unchanged with the exception of the band at 1045 cm^{-1} (Fig. 3A), which was assigned to the stretching vibration of the NO_3^- ion. However, we note that the peak intensity at 1045 cm^{-1} decreased considerably with increasing concentrations of ClO_4^- in solution, especially at concentrations of 10^{-7} and 10^{-6} M. These observations suggest possible competitive interactions between ClO_4^- and NO_3^- ions for sorption onto the Au nanoparticle substrate. The fact that the nitrate band at 1045 cm^{-1} was substantially suppressed could be attributed to the preferential sorption of ClO_4^- ions because of limited sorption sites on DMAE-modified Au nanoparticles. Similar observations have been reported when cystamine-modified gold nanoparticles were used for the detection of ClO_4^- and NO_3^-.[27]

Although SO_4^{2-} and PO_4^{3-} show vibrational bands at about 980 and 925 cm^{-1}, respectively,[39] their Raman scattering apparently was not enhanced by using DMAE-modified Au nanoparticles as a SERS substrate and thus did not significantly interfere with the detection of ClO_4^- ions (Fig. 3). These results suggest that the SERS substrate enhanced the Raman scattering only for some selected anionic species, although exact mechanisms by which the Raman scattering of different ions or molecules is selectively enhanced remain a subject of intensive investigation.[21–24,27,39] One possible explanation is that SO_4^{2-} and PO_4^{3-} ions are only weakly sorbed on the SERS substrate because of their relatively high hydration energy as compared with that of the ClO_4^- ion.[3] However, we note that the presence of these background ionic species did cause overall decreased peak intensities at 934 cm^{-1} for perchlorate. For example, at the ClO_4^- concentration of 10^{-6} M, its peak intensity decreased about 35% as compared with that measured in deionized water (Fig. 1A). Such a decrease in peak intensities of ClO_4^- can be expected because of the presence of 2 to 5 orders of magnitude higher concentrations of background ionic species (NO_3^-, SO_4^{2-}, PO_4^{3-}, Cl^-), which may compete for interactions with the SERS substrate and thus reduce the scattering signal of perchlorate. On the other hand, the presence of these background electrolytes did not appear to impact the quantitative analysis of perchlorate, and a plot of the peak intensity (at 934 cm^{-1}) and the ClO_4^- concentration yielded a linear relationship on a log scale (Fig. 3B). These results again indicate that the DMAE-modified Au SERS substrates could be used for quantitative or semi-quantitative analysis of ClO_4^- in aqueous media. The technique has the potential to be used as a rapid screening tool for environmental analysis because portable Raman spectrometers are readily available and relatively inexpensive.

We further analyzed two contaminated groundwater samples obtained from a field site in Northern California. The groundwater GW-1 contained a ClO_4^- concentration of 8.3×10^{-6} M, which is about three orders of magnitude lower than the concentration of competing ions listed in Table I. The other sample (GW-2) had a ClO_4^- concentration of 1×10^{-8} M, which is five to six orders of magnitude lower than the concentration of competing ions in the water. These samples were analyzed as is or diluted 10 times with deionized water, and the results are shown in Fig. 4. Using Fig. 3B as the standard calibration curve, the calculated ClO_4^- concentrations were 7.86×10^{-6} and 1.02×10^{-8} M for undiluted GW-1 and GW-2 samples, respectively.

These data are in good agreement with those obtained using ion chromatography, which were 8.3×10^{-6} and 1×10^{-8} M (Table I). However, for 10× diluted samples, the SERS analysis substantially overestimated the ClO_4^- concentrations, which were 3.43×10^{-5} and 1.15×10^{-8} M for the GW-1 and GW-2 samples. These observations are not surprising because the background electrolyte concentrations in diluted samples were substantially lower than those used in the calibration "standards" (Fig. 3B). As a result, an increased SERS signal was observed for ClO_4^- because of fewer matrix interferences in the diluted samples. However, by using the calibration curve in Fig. 1B (in deionized water), the calculated ClO_4^-

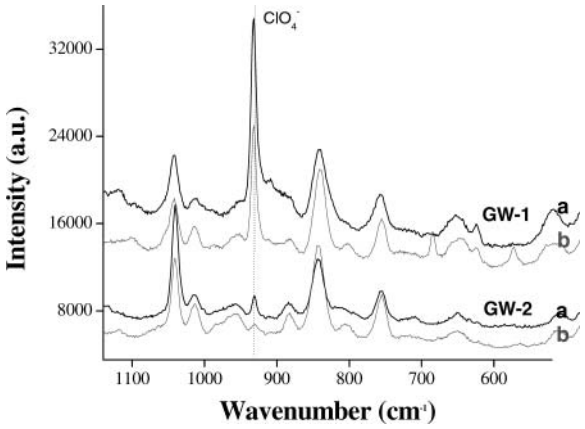

FIG. 4. SERS spectra of two contaminated groundwater samples (GW-1 and GW-2) (***a***) without dilution or (***b***) with a 10× dilution. The ClO_4^- concentrations in undiluted GW-1 and GW-2 were 8.3×10^{-6} and 1×10^{-8} M (Table I).

concentration in GW-1 was 1.08×10^{-5} M, which is close to its true value measured using ion chromatography.

These results thus emphasize the need to prepare samples and reference standards in the same or similar matrices, as a common practice used in any quantitative analysis. For practical applications, future studies and validation will be needed in order to cover a wide variety of environmental conditions for perchlorate detection; standard addition techniques may be used to correct matrix interferences and thus to ensure good reproducibility in quantitative analysis.

ACKNOWLEDGMENTS

This research was supported in part by the Strategic Environmental Research and Development Program (SERDP) of the U.S. Department of Defense and the Laboratory Directed Research and Development Program of the Oak Ridge National Laboratory, which is managed by UT-Battelle, LLC for the U.S. Department of Energy under contract DE-AC05-00OR22725.

1. P. Damian and F. W. Pontius, Environ. Prot., 24 (1999).
2. E. T. Urbansky, B. Gu, M. L. Magnuson, G. M. Brown, and C. A. Kelty, J. Sci. Food Agric. **80,** 1798 (2000).
3. B. Gu and J. D. Coates, *Perchlorate Environmental Occurrence, Interactions and Treatment* (Springer, New York, 2006).
4. B. C. Blount, L. Valentin-Blasini, J. D. Osterloh, J. P. Mauldin, and J. L. Pirkle, J. Exp. Sci. Environ. Epidemiol. **17,** 400 (2007).
5. W. A. Jackson, P. Joseph, P. Laxman, K. Tan, P. N. Smith, L. Yu, and T. A. Anderson, J. Agric. Food Chem. **53,** 369 (2005).
6. A. B. Kirk, P. K. Martinelango, K. Tian, A. Dutta, E. E. Smith, and P. K. Dasgupta, Environ. Sci. Technol. **39,** 2011 (2005).
7. C. A. Sanchez, K. S. Crump, R. I. Krieger, N. R. Khandaker, and J. P. Gibbs, Environ. Sci. Technol. **39,** 9391 (2005).
8. L. Valentin-Blasini, J. P. Mauldin, D. Maple, and B. C. Blount, Anal. Chem. **77,** 2475 (2005).
9. W. Bao and B. Gu, Environ. Sci. Technol. **38,** 5073 (2004).
10. J. K. Böhlke, N. C. Sturchio, B. Gu, J. Horita, G. M. Brown, W. A. Jackson, and J. R. Batista, Anal. Chem. **77,** 7838 (2005).
11. N. C. Sturchio, J. K. Bohlke, A. D. Beloso, S. H. Streger, L. J. Heraty, and P. B. Hatzinger, Environ. Sci. Technol. **41,** 2796 (2007).
12. W. A. Jackson, S. K. Anandam, T. Anderson, T. Lehman, K. Rainwater, S. Rajagopalan, M. Ridley, and R. Tock, Ground Water Monitoring Remediation **25,** 137 (2005).
13. P. K. DasGupta, J. V. Dyke, A. B. Kirk, and W. A. Jackson, Environ. Sci. Technol. **40,** 6608 (2006).
14. P. K. Dasgupta, P. K. Martinelango, W. A. Jackson, T. A. Anderson, K. Tian, R. W. Tock, and S. Rajagopalan, Environ. Sci. Technol. **39,** 1569 (2005).
15. E. T. Urbansky, Bioremed. J. **2,** 81 (1998).
16. P. E. Jackson, S. Gokhale, T. Streib, J. S. Rohrer, and C. A. Pohl, J. Chromatogr. A **888,** 151 (2000).
17. E. T. Urbansky, Crit. Rev. Anal. Chem. **30,** 311 (2000).
18. R. Perez-Olmos, A. Rios, M. P. Martin, R. A. S. Lapa, and J. L. F. C. Lima, Analyst (Cambridge, U.K.) **124,** 97 (1999).
19. C. Sanchez-Pedreno, J. A. Ortuno, and J. Hernandez, Anal. Chim. Acta **415,** 159 (2000).
20. S. W. Park, K. H. Jin, J. H. You, T. J. Kim, K. J. Paeng, and K. H. Kong, Anal. Sci. **13,** 243 (1997).
21. K. Zhao, H. Xu, B. Gu, and Z. Zhang, J. Chem. Phys. **125,** 081102 (2006).
22. S. Nie and S. R. Emory, Science (Washington, D.C.) **275,** 1102 (1997).
23. K. Kneipp, H. Kneipp, I. Itzkan, R. R. Dasari, and M. S. Feld, Chem. Rev. **87,** 2957 (1999).
24. C. M. Ruan, W. Wang, and B. Gu, J. Raman Spectrosc. **38,** 568 (2007).
25. P. A. Mosier-Boss and S. H. Lieberman, Appl. Spectrosc. **57,** 1129 (2003).
26. B. Gu, J. Tio, W. Wang, Y. Ku, and S. Dai, Appl. Spectrosc. **58,** 741 (2004).
27. C. M. Ruan, W. Wang, and B. Gu, Anal. Chim. Acta **567,** 114 (2006).
28. W. Wang, C. M. Ruan, and B. Gu, Anal. Chim. Acta **567,** 121 (2006).
29. S. Tan, M. Erol, A. Attygalle, H. Du, and S. Sukhishvili, Langmuir **23,** 9836 (2007).
30. B. Gu and C. Ruan, Anal. Chem. **79,** 2341 (2007).
31. C. M. Ruan, W. Wang, and B. Gu, Anal. Chim. Acta **605,** 80 (2007).
32. W. Wang and B. Gu, Appl. Spectrosc. **59,** 1509 (2005).
33. M. Sackmann and A. Materny, J. Raman Spectrosc. **37,** 305 (2006).
34. L. G. Olson, Y. S. Lo, T. P. Beebe, and J. M. Harris, Anal. Chem. **73,** 4268 (2001).
35. C. S. Weisbecker, M. V. Merritt, and G. M. Whitesides, Langmuir **12,** 3763 (1996).
36. Z. Y. Zhong, S. Patskovskyy, P. Bouvrette, J. H. T. Luong, and A. Gedanken, J. Phys. Chem. B **108,** 4046 (2004).
37. B. Gu, G. M. Brown, and C. C. Chiang, Environ. Sci. Technol. **41,** 6277 (2007).
38. H. Xu, J. Aizpura, M. Kall, and P. Apell, Phys. Rev. E **62,** 4318 (2000).
39. G. Niaura and R. Jakubenas, J. Electroanal. Chem. **510,** 50 (2001).

NANO LETTERS

pubs.acs.org/NanoLett

Free-Standing Optical Gold Bowtie Nanoantenna with Variable Gap Size for Enhanced Raman Spectroscopy

Nahla A. Hatab,[†] Chun-Hway Hsueh,[‡,||,⊥] Abigail L. Gaddis,[‡] Scott T. Retterer,[§] Jia-Han Li,[¶] Gyula Eres,[‡] Zhenyu Zhang,[*,‡,||] and Baohua Gu[*,†]

[†]Environmental Sciences, [‡]Materials Science and Technology Divisions, and [§]Center for Nanophase Materials Sciences, Oak Ridge National Laboratory, Oak Ridge, Tennessee 37831, United States, [||]Department of Physics and Astronomy, University of Tennessee, Knoxville, Tennessee 37996, United States, and [⊥]Department of Materials Science and Engineering and [¶]Department of Engineering Science and Ocean Engineering, National Taiwan University, Taipei 106, Taiwan

ABSTRACT We describe plasmonic interactions in suspended gold bowtie nanoantenna leading to strong electromagnetic field (*E*) enhancements. Surface-enhanced Raman scattering (SERS) was used to demonstrate the performance of the nanoantenna. In addition to the well-known gap size dependence, up to 2 orders of magnitude additional enhancement is observed with elevated bowties. The overall behavior is described by a SERS enhancement factor exceeding 10^{11} along with an anomalously weak power law dependence of *E* on the gap size in a range from 8 to 50 nm that is attributed to a plasmonic nanocavity effect occurring when the plasmonic interactions enter a strongly coupled regime.

KEYWORDS Electron beam lithography, FDTD simulation, optical nanoantenna, single molecule SERS, collective photonic effect

It is now widely recognized that the extreme sensitivity of SERS is dominated by the electromagnetic enhancement, referring to the intense, spatially varying *E* fields produced by plasmonic coupling between closely spaced metal nanoparticles.[1−15] A particularly intriguing feature of the electromagnetic enhancement is associated with the presence of the so-called "nanogap" effect where local SERS enhancement factors (EF) sufficient for detection of single molecules have been observed.[1,2] Theoretical analysis using model systems consisting of closely spaced metal nanostructures have identified the size, shape, gap distance, the wavelength and polarization of the incident light as key factors that govern the overall EF within the nanogap.[1−5,16−18] These advances in understanding the nanogap effect motivated new experimental approaches that, instead of searching for isolated hot spots or nanogaps in random nanoparticle aggregates,[19,20] use electron beam lithography (EBL) fabricated periodic nanostructures.[3,5,21] EBL is the ideal tool for fabricating SERS substrates with precisely defined shape and systematically variable nanogap size necessary for gaining insight into the underlying enhancement mechanisms and for achieving maximal enhancement. Recent compelling examples include the demonstration of a strong polarization and gap size dependent response from single gold nanobowties fabricated by EBL,[3,7] and the high-harmonic generation by resonant plasmon field enhancement from a closely packed gold bowtie arrays.[22] However, the large enhancement factors expected to occur for gap sizes on the order of a few nanometers remain difficult to confirm[3−5,7,23] primarily because the resolution necessary for generating such features is beyond the capabilities of conventional EBL.[3,7,15] Overcoming these technical hurdles promises advances in fundamental understanding of gap-dependent *E* field coupling that enable design and fabrication of a new generation of nanostructures that are capable of reliably and reproducibly performing single molecule detection and spectroscopy, and advanced optoelectronic functionality.[5,14,15]

Here we demonstrate large SERS enhancement factors exceeding 10^{11} resulting from a new configuration of elevated gold bowtie nanoanatenna arrays with optimized array periodicity. Figure 1a shows a schematic illustration of these structures, together with a scanning electron microscope (SEM) image of the actual structures in Figure 1b, and the spatial distribution of the *E* field intensity calculated by finite difference time domain (FDTD) simulations shown in Figure 1c. A process combining nanofabrication steps of pattern definition by EBL, metal deposition, liftoff, and reactive ion etching (RIE) arranged in a particular sequence was used to fabricate the elevated gold bowtie arrays on Si wafers according to details given in Supporting Information. A precisely controlled deposition of 40 nm gold on a Cr adhesion layer located on top of 200 nm tall Si posts was used to close the 20 nm gap size defined by EBL to 8 ± 1 nm. This step also produces the characteristic overhang that

* To whom correspondence should be addressed. E-mail: (B.G.) gub1@ornl.gov; (Z.Z.) zhangz@ornl.gov.

Received for review: 08/21/2010
Published on Web: 11/19/2010

DOI: 10.1021/nl102963g | *Nano Lett.* **2010,** *10,* 4952–4955

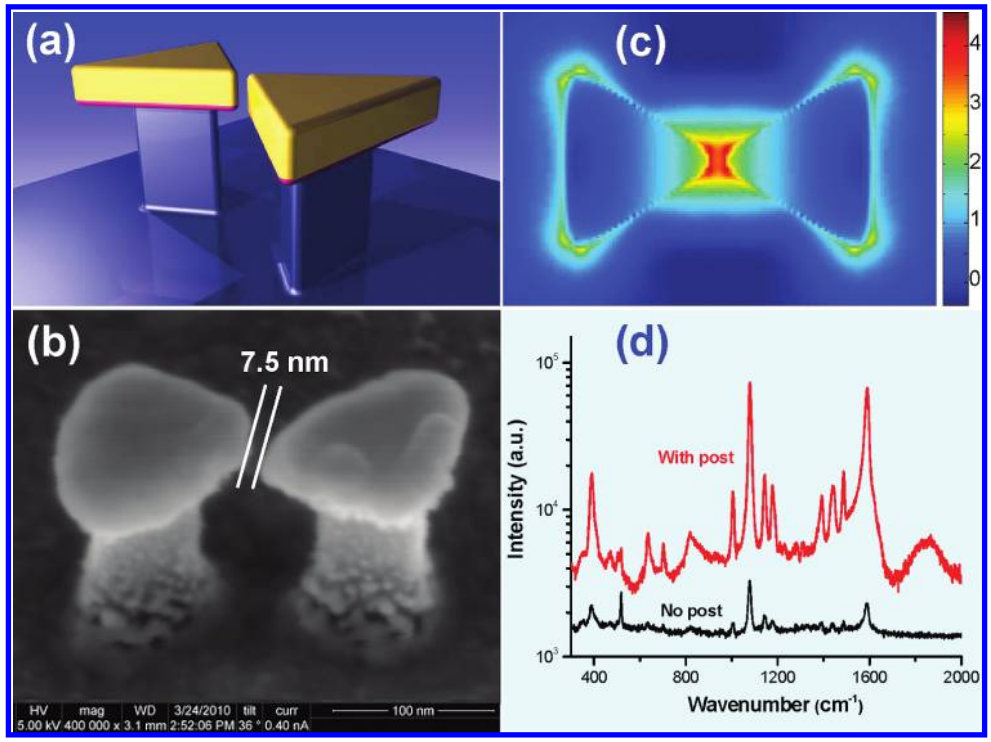

FIGURE 1. (a) Schematic illustration of elevated gold bowties on top of Si posts etched into a Si wafer with a magenta colored Cr adhesion layer between the gold layer and the Si post. (b) Side view SEM image of a three-dimensional gold bowtie nanoantenna with a gap of 8 ± 1 nm. (c) The spatial distribution of the *E* field intensity calculated by FDTD simulations for bowtie equilateral triangle sides of 100 nm, gap size of 10 nm, Si posts of 40 nm in diameter and 200 nm in height, and an apex width of 10 nm (see Supporting Information Figure S3). The intensity is given by a logarithmic scale color bar. (d) Comparison of SERS spectra of *p*-mercaptoaniline from elevated and nonelevated bowtie array substrates.

along with the post defines the three-dimensional nanoantenna (Figure 1b) and distinguishes these structures from gold bowties that remain attached to the substrate.[3,7,21,22] The contrast in SEM backscattered electron images (Supporting Information Figure S1) shows that only the bowties and not the posts are coated with gold. A comparison of SERS spectra of elevated bowties with that of bowties attached to the substrate is shown in Figure 1d. The elevated bowties allow manifestation of intrinsic plasmonic coupling effects in suspended nanocavities, or the tip-to-tip nanogaps, from structures that are not in physical contact with a substrate. This configuration results in up to 2 orders of magnitude additional enhancement in SERS response compared to that of nonelevated bowtie arrays (Figure 1d). The influence of the post heights on the SERS response is confirmed by and qualitatively agrees with FDTD simulation results illustrated in Supporting Information Figure S4. Experimental studies of SERS dependence on the post height are the subject of ongoing work and will be described in a future publication.

Different density arrays shown in Figure 2a were fabricated by changing the center-to-center distance (ccd) in rows along the bowtie axis, and the row-to-row distance (rrd). The isolated bowtie arrays shown in image II of Figure 2a have a dimension of ccd = rrd = 2 μm that is close to the laser spot size, which ensures that the SERS measurements represent local response from a single bowtie. We next compare the SERS response of isolated bowties with that from high-density (III) and low-density (I) arrays in Figure 2a with specific periodicity of ccd = rrd = 300 nm, and ccd = 785 nm, rrd = 2 μm, respectively. The Raman EF for these arrays shown in Figure 2b was determined from the SERS intensity of a probing molecule, *p*-mercaptoaniline (*p*MA).[6,24] Exposure of the bowties to a *p*MA solution (10^{-5} M) results in the chemisorption and uniform coating of the gold surface by a monolayer of *p*MA molecules that ensures unambiguous determination of the SERS enhancement and good reproducibility (Supporting Information Figure S2). The EF was determined following a procedure established in the literature[3,6,24−26] and is described in Supporting Information. Here the EF represents the ratio of the SERS signal to the nonenhanced bulk Raman signal measured and normalized per molecule for the 1588 cm^{-1} Raman band.

For all arrays, the EF increases with decreasing gap size and reaches 2 × 10^{11} and 7 × 10^{11} at the smallest gap of 8 ± 1 nm for the isolated and low-density bowtie arrays (Figure 2b). These values match the largest enhancements reported for nanoshells and nanoparticle aggregates that typically contain a number of randomly distributed hot spots.[6,19,20,24] In addition to the distinct gap size dependence that dominates the response of isolated bowties, we demonstrate that the bowtie arrays are also subject to collective interactions that either degrade or further enhance the overall SERS response. The trends in Figure 2b identify the

DOI: 10.1021/nl102963g | *Nano Lett.* **2010,** *10,* 4952–4955

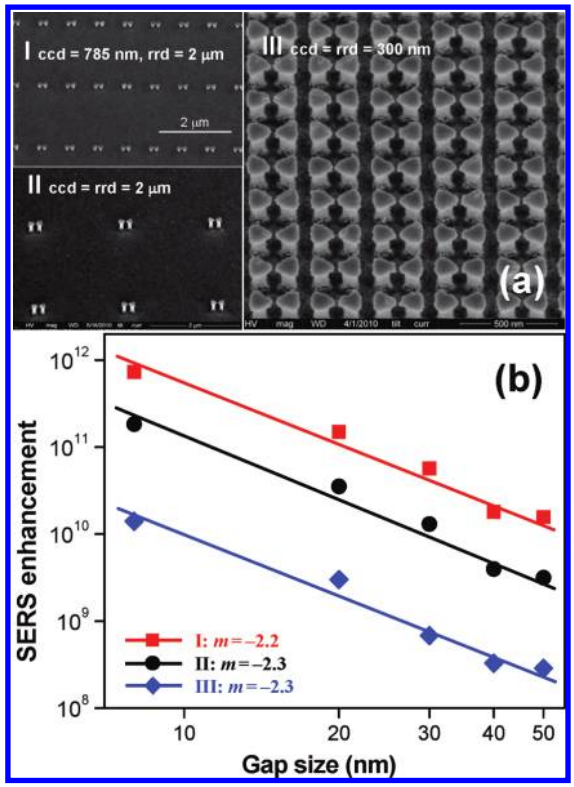

FIGURE 2. Determination of the gap size dependence and the long-range collective plasmonic effects in SERS enhancement using elevated gold bowtie nanoantenna arrays. (a) SEM images of the elevated gold bowtie arrays with varying center-to-center distance in rows along the bowtie axis, and row-to-row distance. (b) A log−log plot of SERS enhancement factors as a function of bowtie nanogap size in arrays I, II, and III with different bowtie spacing. The slope is determined by fitting the power-law relationship of EF ∝ Ad^m to the experimental data.

array periodicity as the critical factor that determines the EF change. The maximal enhancement is achieved when the periodicity of the arrays matches the laser wavelength. In particular, we note that the EF from the high-density bowtie array with ccd = rrd = 300 nm (III in Figure 2) was about 1 order of magnitude lower than that for the isolated bowties. In contrast, the low-density arrays with optimized periodicity of ccd = 785 nm (I in Figure 2) that matches the Raman laser wavelength, produced an EF with nearly an order of magnitude additional increase above that for isolated bowties. These observations represent the first definitive experimental confirmation of the theoretically predicted long-range collective photonic effect.[16,17,27] This important finding suggests that even greater enhancements might have been realized in previous experiments[12,22] had the bowtie or nanoparticle arrays been more sparsely distributed.

The FDTD simulations identify the shape and sharpness (w) of the triangle's apex (Supporting Information Figure S3) as factors that affect efficient coupling of the incident optical radiation into the bowtie gap. The spatial distribution plot of the E field intensity in Figure 1c shows that for elevated bowties the nanogap effect is strongly localized in the volume between the tips of the triangles. In addition, Figure 3 illustrates that the nanogap effect and the resulting SERS response become stronger with the apex sharpness (w) increasing from 20 to 1 nm.

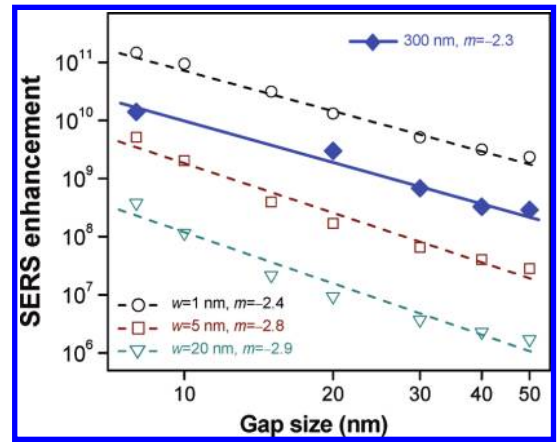

FIGURE 3. Comparison of the FDTD calculated maximum field $|E|^4$ enhancement (dashed lines with open symbols) for apex widths w = 1, 5, and 20 nm with the experimentally determined SERS enhancement (solid line with solid diamonds) as a function of nanogap size for elevated bowtie arrays with ccd = rrd = 300 nm (III in Figure 2). The slope is determined by fitting the power-law relationship of EF ∝ $|E|^4 = Ad^m$ to the data.

The elevated gold bowtie arrays reveal another important feature of the EF. A log−log plot of the EF against the gap size, d, gives a straight line with a slope (m) near -2.2 ± 0.1 for the bowtie arrays (Figure 2b). Similar magnitude and slope are obtained using FDTD simulations for the high-density bowtie arrays with apex width near 1 nm (Figure 3). On the basis of the general relationship of the EF ∝ $|E|^4 = Ad^m$, this behavior is equivalent to a weak power law dependence of E on the gap size given by $E \sim d^{-0.56}$, that is even weaker than the decay of a monopole field according to Coulomb's law of $E \sim d^{-2}$. These findings suggest that narrowing the gap separation between the two prisms below ~50 nm the bowties enter into a regime characterized by exceptionally strong E field within the gap region. In this strongly coupled regime, the E field shows little attenuation possibly due to resonant nanocavity effects[28] supported by both experimental observations and the FDTD simulation (Supporting Information Figure S5). However, the weak power law dependence may also include a component resulting from red shifting of the plasmon resonant frequency with decreasing gap size.[17,29,30] According to the plasmon ruler equation[31,32] the plasmon wavelength shift reaches maximum for very small gap sizes and decays exponentially with the gap size. Nevertheless, an important technological significance of this weak attenuation comes with the realization that in the strong coupling regime the arrays can tolerate a certain degree of gap size nonuniformity and geometrical imperfection without losing their ability for large field enhancement. The spatial localization of a free-standing, finite plasmonic volume enabled by the three-dimensional suspended bowtie nanoantenna substantially expands the versatility of utilizing E-field enhancement

DOI: 10.1021/nl102963g | Nano Lett. 2010, 10, 4952–4955

that has numerous applications in chemistry and physics including single molecule spectroscopy, and a variety of advanced optical characterization, manipulation, and optical information processing using periodic metallic nanostructures.

Acknowledgment. We thank C.M. Rouleau for his contribution to the art work in this paper. This work was supported by the Strategic Environmental Research and Development Program (SERDP) of the U.S. Department of Defense (N.A.H. and B.G.), the Materials Sciences and Engineering Division, Office of Basic Energy Sciences, U.S. Department of Energy (DOE) (A.L.G., G.E., and Z.Z), and the National Science Council of Taiwan (C.H. and J.L.). The fabrication of the gold bowtie nanoantenna was conducted at the Center for Nanophase Materials Sciences of Oak Ridge National Laboratory (ORNL), which is sponsored by DOE Scientific User Facilities Division (S.T.R.). ORNL is managed by UT-Battelle, LLC, for U.S. DOE under contract DE-AC05-00OR22725.

Supporting Information Available. Fabrication of elevated gold bowtie arrays on silicon wafers, sample characterization and Raman spectroscopic analysis, determination of SERS enhancement factors, FDTD computational algorithm and model simulations, additional figures, and additional references. This material is available free of charge via the Internet at http://pubs.acs.org.

REFERENCES AND NOTES

(1) Xu, H.; Bjerneld, E. J.; Kall, M.; Borjesson, L. *Phys. Rev. Let.* **1999**, *83*, 4357–4360.
(2) Michaels, A. M.; Jiang, J.; Brus, L. *J. Phys. Chem. B* **2000**, *104* (50), 11965–11971.
(3) Fromm, D. P.; Sundaramurthy, A.; Schuck, P. J.; Kino, G.; Moerner, W. E. *Nano Lett.* **2004**, *4* (5), 957–961.
(4) Wang, H.; Levin, C. S.; Halas, N. J. *J. Am. Chem. Soc.* **2005**, *127* (43), 14992–14993.
(5) Qin, L. D.; Zou, S. L.; Xue, C.; Atkinson, A.; Schatz, G. C.; Mirkin, C. A. *Proc. Natl. Acad. Sci. U.S.A.* **2006**, *103* (36), 13300–13303.
(6) Haynes, C. L.; Van Duyne, R. P. *J. Phys. Chem. B* **2003**, *107* (30), 7426–7433.
(7) Fromm, D. P.; Sundaramurthy, A.; Kinkhabwala, A.; Schuck, P. J.; Kino, G. S.; Moerner, W. E. *J. Chem. Phys.* **2006**, *124* (6), No. 061101.
(8) Dieringer, J. A.; Lettan, R. B.; Scheidt, K. A.; Van Duyne, R. P. *J. Am. Chem. Soc.* **2007**, *129* (51), 16249–16256.
(9) Etchegoin, P. G.; Le Ru, E. C. *Phys. Chem. Chem. Phys.* **2008**, *10* (40), 6079–6089.
(10) Camden, J. P.; Dieringer, J. A.; Wang, Y. M.; Masiello, D. J.; Marks, L. D.; Schatz, G. C.; Van Duyne, R. P. *J. Am. Chem. Soc.* **2008**, *130* (38), 12616.
(11) Qian, X. M.; Nie, S. M. *Chem. Soc. Rev.* **2008**, *37* (5), 912–920.
(12) Fang, Y.; Seong, N. H.; Dlott, D. D. *Science* **2008**, *321* (5887), 388–392.
(13) Li, J. F.; Huang, Y. F.; Ding, Y.; Yang, Z. L.; Li, S. B.; Zhou, X. S.; Fan, F. R.; Zhang, W.; Zhou, Z. Y.; Wu, D. Y.; Ren, B.; Wang, Z. L.; Tian, Z. Q. *Nature* **2010**, *464* (7287), 392–395.
(14) Lim, D. K.; Jeon, K. S.; Kim, H. M.; Nam, J. M.; Suh, Y. D. *Nat. Mater.* **2010**, *9* (1), 60–67.
(15) Theiss, J.; Pavaskar, P.; Echternach, P. M.; Muller, R. E.; Cronin, S. B. *Nano Lett.* **2010**, *10*, 2749–2754.
(16) Zou, S. L.; Schatz, G. C. *Chem. Phys. Lett.* **2005**, *403* (1−3), 62–67.
(17) Zhao, K.; Xu, H.; Gu, B.; Zhang, Z. *J. Chem. Phys.* **2006**, *125*, No. 081102.
(18) Tabor, C.; Murali, R.; Mahmoud, M.; El-Sayed, M. A. *J. Phys. Chem. A* **2009**, *113* (10), 1946–1953.
(19) Kneipp, K.; Wang, Y.; Kneipp, H.; Perelman, L. T.; Itzkan, I.; Dasari, R.; Feld, M. S. *Phys. Rev. Lett.* **1997**, *78* (9), 1667–1670.
(20) Nie, S.; Emory, S. R. *Science* **1997**, *275*, 1102–1106.
(21) Kinkhabwala, A.; Yu, Z. F.; Fan, S. H.; Avlasevich, Y.; Mullen, K.; Moerner, W. E. *Nat. Photonics* **2009**, *3* (11), 654–657.
(22) Kim, S.; Jin, J. H.; Kim, Y. J.; Park, I. Y.; Kim, Y.; Kim, S. W. *Nature* **2008**, *453*, 757–760.
(23) Hinde, R. J.; Sepaniak, M. J.; Compton, R. N.; Nordling, J.; Lavrik, N. *Chem. Phys. Lett.* **2001**, *339* (3−4), 167–173.
(24) Jackson, J. B.; Halas, N. J. *Proc. Natl. Acad. Sci. U.S.A.* **2004**, *101* (52), 17930–17935.
(25) Hu, X. G.; Wang, T.; Wang, L.; Dong, S. J. *J. Phys. Chem. C* **2007**, *111* (19), 6962–6969.
(26) Wells, S. M.; Retterer, S. D.; Oran, J. M.; Sepaniak, M. *J. ACS Nano* **2009**, *3* (12), 3845–3853.
(27) Haynes, C. L.; McFarland, A. D.; Zhao, L. L.; Van Duyne, R. P.; Schatz, G. C.; Gunnarsson, L.; Prikulis, J.; Kasemo, B.; Kall, M. *J. Phys. Chem. B* **2003**, *107* (30), 7337–7342.
(28) Dong, Z. C.; Zhang, X. L.; Gao, H. Y.; Luo, Y.; Zhang, C.; Chen, L. G.; Zhang, R.; Tao, X.; Zhang, Y.; Yang, J. L.; Hou, J. G. *Nat. Photonics* **2010**, *4* (1), 50–54.
(29) Sundaramurthy, A.; Crozier, K. B.; Kino, G. S.; Fromm, D. P.; Schuck, P. J.; Moerner, W. E. *Phys. Rev. B* **2005**, *72* (16), 1098–0121.
(30) Zhao, L. L.; Kelly, K. L.; Schatz, G. C. *J. Phys. Chem. B* **2003**, *107* (30), 7343–7350.
(31) Jain, P. K.; Huang, W. Y.; El-Sayed, M. A. *Nano Lett.* **2007**, *7* (7), 2080–2088.
(32) Zuloaga, J.; Prodan, E.; Nordlander, P. *Nano Lett.* **2009**, *9* (2), 887–891.

DOI: 10.1021/nl102963g | *Nano Lett.* **2010,** *10,* 4952–4955

Research Article

Journal of RAMAN SPECTROSCOPY

Received: 2 October 2009 Accepted: 21 October 2009 Published online in Wiley Online Library: 5 January 2010

(wileyonlinelibrary.com) DOI 10.1002/jrs.2574

Detection and analysis of cyclotrimethylenetrinitramine (RDX) in environmental samples by surface-enhanced Raman spectroscopy

Nahla A. Hatab,[a]* Gyula Eres,[b] Paul B. Hatzinger[c] and Baohua Gu[a]*

Techniques for rapid and sensitive detection of energetics such as cyclotrimethylenetrinitramine (RDX) are needed both for environmental and security screening applications. Here we report the use of surface-enhanced Raman scattering (SERS) spectroscopy to detect traces of RDX with good sensitivity and reproducibility. Using gold (Au) nanoparticles (~90–100 nm in diameter) as SERS substrates, RDX was detectable at concentrations as low as 0.15 mg/l in a contaminated groundwater sample. This detection limit is about two orders of magnitude lower than those reported previously using SERS techniques. A surface enhancement factor of ~6×10^4 was obtained. This research further demonstrates the potential for using SERS as a rapid, *in situ* field screening tool for energetics detection when coupled with a portable Raman spectrometer.

Keywords: RDX; explosives; SERS detection; gold nanoparticles; groundwater

Introduction

The real-time detection of explosive compounds for environmental monitoring and security screening is a rapidly evolving field and is important for both environmental safety and national security. Cyclotrimethylenetrinitramine (RDX) is one of the most commonly used explosives, and it is frequently detected in soils and groundwater at or near military installations because of its long persistence and high mobility.[1–5] For example, the U.S. Army is reported to have 583 sites at 82 installations with explosives in groundwater and 87 additional locations with suspected groundwater contamination.[5] In addition, studies have shown that munition compounds on ranges and other military testing sites are often heterogeneously distributed in surface soils, with RDX concentrations ranging from less than 0.5 mg/kg up to 10 000 mg/kg for samples collected only a few feet from each other.[1,2] Currently, the detection and analysis of RDX is conducted primarily via high-performance liquid chromatography (HPLC) (USEPA Method 8330), which requires expensive capital equipment and significant costs for sample collection and shipping as well as for laboratory extraction and analysis. Moreover, typical turnaround times for explosives analysis by commercial laboratories are 2 weeks or longer. Rapid, *in situ* field detection and screening technologies are therefore desirable to perform cost-effective assessments within military testing and training ranges to identify potential areas of groundwater contamination with explosives such as RDX.

Surface-enhanced Raman scattering (SERS) spectroscopy has the potential to serve as a rapid screening tool for detecting many different chemical and biological agents. For example, SERS has been demonstrated to be a useful technique for the identification of explosives,[6–10] chemical warfare agents,[11,12] and bacteria.[13–15] The vibrational spectrum generated using this technique provides a 'fingerprint' of the chemical composition of each agent. In addition, SERS is often more sensitive than traditional Raman spectroscopy because the vibrational modes of the analyte can be easily enhanced 10^2–10^9 times when the analyte is adsorbed on noble-metal surfaces. This is due to the high effective SERS cross section per molecule, which allows for detection of up to only a few molecules. Two mechanisms have been known to account for the SERS effect.[16,17] The electromagnetic mechanism is believed to be responsible for the main enhancement that occurs as a result of the excitation of surface plasmons localized on roughened metal surfaces. The second mechanism is related to an increased polarizability of adsorbed molecules due to specific interactions or coupling effects between the metal surface and the adsorbed molecule, although this mechanism has a much smaller contribution to the overall enhancement. Also, the SERS technique requires little or no sample preparation or pretreatment and a small sample volume (usually tens of microliters). Moreover, it is rapid and virtually

* *Correspondence to: Nahla A. Hatab, Environmental Sciences Division, Oak Ridge National Laboratory, Oak Ridge, TN 37831, USA. E-mail: abuhatabna@ornl.gov*

Baohua Gu, Environmental Sciences Division, Oak Ridge National Laboratory, Oak Ridge, TN 37831, USA. E-mail: gub1@ornl.gov

a *Environmental Sciences Division, Oak Ridge National Laboratory, Oak Ridge, TN 37831, USA*

b *Materials Science and Technology Division, Oak Ridge National Laboratory, Oak Ridge, TN 37831, USA*

c *Shaw Environmental, Inc., Lawrenceville, NJ 08648, USA*

nondestructive, and most analytes can be analyzed directly in water. The availability of portable Raman spectrometers also makes it possible to interface it with an SERS probe, permitting rapid, *in situ* field detection and screening.[18] Therefore, the SERS-based methods have the potential to reduce time, operational costs, and waste generated during the analysis while providing discriminative quantification of analytes in a single measurement.

The potential of SERS for trace analysis of explosives has been explored in recent years.[7,8,11,19] In an early study, Kneipp *et al.*[7] reported a minimum detection limit of 10^{-7} M for trinitrotoluene (TNT) adsorbed on gold and silver nanoparticles in laboratory-prepared solutions. More recently, a detection limit of 10^{-12} M for TNT was achieved by using synthesized Ag nanoparticles as SERS substrates and by adjusting the pH of the TNT aqueous solution.[11] SERS was also found to be applicable for detecting the chemical vapor signature emanating from buried TNT-based landmines at a concentration level of 5 μg/l using a flow-through probe head design and electrochemically etched gold substrates.[8] Gold substrates produced by a nanosphere imprinting technique were recently shown to be applicable not only for SERS detection of TNT but also for detection of RDX and cyclotetra-methylene-tetranitramine (HMX) at 4.5×10^{-4} M for both nitramines.[19] While the SERS technique shows great promise for detection of explosives, most of these previous studies were performed in laboratory-prepared solutions rather than in environmental samples. Trace detection by SERS is known to face potential complications from environmental matrixes, which can compromise the performance and accuracy of the analysis. In addition, to the best of our knowledge, there have been no SERS studies to detect RDX in realistic environmental groundwater samples.

In this work, we report on the synthesis and use of Au nanoparticles as sensitive SERS substrates for detecting RDX explosive at concentrations as low as about 1×10^{-6} M in a contaminated groundwater. The substrates were evaluated in terms of both sensitivity and reproducibility for detecting RDX. An SERS enhancement factor of about 6×10^4 was obtained, and the technique was validated by detecting RDX in an environmental sample using the standard addition method.

Experimental

RDX reference standard (1 mg/ml in acetonitrile) was purchased from AccuStandard, Inc. Thionine, $HAuCl_4$, cetyltrimethylammonium bromide (CTAB), trisodium citrate hydrate, and sodium borohydride were obtained from Aldrich. Deionized (DI) water with resistivity higher than 18.2 MΩ·cm (Barnstead E-pure) was used when preparing aqueous solutions. The gold nanoparticles were prepared by a seed-mediated growth approach[20,21] involving the reduction of $HAuCl_4$ with borohydride in the presence of trisodium citrate. Au seeds were first prepared and used to grow larger nanoparticles in the presence of CTAB, additional $HAuCl_4$, and ascorbic acid as a reducing agent. Briefly, 2.0 ml of ice-cold 0.1 M $NaBH_4$ was added to a 40 ml aqueous solution containing 2.5×10^{-3} M $HAuCl_4$ and 2.5×10^{-4} M trisodium citrate with vigorous stirring. The solution immediately turned orange, indicating the formation of gold nanoparticles. Citrate serves as a capping agent in this solution, and the gold seeds were observed to be stable for at least 1 month. Larger gold nanoparticles were subsequently synthesized as follows. A 100-ml vial and four 45-ml vials were labeled '1' through '5'. To each of these vials, 8 ml of 2.5×10^{-3} M $HAuCl_4$ and 0.5 ml 1×10^{-3} M CTAB were added, followed by the addition of 70 μl of 0.10 M of freshly prepared ascorbic acid solution under gentle stirring. The seed solution (3 ml) was then added to sample 1 and, after 1 min, the sample 1 suspension (11.5 ml) was drawn and added to sample 2 with gentle stirring. This procedure was repeated from sample 2 to sample 5, and the ending Au nanoparticle suspension (sample 5) was stored in a refrigerator for 48 h before use. Excess CTAB was removed by centrifugation and washing with DI water three times.

The extinction spectra of as-synthesized Au nanoparticles were recorded using an HP UV-VIS 8453 spectrophotometer (Agilent Technologies) after diluting 5 μl of the Au suspension in 6 ml of DI water. Scanning electron microscopy (SEM) images were obtained using a Hitachi S4800 FEG-SEM scanning electron microscope operated at 4 kV. SERS spectra were obtained using a Renishaw micro-Raman system (Renishaw Inc.) equipped with a 300 mW near-infrared diode laser for excitation at a wavelength of 785 nm. The laser beam was set in position with a 50×, 0.5 NA (numerical aperture) Leica microscope objective at a lateral spatial resolution of ~2 μm. A charge-coupled device array detector was used to achieve signal detection from a 1200 groove/mm grating light path controlled by Renishaw WiRE software and analyzed by ThermoGalactic GRAMS software.

RDX working standard solutions of 10^{-4} to 10^{-7} M were prepared from a stock solution of 8×10^{-4} M by diluting the reference standard in DI water. SERS samples were prepared by mixing 0.5 ml of the Au nanoparticle suspension with 250 μl of RDX standard solutions at different concentrations. This mixed RDX and Au nanoparticle suspension (50 μl) was then placed on a glass slide for SERS analysis after the droplet was air-dried. The calibration curves and the reproducibility studies were performed on the same day to minimize error associated with instrument variability.

To evaluate the applicability of SERS technique to detect RDX in the environment, a contaminated groundwater sample was obtained from a U.S. Navy facility in Virginia and used as received. This sample is characterized with a low pH and contained 18 mg/l of total organic carbon (TOC). Major cations and anions included sulfate (21.5 mg/l), chloride (18.0 mg/l), sodium (39.7 mg/l), magnesium (7.65 mg/l), calcium (19.7 mg/l), and potassium (7.5 mg/l). The analysis was performed by the standard addition method, in which 15 ml of the groundwater sample (with an unknown concentration of RDX) were spiked with 0, 50, 70, 175, or 300 μl of a stock solution of RDX (at 177.7 mg/l). The final volume was made up to 25 ml with DI water. The characteristic Raman band intensity at 874 cm^{-1} for RDX for each sample was plotted against the final added concentration of RDX, and a linear regression routine was used to calculate the absolute value of the X-intercept, which is equal to the concentration of RDX in groundwater.

Results and Discussion

The as-synthesized Au nanoparticles were first characterized for their absorption spectra by UV–vis spectroscopy and for their size and morphology by SEM (Fig. 1(A) and (B)). Both spectra of Au nanoparticles and Au seeds (Fig. 1(A)) showed a broad absorption band which has been referred to as the plasmon resonance absorption band and is ascribed to a collective oscillation of the conduction electrons in response to optical excitation.[22–24] Absorption bands are centered at 528 nm for Au seeds and 635 nm for Au nanoparticles; the position of the plasmon band

Journal of RAMAN SPECTROSCOPY

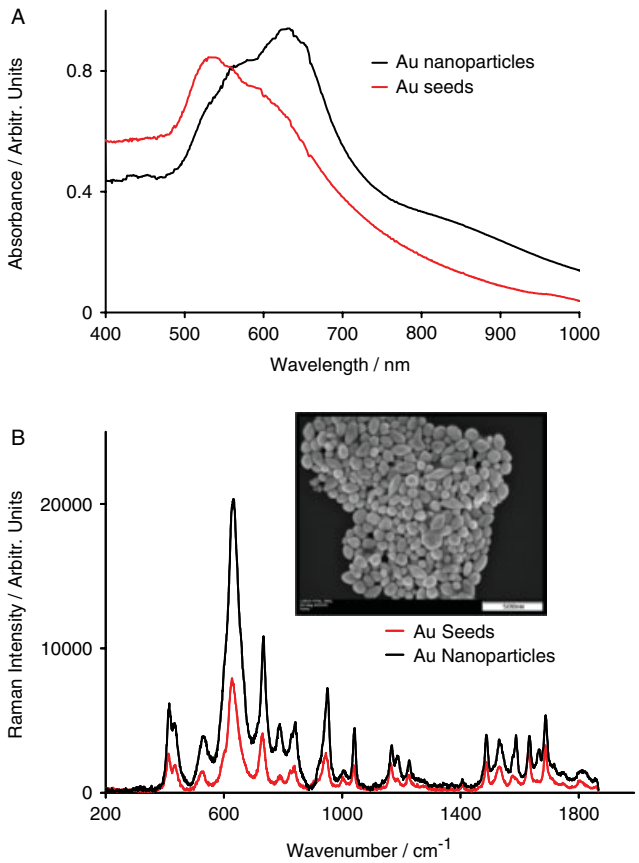

Figure 1. (A) UV-visible spectra of the Au seeds and Au nanoparticles in water. (B) SERS spectra of (1×10^{-6} M thionine) from Au seeds and Au nanoparticles. Inset is a scanning electron micrograph of synthesized Au nanoparticles with an average diameter of 90 nm.

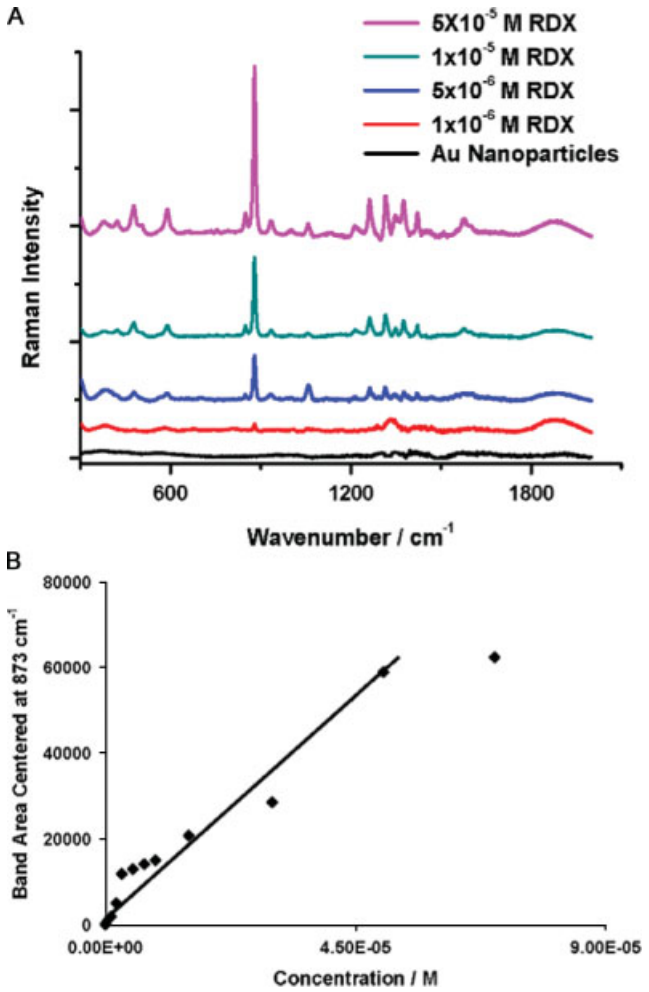

Figure 2. (A) SERS spectra of RDX at concentrations ranging from 1×10^{-6} M to 5×10^{-5} M. Laser power was ~1 mW at the exit of the microscope objective, and the scan time was ~10 s. (B) Peak area at 873 cm^{-1} as a function of RDX concentration.

thus red-shifted from Au seeds to Au nanoparticles due to increased particle size (confirmed by SEM measurements shown in Fig. 1(B)). Au nanoparticles had an average diameter of 90 ± 10 nm, and exhibited spherical to diamond shaped morphologies when compared with spherical Au seeds (~3.5 nm).[20] These observations are consistent with previous studies, in which the absorption maximum of Au nanoparticles was found to depend on the size and shape of the particles.[25–27] For spherical Au nanoparticles, the plasmon band maximum typically falls between 520 and 530 nm.

The synthesized Au nanoparticles were observed to give a good SERS response when thionine was used as the probing molecule (Fig. 1(B)). At the concentration of 10^{-6} M, SERS spectral intensity using Au nanoparticles was found to be ~80% greater than that using the Au seeds. This result is consistent with previously reported data by Ruan *et al.*[28] It has been empirically established that strong SERS effects are obtained when the laser excitation is within the long-wavelength absorption band corresponding to the collective plasmon oscillations.[29,30] Because the absorption spectra of the Au nanoparticles show a single resonance at about 635 nm (Fig. 1(A)), either the red (633 nm) or near-IR (785 nm) laser excitation should be in resonance with surface plasmon of the Au surface and thus suitable for the analysis. For example, Kwon *et al.*[20] reported that gold nanoparticles with an average size of 60–70 nm showed the most intense SERS response when excited at 650 nm. Wei *et al.*[31] found an optimum Au particle size of roughly 90 nm for excitation at 785 nm. The 785-nm laser excitation was used in this study partly because the use of near-IR excitation appears to give higher SERS enhancement and produce the lowest fluorescence background from samples.[28,32–35] This property is particularly advantageous in detecting complex organic molecules such as pyridine,[34] adenine,[35] thionine,[28] and RDX, as shown in this study. For example, Chase and Parkinson[34] found that the SERS enhancement factor for pyridine on Au is higher by using the near-IR rather than visible laser excitation. Kneipp *et al.*[35] showed a large SERS enhancement factor for adenine when near-IR excitation was used.

The Au nanoparticles were subsequently used to investigate the detection of RDX explosive at varying concentrations ranging from 10^{-4} to 10^{-6} M, and the resulting SERS spectra are shown in Fig. 2(A). All spectra were collected in the range from 300 to 2000 cm^{-1} to cover most Raman bands of RDX along with the conventional Raman spectrum of pure RDX for comparison.[36] Since only the vibrational modes of analyte moieties adsorbed on the Au surface are enhanced, there are typically fewer peaks in the SERS spectrum than in the conventional Raman spectrum (without using gold as an SERS substrate). This observation is consistent with those reported in the literature.[19,37,38] The typical

Raman bands assignments of RDX are as follows: the band at 874 cm^{-1} is attributed to the symmetric ring-breathing mode; the band at 930 cm^{-1} is assigned to ring stretching and N–O deformation; the band at 1258 cm^{-1} is due to CH_2 scissoring and N–N stretch vibration;[37] the band at 1312 cm^{-1} results from CH_2 wagging; the band at 1370 cm^{-1} is υNO_2 symmetric stretching vibration and βCH_2 scissoring; finally, the band at 1560 cm^{-1} is attributed to the υNO_2 asymmetric stretch in nitro amines.[37,38]

The strongest SERS Raman band for RDX occurred at 874 cm^{-1} and its intensity increased with an increase of the RDX concentration in solution (Fig. 2(A)). SERS spectra of RDX at different concentrations showed that most of the bands could be identified at the lowest concentration of 1×10^{-6} M RDX with negligible background. On the basis of previously established techniques, the enhancement factor (EF) can be estimated using the following equation:[28,39]

$$EF = \left(\frac{N_{bulk} I_{SERS}}{N_{surf} I_{norm}} \right) \quad (1)$$

where I_{SERS} and I_{norm} are the measured peak areas at 874 cm^{-1} from the SERS spectra and the normal Raman spectra of RDX, respectively. N_{bulk} and N_{surf} are the estimated number of RDX molecules in the reference sample (normal Raman without Au nanoparticles) and the SERS enhanced sample, respectively. These measurements were performed under the same experimental conditions for direct comparisons of data and calculations of EF. The maximum number of adsorbed RDX molecules was calculated following the method developed by Ding *et al.*[40] and found to be approximately 4.65×10^6 per Au particle.[28] The calculated EF for SERS detection of RDX explosive was therefore about 6×10^4, which is higher than the EF previously observed for thionine in our group.[28] This enhancement, which can be attributed to an enhanced electromagnetic field upon laser excitation, is consistent with many theoretical and experimental studies showing that a large SERS enhancement occurs when the analyte is situated at the junction or nanoneck of two adjacent Au nanoparticles.[41–44]

Quantitative SERS analysis of RDX at different concentrations was also evaluated (Fig. 2(B)). The characteristic peak area at 874 cm^{-1} was integrated through the instrument software and plotted as a function of the RDX concentration. The linear dynamic range for SERS analysis of RDX was found from the lower detection limit of 1×10^{-6} M to 5×10^{-5} M (Fig. 2(B)). The band area increased linearly with RDX concentration throughout this range, but linearity was lost when the RDX concentration exceeded 5×10^{-5} M. This detection limit (1×10^{-6} M or 0.22 mg/l) is more than two orders of magnitude lower than that previously reported in the literature (4.5×10^{-4} M or 100 mg/l) using SERS analysis.[19] However, we note that the previous study[19] used a gold-coated polystyrene nanosphere film as the SERS substrate and data were recorded using a portable Raman spectrometer. The reported differences in sensitivity are partially attributed to the use of different SERS substrates and instrumentation.

The reproducibility of SERS measurements of RDX from a given substrate is important especially for sensitive and trace level detections. We thus evaluated the sample-to-sample variations using different batches of Au nanoparticles at a fixed concentration of 5×10^{-5} M RDX (Fig. 3). The results indicate that all spectra overlap with a standard deviation of about 21% for the band area centered at 874 cm^{-1}. This standard deviation is considered

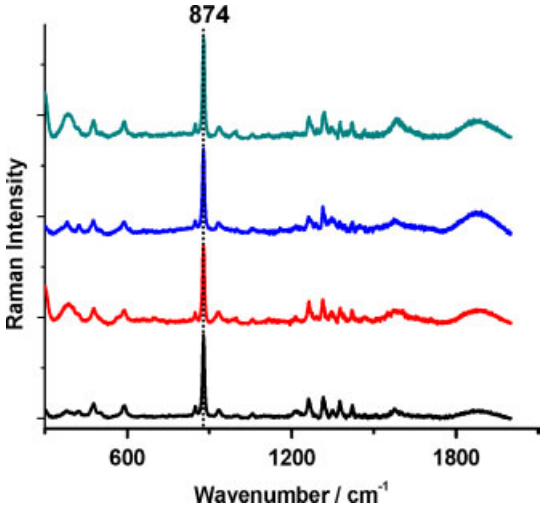

Figure 3. SERS spectra of 5×10^{-5} M RDX using different batches of Au nanoparticles as SERS substrates for reproducibility evaluation.

reasonable for SERS measurements and suggests that our synthesis approach resulted in the production of Au nanoparticles of consistent size and shape among replicate batches. The data also suggest that the SERS technique presented herein holds promise as a quantitative and qualitative tool for rapid screening of RDX.

The SERS technique for detecting RDX was further validated using a contaminated groundwater sample obtained form a U.S. Navy site (Fig. 4(A) and (B)). Rapid detection and screening of RDX explosives in the environment represent a significant challenge because current analytical techniques involve lengthy laboratory preparations and the use of expensive instrumentation (e.g. EPA Method 8330).[45,46] Moreover, groundwater can contain organic impurities which can interfere with the detection and identification of explosives such as RDX, since the EPA method relies on HPLC with analyte detection via retention time only, which is potentially susceptible to false positives. The SERS Raman technique holds promise because the vibrational mode of the SERS spectrum of a given molecule is specific and can provide unique fingerprinting for various organic or inorganic molecules. Here we showed that SERS can be used for sensitive detection of RDX in environmental samples and could potentially offer a valuable tool for rapid screening and characterization of energetics in the environment (Fig. 4(A) and (B)). Using the standard addition technique, SERS analysis revealed that the site groundwater contains about 0.15 ± 0.12 mg/l RDX. The concentration determined by SERS compared favorably with that determined by HPLC via EPA Method 8330 (i.e. 0.12 ± 0.4 mg/l) for the same sample. The standard addition technique was used to correct for matrix interferences because of the presence of unknown constituents in the groundwater. Results showed that the peak intensity at about 874 cm^{-1} increased consistently by spiking the groundwater sample with increasing concentrations of RDX. The error reported in the RDX concentration represents the standard deviation determined using the method by Skoog *et al.*[47]

Our results represent the first use of SERS to detect RDX in a contaminated groundwater at an environmentally relevant concentration, although the SERS technique has been previously demonstrated to detect a range of pollutants such as TNT, perchlorate, pertechnetate, and uranium in groundwater at low

Journal of RAMAN SPECTROSCOPY

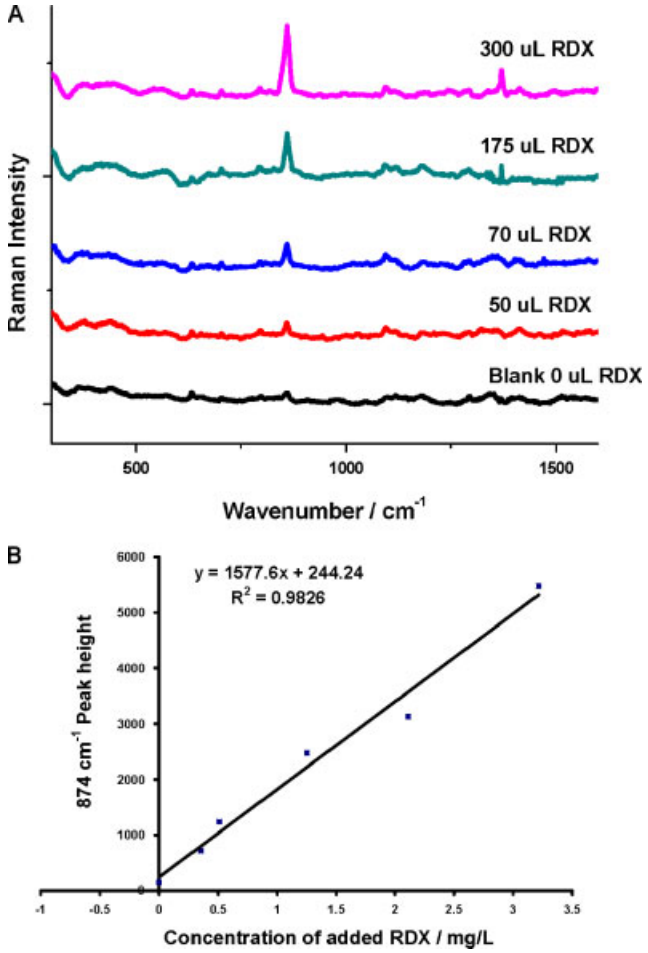

Figure 4. (A) SERS spectra of a contaminated groundwater sample using the standard addition method. (B) Standard addition curve for determining the RDX concentration in groundwater.

concentrations.[48–50] Our work further demonstrates the potential for developing a field SERS detector coupled with a portable Raman spectrometer. The tool would provide environmental and national security professionals with the ability to rapidly screen samples and potentially identify a range of compounds including pollutants, explosives, and other relevant chemical and biological materials.

Acknowledgements

This research was supported in part by the Strategic Environmental Research and Development Program (SERDP) of the U.S. Department of Defense. Oak Ridge National Laboratory is managed by UT-Battelle, LLC for the U.S. Department of Energy under contract DE-AC05-00OR22725.

References

[1] N. Mina, I. Cotte, Y. Colon, C. M. Ramos, L. F. Alzate, S. P. Hernandez-Rivera, M. E. Castro, R. T. Chamberlain, R. T. Lareau, *SPIE* **2003**, *5089*, 363.
[2] A. J. Crockett, H. Craig, W. Sisk, US Army Corps of Engineers, Cold Regions Research & Engineering Overview of on-site analytical methods for explosives in soil Laboratory **1998**, Special report 98-4.
[3] T. L. Pineda, L. Gonzalez, J. Mendez, A. C. C. Olarte, O. L. R. Vivas, S. P. Hernandez-Rivera, N. Mina, M. E. Castro-Rosario, *SPIE* **2005**, *5794*, 1329.
[4] A. H. Wani, D. R. Felt, J. L. Davis, Technical Report ERDC/EL TR-03-11. US Army Corps of Engineers, Engineer Research and Development Center: Vicksburg, **2003**.
[5] H. Yamamoto, M. Morley, G. Speitel, J. Clausen, *Soil Sediment Contam.* **2004**, *12*, 13.
[6] R. Keir, E. Igata, M. Arundell, W. E. Smith, D. Graham, C. McHugh, J. M. Cooper, *Anal. Chem.* **2002**, *74*, 1503.
[7] K. Kneipp, Y. Wang, R. R. Dasari, M. S. Feld, B. D. Gilbert, J. Janni, J. I. Steinfeld, *Spectrochim. Acta* **1995**, *51*, 2171.
[8] J. M. Sylvia, J. A. Janni, J. D. Klein, K. M. Spencer, *Anal. Chem.* **2000**, *72*, 5834.
[9] C. J. McHugh, R. Keir, D. Graham, W. E. Smith, *Chem. Commun.* **2002**, *6*, 580.
[10] J. I. Jerez-Rozo, O. M. Primera-Pedrozo, M. A. Barreto-Caban, S. P. Hernandez-Rivera, *IEEE Sens. J.* **2008**, *8*, 974.
[11] O. M. Primera-Pedrozo, J. I. Jerez-Rozo, E. De la Cruz-Montoya, T. Luna-Pineda, L. C. Pacheco-Londono, S. P. Hernandez-Rivera, *IEEE Sens. J.* **2008**, *8*, 963.
[12] J. F. Bertone, K. L. Cordeiro, J. M. Sylvia, K. M. Spencer, *SPIE* **2004**, *5403*, 387.
[13] M. Kahraman, M. M. Yazici, F. Sahin, M. Culha, *J. Biomed. Opt.* **2007**, *12*, 054015.
[14] W. R. Premasiri, D. T. Moir, M. S. Klempner, N. Krieger, G. Jones, L. D. Ziegler, *J. Phys. Chem. B* **2005**, *109*, 312.
[15] M. Culha, A. Adiguzel, M. M. Yazici, M. Kahraman, F. Sahin, M. Gulluce, *Appl. Spectrosc.* **2008**, *62*, 1226.
[16] G. C. Schatz, M. A. Young, R. P. Van Duyne, *Top. Appl. Phys.* **2006**, *103*, 19.
[17] P. L. Stiles, J. A. Dieringer, N. C. Shah, R. P. Van Duyne, *Annu. Rev. Anal. Chem.* **2008**, *1*, 601.
[18] D. S. Moore, R. J. Scharff, *Anal. Bioanal. Chem.* **2009**, *393*, 1571.
[19] J. F. A. Calzzani, R. Sileshi, A. Kassu, J. M. Taguenang, A. Chowdhury, A. Sharma, P. B. Ruffin, C. Brantley, E. Edwards, *SPIE* **2008**, *6945*, 69451O.
[20] K. Kwon, K. Y. Lee, Y. W. Lee, M. Kim, J. Heo, S. J. Ahn, S. W. Han, *J. Phys. Chem. C* **2007**, *111*, 1161.
[21] T. K. Sau, C. J. Murphy, *J. Am. Chem. Soc.* **2004**, *126*, 8648.
[22] S. Link, M. A. El-Sayed, *Annu. Rev. Phys. Chem.* **2003**, *54*, 331.
[23] C. Burda, X. B. Chen, R. Narayanan, M. A. El-Sayed, *Chem. Rev.* **2005**, *105*, 1025.
[24] L. Brus, *Acc. Chem. Res.* **2008**, *41*, 1742.
[25] K. R. Brown, D. G. Walter, M. J. Natan, *Chem. Mater.* **2000**, *12*, 306.
[26] N. R. Jana, L. Gearheart, C. J. Murphy, *J. Phys. Chem. B* **2001**, *105*, 4065.
[27] C. M. Shen, C. Hui, T. Z. Yang, C. W. Xiao, J. F. Tian, L. H. Bao, S. T. Chen, H. Ding, H. J. Gao, *Chem. Mater.* **2008**, *20*, 6939.
[28] C. M. Ruan, W. Wang, B. H. Gu, *J. Raman Spectrosc.* **2007**, *38*, 568.
[29] J. Zhao, J. A. Dieringer, X. Y. Zhang, G. C. Schatz, R. P. Van Duyne, *J. Phys. Chem. C* **2008**, *112*, 19302.
[30] K. Kneipp, E. Roth, C. Engert, W. Kiefer, *Chem. Phys. Lett.* **1993**, *207*, 450.
[31] A. Wei, B. Kim, B. Sadtler, S. L. Tripp, *Chemphyschem* **2001**, *2*, 743.
[32] Y. Sawai, B. Takimoto, H. Nabika, K. Ajito, K. Murakoshi, *Faraday Discuss.* **2006**, *132*, 179.
[33] K. Kneipp, H. Kneipp, F. Seifert, *Chem. Phys. Lett.* **1995**, *233*, 519.
[34] D. B. Chase, B. A. Parkinson, *Appl. Spectrosc.* **1988**, *42*, 1186.
[35] K. Kneipp, R. R. Dasari, Y. Wang, *Appl. Spectrosc.* **1994**, *48*, 951.
[36] R. Infante-Castillo, S. P. Hernandez-Rivera, *SPIE* **2006**, 62012F.
[37] R. J. Karpowicz, T. B. Brill, *J. Phys. Chem.* **1984**, *88*, 348.
[38] P. Torres, L. Mercado, I. Cotte, S. P. Hernandez, N. Mina, A. Santana, R. T. Chamberlain, R. Lareau, M. E. Castro, *J. Phys. Chem. B* **2004**, *108*, 8799.
[39] Z. H. Zhu, T. Zhu, Z. F. Liu, *Nanotechnology* **2004**, *15*, 357.
[40] Y. H. Ding, X. M. Zhang, X. X. Liu, R. Guo, *Langmuir* **2006**, *22*, 2292.
[41] R. G. Freeman, K. C. Grabar, K. J. Allison, R. M. Bright, J. A. Davis, A. P. Guthrie, M. B. Hommer, M. A. Jackson, P. C. Smith, D. G. Walter, M. J. Natan, *Science* **1995**, *267*, 1629.
[42] A. M. Michaels, J. Jiang, L. Brus, *J. Phys. Chem. B* **2000**, *104*, 11965.
[43] J. Jiang, K. Bosnick, M. Maillard, L. Brus, *J. Phys. Chem. B* **2003**, *107*, 9964.
[44] K. Zhao, H. Xu, B. Gu, Z. Zhang, *J. Chem. Phys.* **2006**, *125*, 081102.
[45] M. Godejohann, L. Heintz, C. Daolio, J. D. Berset, D. Muff, *Environ. Sci. Technol.* **2009**, *43*, 7055.

[46] W. A. MacCrehan, *Anal. Chem.* **2009**, *81*, 7189.
[47] D. A. Skoog, D. M. West, F. J. Holler, S. R. Crouch, *Analytical Chemistry An Introduction*, (7th edn), Harcourt College: Orlando Florida, **2000**, p 601.
[48] B. Gu, C. Ruan, *Anal. Chem.* **2007**, *79*, 2341.
[49] C. M. Ruan, W. Wang, B. Gu, *Anal. Chim. Acta* **2007**, *605*, 80.
[50] B. Gu, C. Ruan, W. Wang, *Appl. Spectrosc.* **2009**, *63*, 98.

Analyst

View Online
Dynamic Article Links

Cite this: *Analyst*, 2011, **136**, 1697

www.rsc.org/analyst

PAPER

An integrated portable Raman sensor with nanofabricated gold bowtie array substrates for energetics detection

Nahla A. Hatab,*[a] C. M. Rouleau,[b] Scott T. Retterer,[c] Gyula Eres,[b] Paul B. Hatzinger[d] and Baohua Gu*[a]

Received 7th December 2010, Accepted 7th February 2011
DOI: 10.1039/c0an00982b

An integrated field-portable surface enhanced Raman scattering (SERS) sensing system has been developed and evaluated for quantitative analysis of energetics such as perchlorate (ClO_4^-) and trinitrotoluene (TNT) at environmentally relevant concentrations and conditions. The detection system consists of a portable Raman spectrometer equipped with an optical fiber probe that is coupled with novel elevated gold bowtie nanostructural arrays as a sensitive and reproducible SERS substrate. Using the standard addition technique, we show that ClO_4^- and TNT can be quantified at concentrations as low as 0.66 mg L^{-1} (or ~6.6 μM) and 0.20 mg L^{-1} (~0.9 μM), respectively, in groundwater samples collected from selected military sites. This research represents the first step toward the development of a field SERS sensor which may permit rapid, *in situ* screening and analysis for various applications including national security, chemical, biological and environmental detection.

Introduction

Real-time analytical methods for environmental monitoring,[1,2] including chemical and biological detection,[3–5] are currently being developed. In particular, there is a significant need for compact and portable instruments that can perform on-site, rapid, sensitive, and accurate detection and identification of toxic chemicals, hazardous materials and energetic chemicals, such as perchlorate, trinitrotoluene (TNT), chemical warfare agents, pollutants, and related chemicals.[4,6–8] Currently, the standard protocol entails collecting samples in the field and transporting them to a designated laboratory for analysis. This process is often expensive, requires significant sample preparation and chemical handling, and may take several days to weeks before results are available. A portable Raman scattering sensor can be a powerful alternative to traditional analytical approaches if the sensitivity of conventional Raman can be improved, for example, by the surface enhanced Raman scattering (SERS) technique. SERS has been developed into a highly sensitive technique for detecting a number of chemical and biological agents when a target molecule is adsorbed or in close proximity to roughened metallic nanostructural surfaces, where the Raman signal is enhanced by 10^6 or greater.[9,10] Details about mechanisms of SERS enhancement and factors that affect SERS are provided in several recent reviews and publications.[11–13]

One of the key challenges for SERS, however, is the fabrication of noble metallic nanostructures that are highly reproducible and sensitive to target molecules. Unfortunately, the high enhancement (up to single molecule detection sensitivity) is usually observed with randomly oriented metallic nanoparticles, from which only a minute fraction exhibits SERS activity (referred to as "hot spots") at the nanogap regions of nanoparticles.[14–16] Additionally, these substrates, which are usually prepared by wet-chemical techniques, often have high sample to sample variability, and it is difficult to achieve acceptable reproducibility for materials prepared from different batches or by different laboratories. For practical applications, it is thus imperative to develop SERS active substrates with reproducible and controllable SERS enhancement. To this end, substrates that show better reproducibility are prepared by physical means such as nanosphere lithography,[17] laser ablation,[18] dip pen nanolithography,[19] and atomic force microscopy.[20] As a result, advanced lithographic techniques such as focused ion beam[21] and electron beam lithography[22,23] have been applied for precision nanofabrication. However, these techniques also suffer from an inability to controllably fabricate the small gap sizes (*e.g.*, <20 nm) that are necessary to achieve maximal SERS enhancement or sensitivity. We have recently demonstrated a new nanofabrication approach combining electron beam lithography, metal deposition, lift-off, and reactive ion etching to produce highly ordered and elevated gold bowtie array substrates with controllable gap sizes to less than 8 nm. These ordered SERS arrays have shown superior reproducibility and high sensitivity with an enhancement factor on the order of 10^{11}.[24]

[a]*Environmental Sciences Division, Oak Ridge National Laboratory, Oak Ridge, TN, 37831, USA. E-mail: abuhatabna@ornl.gov; gub1@ornl.gov; Tel: +1-865-241-2298/574-7286*
[b]*Materials Science & Technology Division Oak Ridge National Laboratory, Oak Ridge, TN, 37831, USA*
[c]*Center for Nanophase Materials Sciences, Oak Ridge National Laboratory, Oak Ridge, TN, 37831, USA*
[d]*Shaw Environmental Inc., Lawrenceville, NJ, 08648, USA*

In this report, we integrate this novel nanofabricated bowtie array substrate as a probe with a portable Raman spectrometer and evaluate its performance for the detection and analysis of environmental pollutants such as perchlorate and TNT in actual groundwater samples. Perchlorate is a widespread contaminant found in groundwater and surface water and is a key component of solid rocket fuel, explosives, fireworks, road flares and other products.[6,25] Perchlorate can also form naturally[26,27] and is known to affect human thyroid function by inhibiting iodide intake. TNT is a common contaminant found in soils and groundwater at military sites and is a toxin to humans and aquatic organisms.[28,29] Standard methods to detect perchlorate and TNT are ion chromatography (IC) and high-performance liquid chromatography (HPLC),[30,31] respectively, each of which requires significant sample preparation and analytical time. Here we show that, without any sample pretreatment, the integrated SERS probe is capable of detecting ClO_4^- and TNT at concentrations as low as 0.66 mg L^{-1} (or ~6.6 μM) and 0.20 mg L^{-1} (~0.9 μM), respectively, in groundwater samples collected from selected military sites.

Results and discussion

The elevated gold bowtie arrays were first fabricated and used as sensitive SERS substrates for detecting energetics by the portable Raman sensor. Fig. 1A shows a typical scanning electron microscope (SEM) image of the actual structures, in which the characteristic overhang gold bowties are located on top of 200 nm tall silicon posts. A precisely controlled deposition of 40 nm thick gold film was used to close the tip-to-tip gap size of the bowtie to 8 ± 1 nm. Aside from improved reproducibility (due to the structural uniformity), one of the advantages of using such elevated structures is that they are decoupled from substrate interactions. This improves the quality factor and the plasmonic coupling efficiency in the structures, leading to large SERS enhancement factors as demonstrated in our previous studies.[24] The enhancement was also found to increase with decreasing gap size, with the highest enhancement observed at the gap size of ~8 nm (the smallest gap fabricated by EBL).[24] For the first time, these structures are used throughout this study for detecting perchlorate and TNT in both laboratory simulated and real groundwater samples. SERS spectra were collected with a portable EZRaman M system (Fig. 1B) as detailed in the Experimental section.

We subsequently performed a series of tests of our sensing system by collecting SERS spectra of standard perchlorate solutions at concentrations ranging from 10^{-3} M to 10^{-6} M in water. Fig. 2 shows the spectra of perchlorate, which are offset for clarity. The strongest SERS peak occurred at about 947 cm^{-1} as a result of the symmetric stretching vibration of the perchlorate molecule. This peak location is in close agreement with what has been previously reported in the literature.[32,33] The lowest

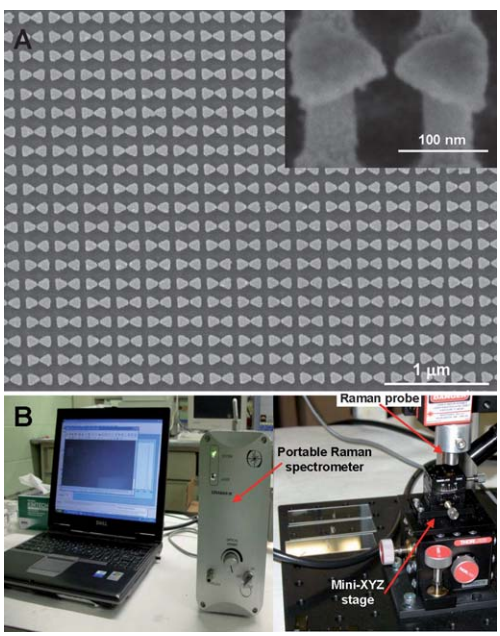

Fig. 1 (A) Top-view of a typical SEM image of the elevated gold bowtie arrays used as surface enhanced Raman scattering (SERS) substrates. The inset is an enlarged, tilted view of a gold bowtie array sitting on the top of silicon posts. (B) Illustration of a portable Raman sensor coupled with a fiber-optic Raman probe and a miniaturized *XYZ* stage.

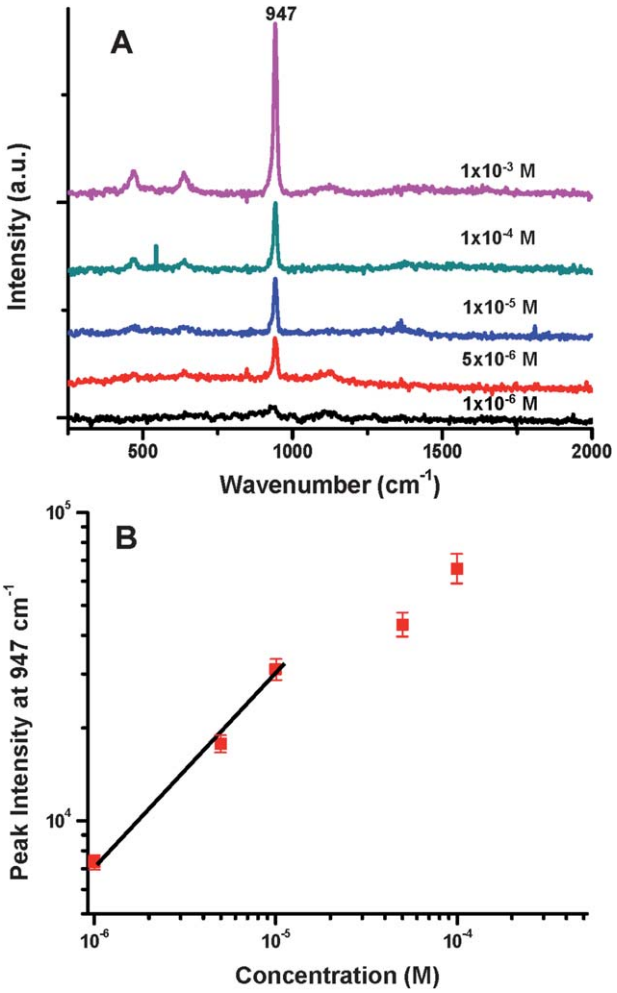

Fig. 2 (A) Detection and spectral analysis of perchlorate (ClO_4^-) at varying concentrations using a portable Raman sensor. (B) A log–log plot of the peak intensity at 947 cm^{-1} as a function of the ClO_4^- concentration.

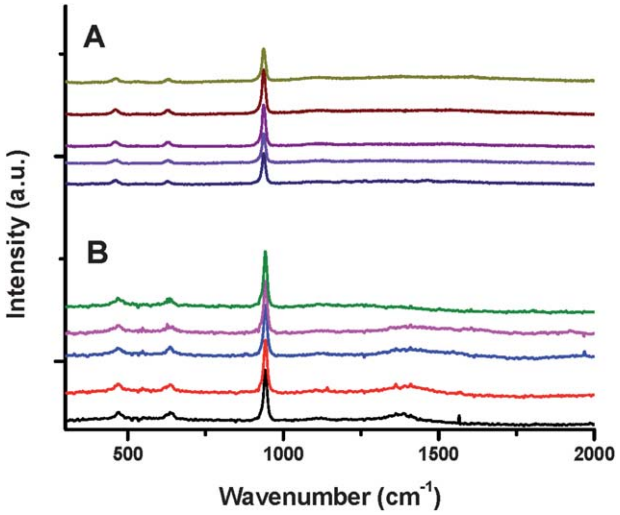

Fig. 3 Reproducibility evaluation of the SERS sensor: (A) SERS spectra of ClO_4^- (1×10^{-4} M) obtained from five different gold bowtie array substrates and (B) spectra of ClO_4^- (5×10^{-3} M) obtained from five different spots on a single gold bowtie array substrate.

perchlorate concentration detected was about 5×10^{-6} M with a notable SERS peak. This detection is equivalent to an enhancement factor of 10^4 to 10^5 by SERS due to enhanced electromagnetic fields generated at or near the surface of the elevated gold bowtie arrays. The detection limit is comparable to or better than those reported in several previous studies,[6,25,32–36] but it is about two orders of magnitude higher than detection limits reported recently using surface modified gold nanoparticles.[32,33] Our study represents the first reported case of perchlorate being detected using a portable Raman spectrometer on elevated gold bowtie array substrates. We also note that many of the previous studies reported the use of organic modifiers such as cystamine,[33] polyethyleneimine fragments containing primary amino and amide functional groups,[37] and dimethylaminoethanethiol[34] in order to increase the sorption or surface concentration of perchlorate, leading to improved detection. One of the disadvantages of using these organic modifiers is the relatively high background scattering resulting from complicated molecular structures of the modifiers (*e.g.*, cystamine and polyethyleneimine),[33,37] which could potentially interfere with detection particularly at relatively high concentrations.

A log–log plot of the peak intensity of the primary Raman scattering band at 947 cm^{-1} indicates that, at relatively low perchlorate concentrations (1×10^{-6} M to 1×10^{-5} M), the peak intensity increases linearly with the perchlorate concentration ($R^2 = 0.998$), but it levels off at higher concentrations (5×10^{-5} M to 1×10^{-4} M) (Fig. 2B). This nonlinear correlation between peak intensity and perchlorate concentration is common when using vibrational spectroscopic techniques such as SERS.[34,38] The observation is partially attributed to limited sorption sites within the gap region of the gold bowtie arrays and also a wide perchlorate concentration range used in the study. Nonetheless these results suggest that the technique can be used for quantitative or semi-quantitative analysis of perchlorate within a given concentration range.

Reproducible substrates are important for SERS to become a valuable tool for quantitative analysis. Fig. 3 shows the SERS spectra collected from five different 1 mm^2 substrate arrays (A) or from five different spots within a given substrate array (B) in order to evaluate the reproducibility of the new bowtie substrates and the portable Raman system. Results indicate that, at a given perchlorate concentration (1×10^{-4} M), the substrate-to-substrate variation for the peak intensity at 947 cm^{-1} is about 18% (Fig. 3A), whereas the spot-to-spot reproducibility is about 10% across five randomly selected spots (Fig. 3B). These observations are attributed to the fact that EBL is capable of fabricating highly uniform or evenly distributed nanogaps with spatial resolution of nanometers serving as "hot spots" for perchlorate detection. On the other hand, although high enhancement has also been observed on substrates such as metallic colloids and roughened electrode surfaces, reproducibility is an issue because it is difficult to achieve uniform particles, particle aggregates or nanogap sizes across a large measuring area for SERS. Nie and Emery reported that with silver colloids there are only a minute fraction of colloid nanoparticles that are likely to be SERS active or considered to be "hot".[15] This has been a major challenge for the use of SERS as a routine analytical tool. Therefore, the use of elevated gold bowtie arrays as SERS substrates shows clear advantages with respect to sensitivity and reproducibility for SERS applications.

To evaluate the applicability of the SERS sensing system for potential field applications, we collected and analyzed a number of realistic contaminated groundwater samples from US Department of Defense sites (Table 1). As with many other techniques, analysis of realistic environmental samples by SERS presents a challenge because samples often have multiple contaminants and complex geochemistry, resulting in interference with the analysis or false positive responses. This is further complicated by the fact that concentrations of the analytes of interest (perchlorate and TNT in this case) are usually orders of magnitude lower than organic and inorganic interfering ions

Table 1 General geochemical properties of groundwater samples

Sample name	Chloride/mg L^{-1}	Sulfate/mg L^{-1}	Nitrate/mg L^{-1}	Phosphate/mg L^{-1}	TOC/mg L^{-1}	pH
Site 1						
GWOBOD02	8.4	9.5	1.2	<0.1	5	5.2
GWOBOD03	6.7	6.4	0.9	<0.1	3.4	5.45
Site 2						
MW01	77.4	1.7	<0.1	<0.1	20.3	5.91
MW04	193.0	13.5	1.6	<0.1	12.6	6.32
Site 3						
MW38	23.8	94.8	8.8	<0.1	4.8	7.39

such as total organic carbon (TOC), chloride and sulfate (Table 1). As a result, we used the standard addition technique to correct for matrix interferences.[39–41] Results are shown in Fig. 4 and 5 as examples, and all additional data are summarized in Table 2 along with the concentration data determined by standard EPA Method 314 for perchlorate and EPA Method 8330 for TNT for comparison. For groundwater sample GWOBOD03, the major contaminant is perchlorate. Results reveal that the peak intensity for perchlorate at 947 cm^{-1} increased consistently with increasing concentration of the added perchlorate in solution (Fig. 4). The measured concentration by SERS, which was 0.66 ± 0.20 mg L^{-1} (~6.6 μM), compared favorably with that determined by IC *via* EPA Method 314 (*i.e.*, 0.59 mg L^{-1}). The errors reported in the SERS perchlorate concentration data represent the standard deviation determined using the method by Skoog *et al.*[39–41] For all groundwater samples, data analyzed by SERS are in general agreement with those analyzed by IC, again indicating that the portable Raman system can potentially be used for rapid, *in situ* analysis of environmental samples. However, further increasing the sensitivity of the portable Raman system is desirable. Previous studies reported the use of 2-dimethylaminoethanethiol as a surface modifier so that perchlorate can be attracted and concentrated onto gold surfaces for improved detection, and this approach is currently being investigated in our laboratory.

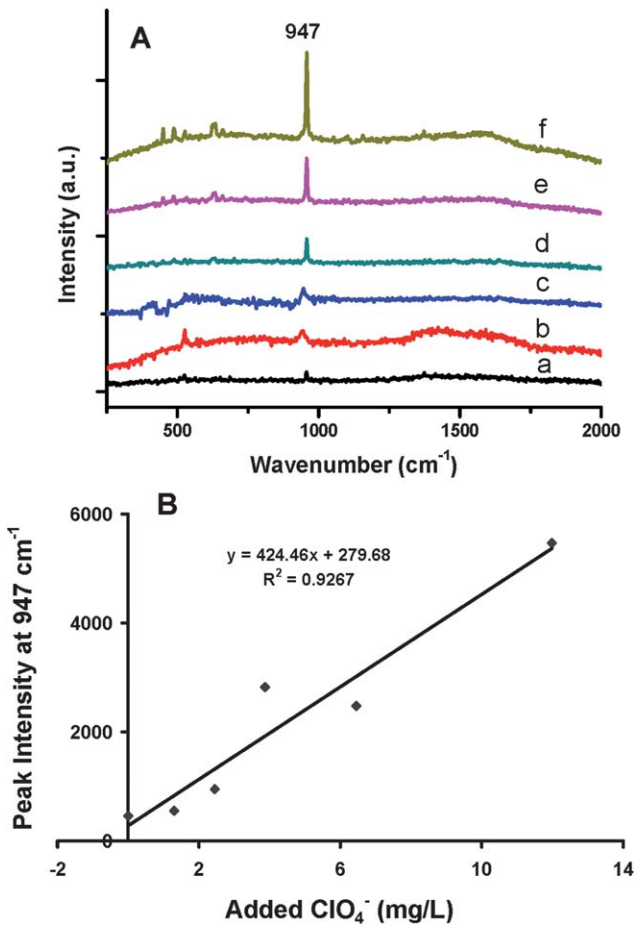

Fig. 4 SERS determination of ClO_4^- in a contaminated groundwater sample (GWOBOD03) by the standard addition method. (A) SERS spectra with the addition of varying concentrations of ClO_4^- at (a) 0, (b) 0.01, (c) 0.03, (d) 0.04, (e) 0.07, and (f) 0.12 mM. (B) The calibration curve for determining the actual ClO_4^- concentration in groundwater.

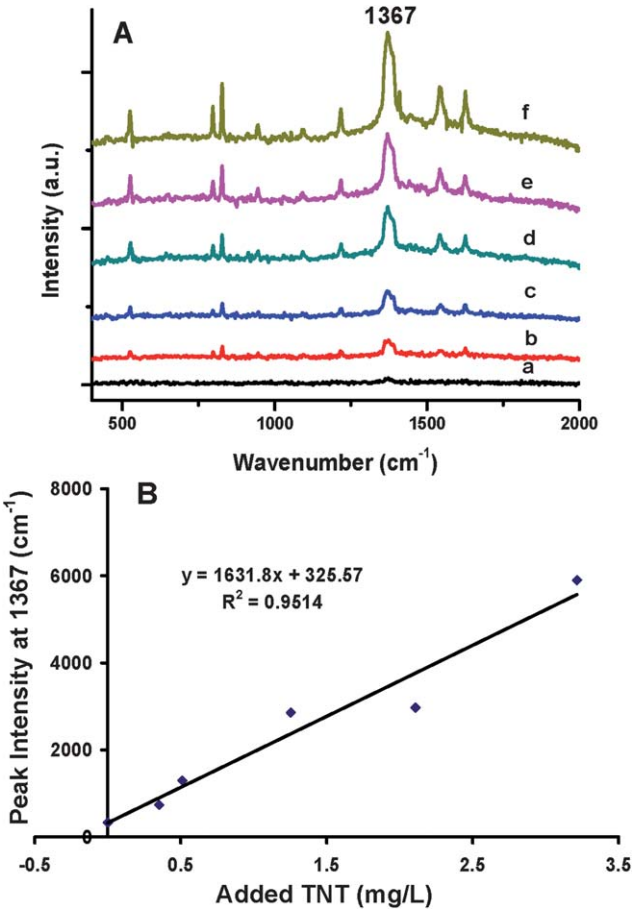

Fig. 5 SERS determination of TNT in a contaminated groundwater sample (MW38) by the standard addition method. (A) SERS spectra with the addition of varying concentrations of TNT standard at (a) 0, (b) 1.6, (c) 2.3, (d) 5.5, (e) 9.3, and (f) 14.0 μM, and (B) the calibration curve for determining the actual TNT concentration in groundwater.

An additional advantage of SERS is its versatility for detecting different contaminants or compounds either individually or simultaneously based upon the characteristic vibrational frequencies of the molecules.[10,42] We have previously reported the use of SERS for detecting the explosive cyclotrimethylenetrinitramine (RDX).[40] Here we also show the use of a SERS sensor for detecting TNT in contaminated groundwater from a military site. The groundwater (sample MW38) is contaminated with TNT at 0.26 mg L^{-1} based on HPLC analysis using EPA Method 8330, but perchlorate was below detection by EPA Method 314 (<0.001 mg L^{-1}) (Table 2). Similarly, using the standard addition technique, we observe that the TNT peak intensity at 1367 cm^{-1} increased consistently with increasing concentration of TNT in solution (Fig. 5). The measured concentration by SERS was 0.20 ± 0.11 mg L^{-1} (~0.9 μM), which agrees well with that determined by HPLC (Table 2). Our detection limit for TNT by SERS is comparable to that reported by Kneipp *et al.* for the detection of TNT (10^{-7} M) using silver and gold nanoparticles in laboratory prepared solutions.[43] However, it is much higher than the detection limit of 10^{-12}

Table 2 Analysis of groundwater samples by the SERS sensor and comparisons of the analytical results with those determined by EPA Methods 314 and 8330 for ClO_4^- and TNT, respectively

	Perchlorate/mg L^{-1}		TNT/mg L^{-1}	
Sample	IC	SERS	HPLC	SERS
GWOBOD02	0.26	0.85	ND	ND
GWOBOD03	0.59	0.66	ND	ND
MW01	18.4	11.5	ND	ND
MW04	14.7	6.15	ND	ND
MW38	ND	ND	0.26	0.20

M recently reported using cysteine modified gold nanoparticles.[44] This is not completely surprising, because, in addition to the use of modifiers, their analyses were performed in pure laboratory prepared solutions using a desktop Raman spectrometer.

Conclusions

Our results represent the first step in developing a SERS-based field sensing system that combines a portable Raman spectrometer with novel elevated gold bowtie arrays for the detection and analysis of perchlorate and TNT in environmental samples. When mature, this SERS technology is expected to provide a tool for rapid, *in situ* screening and analysis of energetics that are both important for environmental monitoring and of interest for national security.

Experimental

Substrate preparation and characterization

Gold bowtie nanostructural array substrates were fabricated by electron beam lithography (EBL) using a JEOL JBX-9300FS EBL system (JEOL, Japan). In brief, a 300 nm thick layer of ZEP520A e-beam resist (ZEON Chemical, Japan) was spun on a 4 in silicon wafer that was subsequently baked at 180 °C for 2 minutes to harden the resist. The resist was then patterned at an acceleration voltage of 100 kV and exposed to a dose of 450 μC cm^{-2}. After exposure, the resist was developed in xylene for 30 s, rinsed in isopropyl alcohol for another 30 s and then dried under a stream of pure nitrogen. Following the development, the sample was exposed to oxygen plasma for 6 s at 100 W (Technics Reactive Ion Etching System) to remove residual resists on the arrays. For the lift-off process, an 8 nm Cr layer was first deposited using an electron-beam dual gun evaporation chamber (VE-240, Thermionics Laboratory, Port Townsend, WA) equipped with a quartz crystal monitor to measure the thickness; the excess resist and Cr were removed *via* lift-off using an acetone bath followed by an isopropyl alcohol rinse. Following the lift-off process, the wafer was dried under a stream of nitrogen. An Oxford Reactive Ion Etching (RIE) instrument (Oxfordshire, UK) was subsequently used at a rate of 100 nm min^{-1} for 1.5 minutes to create the silicon post with the Cr metal pattern on the top and to generate elevated bowtie arrays.

A 40 nm thick gold film was subsequently deposited using the same evaporation chamber to generate the SERS active substrate. All bowtie arrays were made with pairs of triangular prisms (100 nm in size) with a tip-to-tip gap distance of about 8 nm and a center-to-center distance of 300 nm, respectively (Fig. 1A). The array size is 1 × 1 mm, and each wafer (4 in diameter) contains 24 identical arrays for sample analysis. Scanning electron micrographs (SEM) of these arrays were collected either with a JEOL JSM-7400F (JEOL, Tokyo, Japan) or a FEI Nova 600 scanning electron microscope (FEI Oregon, USA) with a field emission gun operated at 10 kV.

All SERS spectra were collected with a portable EZRaman-M system equipped with an InPhotonics fiber optic Raman probe and a miniaturized camera stage attached to it (Fig. 1B). A diode laser operating at 785 nm is used as the excitation source with a high Rayleigh rejection fiber optic probe, which serves three purposes: (1) transmission of the incident laser to the sample, (2) collection of the scattered Raman signal to the spectrograph, and (3) removal of unwanted background signals through an optical filtering device. For sample analysis, the Au bowtie array substrates were mounted on the *XYZ* stage to allow precise focusing and mapping of the entire surface. The incident laser is then focused onto the array substrates, and the scattered SERS signals are collected by the spectrograph/detector system. Each spectrum was accumulated over a period of 60 s and analyzed by ThermoGalactic GRAMS software.

Analyte samples and data acquisition

Sodium perchlorate ($NaClO_4 \cdot H_2O$) was purchased from EM Science (Cherry Hill, NJ). TNT reference standard (1 mg mL^{-1} in MeOH : ACCN 1 : 1) was purchased from AccuStandard, Inc. (New Haven, CT). Deionized (DI) water with resistivity greater than 18.2 mΩ cm (Barnstead E-pure) was used throughout the experiment. Standard solutions of perchlorate in the concentration range of 10^{-3} M to 5×10^{-6} were prepared from a stock solution of 1×10^{-2} M. The calibration curves and reproducibility studies were performed on the same day and from the same wafer to reduce errors associated with instrument variation. A small droplet of standards or samples (~20 μL) were placed on the array substrate and subsequently analyzed after air drying.

To evaluate the applicability of the SERS probe for field analysis, contaminated groundwater samples were collected from several US Department of Defense facilities and were used as received. The general characteristics and ionic compositions of these samples are shown in Table 1. To avoid potential matrix interferences due to unknown background organic or inorganic ions in the groundwater, the standard addition method was used whereby varying amounts of the perchlorate or TNT standard solution were added to a fixed amount of the groundwater. The final volumes were made up to 25 mL using DI water. The sample was then analyzed, and the characteristic Raman intensities at 947 cm^{-1} for perchlorate and 1367 cm^{-1} for TNT were plotted against the final concentration of perchlorate or TNT. A linear regression was used to calculate the absolute value of the *x*-intercept, which corresponds to the true concentrations of perchlorate or TNT in the groundwater.

Acknowledgements

This research was supported by the Strategic Environmental Research and Development Program (SERDP) of the U.S.

Department of Defense, and performed in part at the Center for Nanophase Materials Sciences (CNMS), which is sponsored at Oak Ridge National Laboratory (ORNL) by the Office of Basic Energy Sciences, US Department of Energy. ORNL is managed by UT-Battelle, LLC for the US Department of Energy under contract DE-AC05-00OR22725.

References

1 M. M. Liang and L. H. Guo, *J. Nanosci. Nanotechnol.*, 2009, **9**, 2283–2289.
2 C. B. Ojeda and F. S. Rojas, *Appl. Spectrosc. Rev.*, 2009, **44**, 245–265.
3 B. Raman, D. C. Meier, J. K. Evju and S. Semancik, *Sens. Actuators, B*, 2009, **137**, 617–629.
4 E. M. A. Ali, H. G. M. Edwards and I. J. Scowen, *J. Raman Spectrosc.*, 2009, **40**, 2009–2014.
5 D. Q. Liu, M. J. Sun and A. S. Kord, *J. Pharm. Biomed. Anal.*, 2010, **51**, 999–1014.
6 B. H. Gu, J. Tio, W. Wang, Y. K. Ku and S. Dai, *Appl. Spectrosc.*, 2004, **58**, 741–744.
7 S. Farquharson, W. Smith, Y. Lee, S. Elliott and J. F. Sperry, *Proc. SPIE*, 2002, **4575**, 62–72.
8 O. M. Primera-Pedrozo, J. I. Jerez-Rozo, E. De la Cruz-Montoya, T. Luna-Pineda, L. C. Pacheco-Londono and S. P. Hernandez-Rivera, *IEEE Sens. J.*, 2008, **8**, 963–973.
9 J. Kneipp, B. Wittig, H. Bohr and K. Kneipp, *Theor. Chem. Acc.*, 2010, **125**, 319–327.
10 C. L. Haynes, C. R. Yonzon, X. Y. Zhang and R. P. Van Duyne, *J. Raman Spectrosc.*, 2005, **36**, 471–484.
11 K. Kneipp, H. Kneipp, I. Itzkan, R. R. Dasari and M. S. Feld, *Chem. Rev.*, 1999, **99**, 2957–2975.
12 G. C. Schatz, M. A. Young and R. P. Van Duyne, *Top. Appl. Phys.*, 2006, **103**, 19–45.
13 P. L. Stiles, J. A. Dieringer, N. C. Shah and R. P. Van Duyne, *Annu. Rev. Anal. Chem.*, 2008, **1**, 601–626.
14 J. P. Camden, J. A. Dieringer, Y. M. Wang, D. J. Masiello, L. D. Marks, G. C. Schatz and R. P. Van Duyne, *J. Am. Chem. Soc.*, 2008, **130**, 12616–12617.
15 S. M. Nie and S. R. Emery, *Science*, 1997, **275**, 1102–1106.
16 X. M. Qian, X. Zhou and S. M. Nie, *J. Am. Chem. Soc.*, 2008, **130**, 14934–14935.
17 X. Y. Zhang, C. R. Yonzon and R. P. Van Duyne, *J. Mater. Res.*, 2006, **21**, 1083–1092.
18 E. G. Gamaly and A. V. Rode, *Encycl. Nanosci. Nanotechnol.*, 2004, **7**, 783–809.
19 H. Zhang and C. A. Mirkin, *Chem. Mater.*, 2004, **16**, 1480–1484.
20 H. Yanagi and T. Ohno, *Langmuir*, 1999, **15**, 4773–4776.
21 Q. Min, M. J. L. Santos, E. M. Girotto, A. G. Brolo and R. Gordon, *J. Phys. Chem. C*, 2008, **112**, 15098–15101.
22 Q. M. Yu and G. Golden, *Langmuir*, 2007, **23**, 8659–8662.
23 L. Gunnarsson, E. J. Bjerneld, H. Xu, S. Petronis, B. Kasemo and M. Kall, *Appl. Phys. Lett.*, 2001, **78**, 802–804.
24 N. A. Hatab, H. C. Hsueh., A. L. Gaddis, S. T. Retterer, J. H. Li, G. Eres, Z. Zhang and B. Gu, *Nano Lett.*, 2010, **12**, 4952–4955.
25 W. Wang and B. H. Gu, *Appl. Spectrosc.*, 2005, **59**, 1509–1515.
26 K. H. Kucharzyk, R. L. Crawford, B. Cosens and T. F. Hess, *J. Environ. Manage.*, 2009, **91**, 303–310.
27 B. R. Scanlon, R. C. Reedy, W. A. Jackson and B. Rao, *Environ. Sci. Technol.*, 2008, **42**, 8648–8653.
28 K. Ayoub, E. D. van Hullebusch, M. Cassir and A. Bermond, *J. Hazard. Mater.*, 2010, **178**, 10–28.
29 N. K. Hannink, S. J. Rosser and N. C. Bruce, *Crit. Rev. Plant Sci.*, 2002, **21**(5), 511–538.
30 B. Paull, C. Roux, M. Dawson and P. Doble, *J. Forensic Sci.*, 2004, **49**, 1181–1186.
31 S. Z. Falone, E. M. Vieira and F. I. Onuska, *J. Liq. Chromatogr. Relat. Technol.*, 2006, **29**, 1645–1662.
32 W. Wang, C. M. Ruan and B. H. Gu, *Anal. Chim. Acta*, 2006, **567**, 121–126.
33 C. M. Ruan, W. Wang and A. H. Gu, *Anal. Chim. Acta*, 2006, **567**, 114–120.
34 B. H. Gu, C. M. Ruan and W. Wang, *Appl. Spectrosc.*, 2009, **63**, 98–102.
35 P. A. Mosier-Boss and S. H. Lieberman, *Appl. Spectrosc.*, 2003, **57**, 1129–1137.
36 P. A. Mosier-Boss and S. H. Lieberman, *Langmuir*, 2003, **19**, 6826–6836.
37 S. Tan, M. Erol, A. Attygalle, H. Du and S. Sukhishvili, *Langmuir*, 2007, **23**, 9836–9843.
38 B. H. Gu and C. M. Ruan, *Anal. Chem.*, 2007, **79**, 2341–2345.
39 M. Mulvihill, A. Tao, K. Benjauthrit, J. Arnold and P. Yang, Surface-enhanced Raman spectroscopy for trace arsenic detection in contaminated water, *Angew. Chem., Int. Ed.*, 2008, **47**, 6456–6460.
40 N. A. Hatab, G. Eres, P. B. Hatzinger and B. Gu, *J. Raman Spectrosc.*, 2010, **41**, 1131–1136.
41 D. A. Skoog, D. M. West, F. J. Holler and S. R. Crouch, *Analytical Chemistry: an Introduction*, Harcourt College, Orlando, Florida, 7th edn, 2000, p. 601.
42 S. Tan, M. Erol, S. Sukhishvili and H. Du, *Langmuir*, 2008, **24**, 4765–4771.
43 K. Kneipp, Y. Wang, R. R. Dasari, M. S. Feld, B. D. Gilbert, J. Janni and J. I. Steinfeld, *Spectrochim. Acta, Part A*, 1995, **51**, 2171–2175.
44 S. S. R. Dasary, A. K. Singh, D. Senapati, H. T. Yu and P. C. Ray, *J. Am. Chem. Soc.*, 2009, **131**, 13806–13812.

Resonance modes, cavity field enhancements, and long-range collective photonic effects in periodic bowtie nanostructures

Chun-Hway Hsueh,[1,2,*] Chih-Hong Lin,[3] Jia-Han Li,[3] Nahla A. Hatab,[4] and Baohua Gu[4]

[1]*Department of Materials Science and Engineering, National Taiwan University, Taipei 10617, Taiwan*
[2]*Department of Physics and Astronomy, University of Tennessee, Knoxville, Tennessee 37996*
[3]*Department of Engineering Science and Ocean Engineering, National Taiwan University, Taipei 10617, Taiwan*
[4]*Environmental Sciences Division, Oak Ridge National Laboratory, Oak Ridge, Tennessee 37831*
**hsuehc@ntu.edu.tw*

Abstract: The discovery of single-molecule sensitivity via surface-enhanced Raman scattering on resonantly excited noble metal nanoparticles has brought an increasing interest in its applications to the molecule detection and identification. Periodic gold bowtie nanostructures have recently been shown to give a large enhancement factor sufficient for single molecule detection. In this work, we simulate the plasmon resonance for periodic gold bowtie nanostructures. The difference between the dipole and the quadrupole resonances is described by examining the magnitude and phase of electric field, the bound surface charge, and the polarization. The gap size dependence of the field enhancement can be interpreted by considering cavity field enhancement. Also, additional enhancement is obtained through the long-range collective photonic effect when the bowtie array periodicity matches the resonance wavelength.

OCIS codes: (240.6680) Surface plasmons; (310.6628) Subwavelength structures, nanostructures; (260.5740) Resonance; (260.5430) Polarization; (350.5030) Phase.

References and links

1. R. D. Grober, R. J. Schoelkopf, and D. E. Prober, "Optical antenna, towards a unity efficiency near-field optical probe," Appl. Phys. Lett. **70**(11), 1354–1356 (1997).
2. D. P. Fromm, A. Sundaramurthy, P. J. Schuck, G. Kino, and W. E. Moerner, "Gap-dependent optical coupling of single bowtie nanoantennas resonant in the visible," Nano Lett. **4**(5), 957–961 (2004).
3. A. Sundaramurthy, K. B. Crozier, G. S. Kino, D. P. Fromm, P. J. Schuck, and W. E. Moerner, "Field enhancement and gap-dependent resonance in a system of two opposing tip-to-tip Au nanotriangles," Phys. Rev. B **72**(16), 165409 (2005).
4. H. Guo, T. P. Meyrath, T. Zentgraf, N. Liu, L. Fu, H. Schweizer, and H. Giessen, "Optical resonances of bowtie slot antennas and their geometry and material dependence," Opt. Express **16**(11), 7756–7766 (2008).
5. S. Kim, J. Jin, Y. J. Kim, I. Y. Park, Y. Kim, and S. W. Kim, "High-harmonic generation by resonant plasmon field enhancement," Nature **453**(7196), 757–760 (2008).
6. S. Nie and S. R. Emory, "Probing single molecules and single nanoparticles by surface-enhanced Raman scattering," Science **275**(5303), 1102–1106 (1997).
7. K. Kneipp, Y. Wang, H. Kneipp, L. T. Perelman, I. Itzkan, R. R. Dasari, and M. S. Feld, "Single molecule detection using surface-enhanced Raman scattering (SERS)," Phys. Rev. Lett. **78**(9), 1667–1670 (1997).
8. H. Xu, E. J. Bjerneld, M. Käll, and L. Börjesson, "Spectroscopy of single hemoglobin molecules by surface enhanced Raman scattering," Phys. Rev. Lett. **83**(21), 4357–4360 (1999).
9. P. A. Mosier-Boss and S. H. Lieberman, "Surface-enhanced Raman spectroscopy substrate composed of chemically modified gold colloid particles immobilized on magnetic microparticles," Anal. Chem. **77**(4), 1031–1037 (2005).
10. N. A. Hatab, C. H. Hsueh, A. L. Gaddis, S. T. Retterer, J. H. Li, G. Eres, Z. Zhang, and B. Gu, "Free-standing optical gold bowtie nanoantenna with variable gap size for enhanced Raman spectroscopy," Nano Lett. **10**(12), 4952–4955 (2010).
11. X. Xu, K. Seal, X. Xu, I. Ivanov, C. H. Hsueh, N. A. Hatab, L. Yin, X. Zhang, Z. Cheng, B. Gu, Z. Zhang, and J. Shen, "High tunability of the surface-enhanced Raman scattering response with a metal-multiferroic composite," Nano Lett. **11**(3), 1265–1269 (2011).

#152900 - $15.00 USD Received 15 Aug 2011; revised 12 Sep 2011; accepted 12 Sep 2011; published 22 Sep 2011

12. R. Jin, Y. Cao, C. A. Mirkin, K. L. Kelly, G. C. Schatz, and J. G. Zheng, "Photoinduced conversion of silver nanospheres to nanoprisms," Science **294**(5548), 1901–1903 (2001).
13. H. Fischer and O. J. F. Martin, "Engineering the optical response of plasmonic nanoantennas," Opt. Express **16**(12), 9144–9154 (2008).
14. http://www.lumerical.com
15. E. D. Palik, *Handbook of Optical Constants of Solids* (Academic, Orlando, FL, 1985).
16. D. S. Kong, S. L. Yuan, Y. X. Sun, and Z. Y. Yu, "Self-assembled monolayer of *o*-aminothiophenol on Fe(110) surface: a combined study by electrochemistry, in situ STM, and molecular simulations," Surf. Sci. **573**(2), 272–283 (2004).
17. K. L. Kelly, E. Coronado, L. L. Zhao, and G. C. Schatz, "The optical properties of metal nanoparticles: the influence of size, shape, and dielectric environment," J. Phys. Chem. B **107**(3), 668–677 (2003).
18. K. L. Shuford, M. A. Ratner, and G. C. Schatz, "Multipolar excitation in triangular nanoprisms," J. Chem. Phys. **123**(11), 114713 (2005).
19. K.-H. Su, Q.-H. Wei, X. Zhang, J. J. Mock, D. R. Smith, and S. Schultz, "Interparticle coupling effects on plasmon resonances of nanogold particles," Nano Lett. **3**(8), 1087–1090 (2003).
20. P. K. Jain, W. Huang, and M. A. El-Sayed, "On the universal scaling behavior of the distance decay of plasmon coupling in metal nanoparticle pairs: a plasmon ruler equation," Nano Lett. **7**(7), 2080–2088 (2007).
21. C. Tabor, R. Murali, M. Mahmoud, and M. A. El-Sayed, "On the use of plasmonic nanoparticle pairs as a plasmon ruler: the dependence of the near-field dipole plasmon coupling on nanoparticle size and shape," J. Phys. Chem. A **113**(10), 1946–1953 (2009).
22. T. Jensen, L. Kelly, A. Lazarides, and G. C. Schatz, "Electrodynamics of noble metal nanoparticles and nanoparticle clusters," J. Cluster Sci. **10**(2), 295–317 (1999).
23. S. A. Maier, *Plasmonics Fundamentals and Applications* (Springer Science + Business Media LLC, New York, 2007), pp. 163–164.
24. S. Zou and G. C. Schatz, "Silver nanoparticle array structures that produce giant enhancements in electromagnetic fields," Chem. Phys. Lett. **403**(1-3), 62–67 (2005).
25. K. Zhao, H. Xu, B. Gu, and Z. Zhang, "One-dimensional arrays of nanoshell dimers for single molecule spectroscopy via surface-enhanced Raman scattering," J. Chem. Phys. **125**(8), 081102 (2006).

1. Introduction

It has been shown that a bowtie-shaped nanoantenna, where two metallic triangular prisms facing tip-to-tip and separated by a small gap, produces a large electromagnetic field confined to the gap region [1–5]. This field enhancement enables the detection of single molecule via surface-enhanced Raman scattering (SERS) [6–11]. While the fabrication of a nanoantenna can be achieved using electron beam lithography and lift-off techniques, it is fruitful to have simulation results to provide guidelines in choosing the geometry of the nanostructure, the wavelength and polarization of the incident light, and the dielectric properties of the constituents of the system to obtain the optimum field enhancement. The purpose of the present study is to perform simulations on a model system to examine the different resonance modes and to provide the essential trends of how the plasmon resonance is influenced by the geometric parameters. Specifically, the effects of the gap size and the periodicity of bowtie arrays on the plasmon resonance of the periodic gold bowtie nanostructures are studied.

2. Finite-difference time-domain simulations

A model system of the periodic gold bowtie nanostructures is used for simulations. The side length of the equilateral triangle is 100 nm and the thickness of the Au bowtie is 40 nm with a 0.5 nm thick analyte, *p*-aminothiolphenol (*p*-ATP), on the top surface of the bowtie. At the bottom surface of the bowtie, an 8 nm thick Cr is used to bond the Au bowtie to Si substrate. A schematic drawing of the top view of the bowtie structure on the *x*-*y* plane is shown in Fig. 1(a) and the side view on the *x*-*z* plane is shown in Fig. 1(b). While a perfectly sharp tip at the apex of the triangle cannot be achieved because of limitations by using the electron beam lithography followed by the vapor deposition of gold, simulations of imperfect bowtie structures have been performed by either truncating the tips of the triangle [12,13] or assuming a curvature at the apex [3]. In the present study, the truncated bowtie shown in Fig. 1(a) is adopted as a simplified structure in simulations such that other parameters (e.g., gap between apexes and inter-bowtie distance) can be changed systematically to elucidate the essential trends of how other parameters affect plasmon resonances. First, the difference

#152900 - $15.00 USD Received 15 Aug 2011; revised 12 Sep 2011; accepted 12 Sep 2011; published 22 Sep 2011

between the dipole and the quadrupole resonances is examined. Then, the mechanism of the gap size dependence of the field enhancement is explored. Finally, the effect of the bowtie array periodicity on the field enhancement is studied.

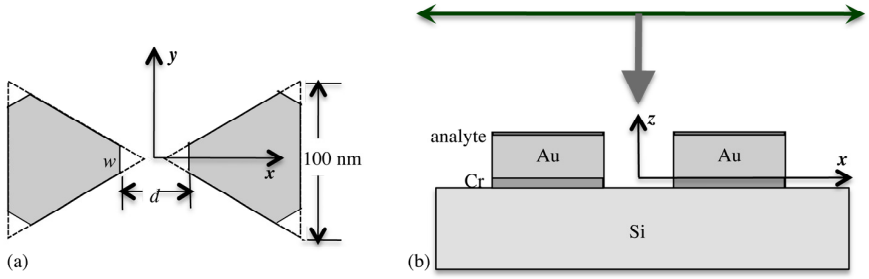

Fig. 1. Schematics showing (a) a truncated bowtie on the *x*-*y* plane and (b) the cross-section of Si/Cr/Au bowtie/*p*-aminothiolphenol nanostructure on the *x*-*z* plane. A polarized plane wave is illuminated from the bowtie side.

Lumerical FDTD Solutions [14], a commercial electromagnetic software based on the finite-difference time-domain method, is used to perform the simulation. Considering the periodic structure, the unit cell adopted in simulations has a dimension corresponding to the inter-bowtie distance on the *x*-*y* plane. Unless noted otherwise, the unit cell of 400 nm × 300 nm on the *x*-*y* plane is adopted in simulations. The dielectric properties of Au, Cr, and Si used in simulations are taken from Palik's handbook [15] and the dielectric constant of *p*-ATP is 7 [16]. A plane wave (500 to 1000 nm wavelength) polarized across the junctions between the triangles (i.e., along the *x*-direction) is illuminated from the bowtie side (i.e., in the negative *z*-direction). The mesh sizes in the bowtie region (including analyte, gap, and Cr layer) vary from 0.25 to 1 nm, and an automatic graded mesh is used in the region outside the bowtie.

3. Results

The simulation results of both the near-field (local field) and the far-field (reflectance) are recorded. For the local field, E intensity (i.e., $|E|^2$) is the largest on the plane containing the bowtie surface among all the constant-z planes, and it is located at the opposing apexes.

3.1 Maximum E intensity enhancement and minimum reflectance

For an apex width, w, of 20 nm, the maximum E intensity enhancement (i.e., $|E|^2/|E_0|^2$ where E_0 is the electric field of the illumination wave) and the reflectance are shown in Figs. 2(a) and 2(b), respectively, as functions of the illumination wavelength, λ, at different gap sizes, d. There are two peaks in each curve in Fig. 2(a). These two plasmon resonances have also been obtained elsewhere using discrete dipole approximation and the peaks at the longer and the shorter wavelengths have been qualitatively described as dipole and quadrupole resonances, respectively [17,18]. When the two truncated triangles are sufficiently apart, the dipole and the quadrupole resonances occur, respectively, at λ = ~640 nm and ~530 nm and red shift occurs for both resonances as d decreases. It should be noted that red shift of the dipole peak becomes more evident as d becomes smaller. This is in agreement with the plasmon ruler equation that the plasmon wavelength shift for polarization along the interparticle axis decays nearly exponentially with the interparticle gap [19–21]. It is shown in Fig. 2(a) that the quadrupole peak is less sensitive to the gap size and is higher than the dipole peak when d is greater than 10 nm. The dipole peak increases as d decreases. It has also been reported elsewhere for Ag nanoparticles that the quadrupole resonance is much less sensitive to the interparticle interactions than the dipole resonance [22].

The minimum reflectance corresponds to the maximum scattering and absorption of the system. There are two valleys in each curve in Fig. 2(b) for the reflectance and both valleys show red shift as d decreases. The far-field resonance can occur at a different wavelength

#152900 - $15.00 USD Received 15 Aug 2011; revised 12 Sep 2011; accepted 12 Sep 2011; published 22 Sep 2011

compared to the near-field resonance because far-field is dictated by the average behavior of the entire bowtie. While the magnitude of local intensity enhancement strongly depends on the gap size as shown in Fig. 2(a), Fig. 2(b) shows that the magnitude of minimum reflectance is relatively insensitive to the gap size.

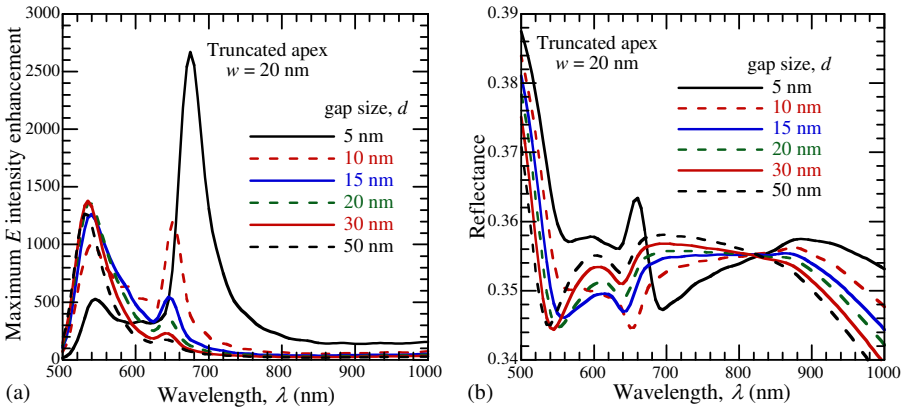

Fig. 2. (a) Maximum E intensity enhancement at the apex and on the bowtie surface and (b) the reflectance as functions of the illumination wavelength, λ, at different gap sizes. The width of the truncated apex, w, is 20 nm.

For the gap size d = 10 nm, the dipole and the quadrupole resonances occur, respectively, at λ = 655 and 540 nm. The E intensity enhancement profiles on the plane containing the bowtie surface are shown in Figs. 3(a) and 3(b), respectively, for λ = 655 and 540 nm. The maximum enhancement is always at the apexes. However, compared to the dipole resonance, the quadrupole resonance has more significant enhancement at the sides. This is in agreement with the results obtained elsewhere [17]. While the E intensity enhancement is highly confined to the gap region for dipole resonance, it spreads to the bowtie surface for quadrupole resonance.

3.2 Phase of electric field and bound surface charge

It is instructive to examine the phase of the electric field and the bound surface charge on the bowtie surface to distinct the quadrupole resonance from the dipole resonance. The dominant component of the electric field is E_x in most regions because of the polarization direction. The field has a harmonic time dependence and the solution of the time-independent component, E_x, from FDTD simulations is a complex number, such that

$$E_x = \mathrm{Re}[E_x] + i\mathrm{Im}[E_x] = |E_x|\exp(i\phi), \tag{1}$$

where $|E_x|$ and ϕ are the magnitude and the phase of E_x, respectively, and

$$|E_x| = \sqrt{\mathrm{Re}[E_x]^2 + \mathrm{Im}[E_x]^2}, \tag{2a}$$

$$\phi = \tan^{-1}\left(\mathrm{Im}[E_x]/\mathrm{Re}[E_x]\right), . \tag{2b}$$

While the E intensity; i.e., $|E|^2$, enhancement profiles are shown in Figs. 3(a) and 3(b), the corresponding phase profiles of the dominate component of the electric field E_x, ϕ, are shown in Figs. 3(c) and 3(d). Only E_x is discussed here to avoid the complexity of the three components of the electric field. For λ = 655 nm (i.e., dipole resonance), the phase is ~$-\pi$ in both the opposing apex and the end of bowtie regions, and it is ~π in between those two regions. However, it should be noted that $-\pi$ and π are the same in terms of the trigonometric functions. Hence, the phase is relatively uniform on the bowtie surface for dipole resonance.

#152900 - $15.00 USD Received 15 Aug 2011; revised 12 Sep 2011; accepted 12 Sep 2011; published 22 Sep 2011

For λ = 540 nm (i.e., quadrupole resonance), the phase is about zero in the opposing apexes region and progressively shifts toward $\pi/2$ as the position moves toward the ends of the bowtie.

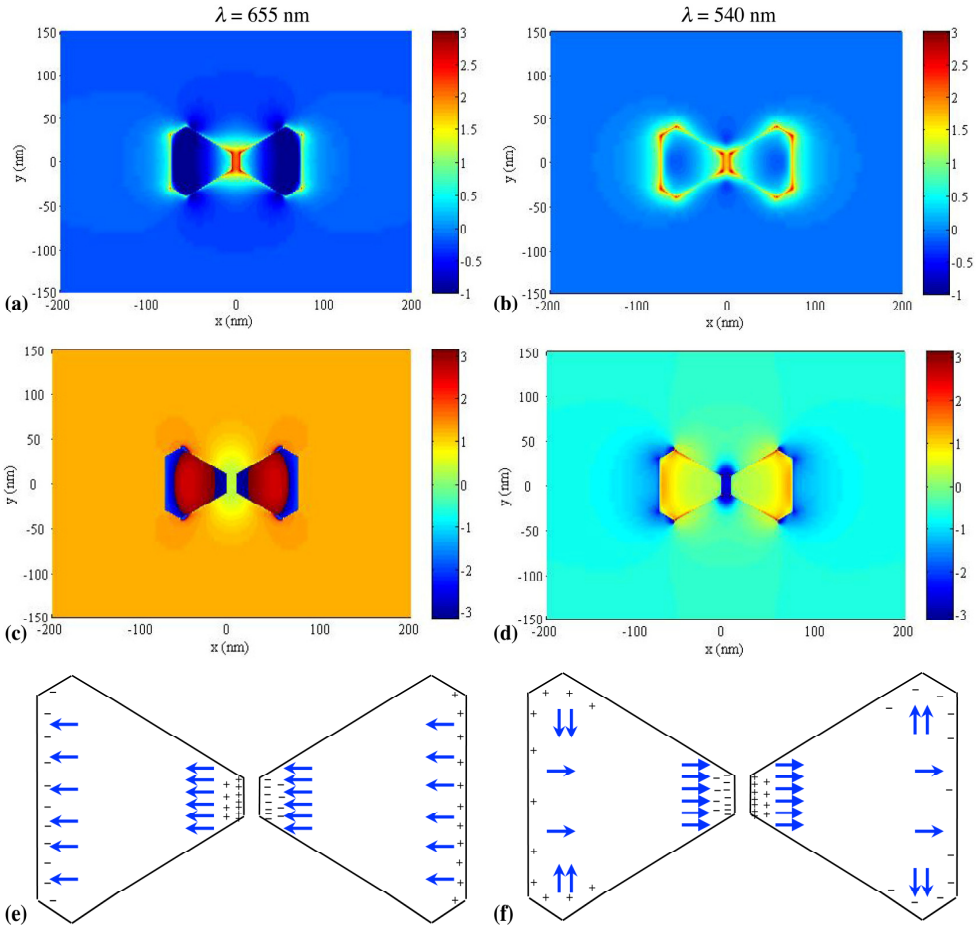

Fig. 3. The E intensity enhancement profiles on the plane containing the bowtie surface for (a) λ = 655 nm with dipole resonance and (b) λ = 540 nm with quadrupole resonance. The color bar is logarithmic-scale and limited to –1 to 3. The corresponding phase profiles of E_x for (c) λ = 655 nm and (d) λ = 540 nm, and schematics showing the bound surface charge distribution on the bowtie surface and the major polarizations for (e) λ = 655 nm and (f) λ = 540 nm. The apex is truncated with w = 20 nm and the gap size, d, is 10 nm.

The bound surface charge density can be derived from the electric field. In the presence of an electric field, **E**, the polarization of the material, **P**, is

$$\mathbf{P} = \left(\varepsilon_m - \varepsilon_0\right)\mathbf{E}, \tag{3}$$

where ε_m and ε_0 are the electric permittivities of the material and vacuum, respectively. This polarization results from the alignment of dipoles with the electric field and is related to the bound surface charge density, ρ_b, via

$$\rho_b = \mathbf{P} \cdot \mathbf{n}, \tag{4}$$

where **n** is the unit vector normal to the surface. Combination of Eqs. (3) and (4) yields

$$\rho_b = \left(\varepsilon_m - \varepsilon_0\right)\mathbf{E} \cdot \mathbf{n}. \tag{5}$$

#152900 - $15.00 USD Received 15 Aug 2011; revised 12 Sep 2011; accepted 12 Sep 2011; published 22 Sep 2011

Hence, using the electric field solutions obtained from FDTD simulations, ρ_b can be obtained from Eq. (5), and the sign of ρ_b is related to the phase of **E**. On the bowtie surface, the permittivity of Au, ε_{Au}, is used to calculate ρ_b from Eq. (5).

Taking the left triangle in Fig. 1(a) as an example, the normal vectors **n** at the opposing apex and the end of bowtie are $\bar{x}$ and $-\bar{x}$, respectively, and ρ_b becomes

$$\rho_b = \left(\varepsilon_{\text{Au}} - \varepsilon_0\right) E_x \quad \text{(at opposing apex)} \tag{6a}$$

$$\rho_b = -\left(\varepsilon_{\text{Au}} - \varepsilon_0\right) E_x \quad \text{(at end of bowtie)} \tag{6b}$$

For λ = 655 nm, $\phi \sim -\pi$ and E_x is negative in both the opposing apex and the end of bowtie regions. Also, because Au has small dielectric loss; i.e., Im[ε_{Au}] is small, and Re[ε_{Au}] is negative, $\varepsilon_{\text{Au}}-\varepsilon_0$ is negative. As a result, ρ_b is positive in the opposing apex region but is negative in the end of bowtie region. For λ = 540 nm, ϕ approaches 0 and $\pi/2$ (i.e., E_x is positive and positive but very small), respectively, in the opposing apex and the end of bowtie regions. As a result, ρ_b is negative in the opposing apex region but is slightly positive in the end of bowtie region. To satisfy the charge balance condition, some positive charges should exist at the side edge of the bowtie. The bound surface charges on the other sides and the corners of the bowtie can also be calculated by considering E_x, E_y, and the unit vector normal to the corner. Since the field enhancement for λ = 655 nm is more confined in the gap region as shown in Fig. 3(a), the bound surface charges are most likely to exist in the opposing apex region and in the end of bowtie region. The field enhancement for λ = 540 nm has more significant enhancement at the sides in Fig. 3(b), and the bound surface charges around the corners need to be considered in describing the physical mechanism. The schematic drawings of the charge distribution for λ = 655 and 540 nm at a specific time are shown, respectively, in Figs. 3(e) and 3(f). Like the field, the charges have a harmonic time-dependence and it is much more complicated than Figs. 3(e) and 3(f); however, the dipole plasmon resonance and quadrupole plasmon resonance can be seen in Figs. 3(e) and 3(f). The polarizations **P**, which can be calculated from Eq. (3), can also be described by the interactions between positive and negative bound surface charges. For simplicity, only the polarizations in large amplitude at a specific time are plotted as the arrow symbols in Figs. 3(e) and 3(f). For λ = 655 nm, the polarization gives the dipole moments in each triangular prism and most of the polarizations are in the opposing apex regions. This concludes that the dipole plasmon resonance occurs for λ = 655 nm case. For λ = 540 nm, it has not only the similar dipole moments and plasmon resonance as described for λ = 655 nm case, but also the quadrupole plasmon resonance for the opposite polarizations in the two corners of the end of the bowtie regions. This concludes that the dipole plasmon resonance that is mostly in the opposing apex regions and the quadrupole plasmon resonance that is in each triangular prism both occur for λ = 540 nm case.

3.3 Cavity field enhancement

The FDTD simulation results of the maximum E intensity enhancement as a function of the gap size, d, are shown in Fig. 4(a) at different apex widths. For d > 50 nm (not shown in figure), the maximum $|E|^2$ enhancement is insensitive to the gap size (i.e., the two prisms are sufficiently far apart to mostly eliminate near-field coupling between prisms). However, for d < 50 nm, the maximum $|E|^2$ enhancement versus d relation can be fitted by a power law, such that

$$\left|E\right|^2 = Ad^m, \tag{7}$$

where A and m are fitting parameters with A being the intercept of the fitting line with the ordinate and m being the slope in the log-log plot. It can be seen in Fig. 4(a) that the maximum $|E|^2$ enhancement decreases with both the increasing gap size and the increasing apex width.

#152900 - $15.00 USD Received 15 Aug 2011; revised 12 Sep 2011; accepted 12 Sep 2011; published 22 Sep 2011

It is of interest to explore the above power-law dependence. The E field intensity in a plasmonic cavity, which can be formed by the junction between two closely spaced metal nanoparticles, is related to the cavity geometry and quality factor, the coupling efficiency, and the absorption and radiation loss [23]. A general equation to describe this field intensity for all plasmonic cavity structures is unattainable and a semi-quantitative approach is used in the present study to describe the cavity field enhancement. For a bowtie cavity, the field intensity is inversely proportional to the effective volume, proportional to the square of the cavity quality factor, and affected by the absorption and radiation loss. For a small gap size, the field is highly confined in the gap region at its resonant wavelength and the absorption loss for the bowtie cavity varies with the gap size. According to [23], the absorption loss for a metallic cavity is inversely proportional to its quality factor. Because the quality factor of a plasmonic cavity increases slightly as the cavity becomes smaller, the effects of the absorption loss and the quality factor are not significant. The radiation loss also varies with the gap size; however, it is neglected for simplicity in analyses because the field is always highly confined at the resonant wavelength. While the effective volume of the bowtie cavity is proportional to the true volume of the bowtie cavity which is the product of the apex width, w, the gap size, d, and the height of the bowtie, the E field intensity should be approximately inverse-proportional to the product of w and d when the height is fixed. Hence, for a fixed bowtie height, the $|E|^2$ enhancement should be approximately proportional to $(wd)^{-1}$. This dependence is modified by other factors such as the difference between the effective volume and the true volume of the cavity, the quality factor, and the absorption and radiation loss. The FDTD data shown in Fig. 4(a) for three different apex widths are re-plotted in Fig. 4(b) as a function of wd. The three data sets can be fitted by a power law with a slope of –1.08 in a log-log plot which is in good agreement with the predicted value of –1.

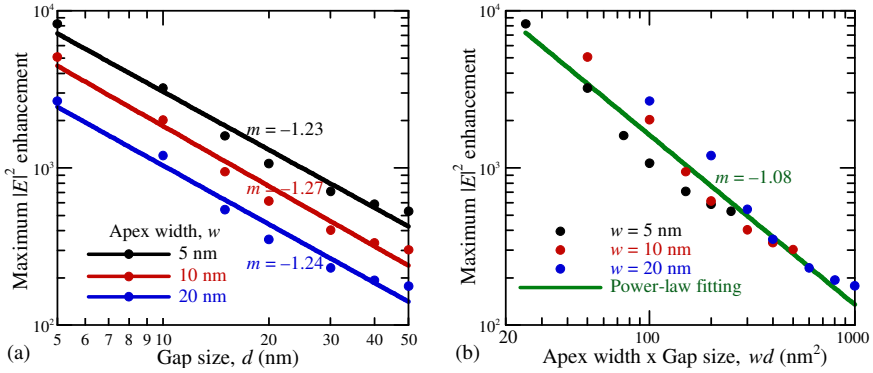

Fig. 4. The maximum E intensity enhancement at plasmon resonance as a function of (a) the gap size, d, for apex widths w of 5, 10, and 20 nm and (b) the product of the apex width and the gap size, wd. (symbols: FDTD data; lines: power-law fitting)

3.4 Long-range collective photonic effect

While the gap size dictates the short-range interaction between the two triangular prisms of the bowtie structure, the inter-bowtie distance controls the long-range interaction between neighboring bowties. Using the T-matrix method, the long-range collective photonic effect has been concluded such that additional enhancement can be achieved when the periodicity of the arrays of nanostructures matches the plasmon resonance wavelength of the nanostructures [24,25]. To study this collective photonic effect, truncated bowties with apex width of 10 nm and gap size of 10 nm are considered in FDTD simulations. Because the polarization of the incident light is in the x-direction, the inter-bowtie distance controlling this long-range interaction is the one in the x-direction. Fixing the (center-to-center) inter-bowtie distance in the y-direction at 300 nm, the maximum E intensity enhancement is plotted as a function of

#152900 - $15.00 USD Received 15 Aug 2011; revised 12 Sep 2011; accepted 12 Sep 2011; published 22 Sep 2011

the inter-bowtie distance in the *x*-direction, *c*, in Fig. 5. A major peak occurs at *c* = 650 nm that coincides with the resonance wavelength which, in turn, confirms the long-range collective photonic effect. A secondary peak occurs at *c* = 340 nm that is slightly longer than the half resonance wavelength, 325 nm. This secondary peak could result from the long-range interaction between the second neighboring bowties with a modification from the presence of the first neighboring bowties.

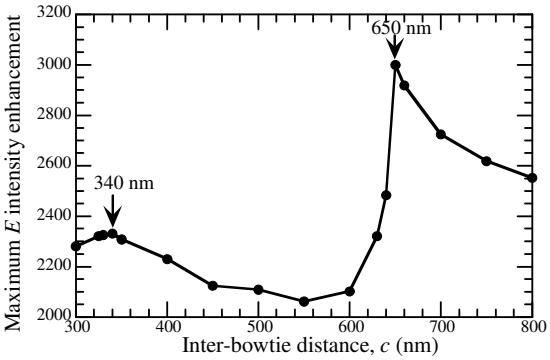

Fig. 5. The maximum *E* intensity enhancement at plasmon resonance as a function of the inter-bowtie distance along the polarization direction, *c*, for fixing the inter-bowtie distance along the direction normal to the polarization as 300 nm and truncated apex with *w* = 10 nm and *d* = 10 nm.

4. Conclusion

In conclusion, we use FDTD to simulate the plasmon resonance of periodic gold bowtie nanostructures with truncated apexes. The illumination light is polarized along the direction connecting the two opposing apexes of the two triangles of a bowtie. Bowties with different gap sizes are considered to systematically examine how the gap size affects the near-field *E* intensity and the far-field reflectance of periodic gold bowtie nanostructures. Both dipole and quadrupole resonances are evident in the simulation results and both resonances show red shift with decreasing gap size. While the *E* intensity enhancement is highly confined to the gap region for dipole resonance, it has more significant enhancement at the sides for quadrupole resonance. Also, these two resonances are different in the phase of electric field, the bound surface charge distribution on the bowtie surface, and the polarization. Both resonances show red shift with decreasing apex width. We found that the peak at a longer wavelength is caused by the dipole resonance between two triangular prisms, while the other peak at a shorter wavelength has the quadrupole resonance in each triangular prism in addition to the dipole resonance between two triangular prisms. A log-log plot of the field enhancement versus the product of apex width and gap size can be fitted by a straight line with a slope of –1.08 for the periodic bowtie arrays. This is in good agreement with the predicted value of –1 based on plasmon resonance cavity. When the periodicity of the periodic bowtie structures matches the resonance wavelength, a major peak is observed in the maximum *E* intensity enhancement versus the inter-bowtie distance relation. This confirms the long-range collective photonic effect. In addition, when the periodicity is about the half resonance wavelength, a secondary peak is observed. This could be attributed to the long-range interaction between the second neighboring bowties.

Acknowledgments

This research was jointly supported by National Science Council, Taiwan under contracts no. NSC100-2221-E-002-128 and no. NSC99-2221-E-002-147, and by the Strategic Environmental Research and Development Program of the U.S. Department of Defense.

#152900 - $15.00 USD Received 15 Aug 2011; revised 12 Sep 2011; accepted 12 Sep 2011; published 22 Sep 2011